UNIVERSITÉ DU QUÈBEC Â CHICOUTIMI

MÉMOIRE PRÉSENTÉ Â
L'UNIVERSITÉ DU QUÈBEC Â CHICOUTIMI
COMME EXIGENCE PARTIELLE
DE LA MAÎTRISE EN INGÉNIERIE

PAR
HANY AMMAR

# EFFET DES IMPERFECTIONS DE LA COULÉE SUR LES PROPRIÉTÉS EN FATIGUE DES ALLIAGES DE FONDERIE ALUMINIUM SILICIUM

AVRIL 2006

Bibliothèque Paul-Émile-Boulet

UQAC Université du Québec à Chicoutimi

# ***Mise en garde/Advice***

Afin de rendre accessible au plus grand nombre le résultat des travaux de recherche menés par ses étudiants gradués et dans l'esprit des règles qui régissent le dépôt et la diffusion des mémoires et thèses produits dans cette Institution, **l'Université du Québec à Chicoutimi (UQAC)** est fière de rendre accessible une version complète et gratuite de cette œuvre.

Motivated by a desire to make the results of its graduate students' research accessible to all, and in accordance with the rules governing the acceptation and diffusion of dissertations and theses in this Institution, the **Université du Québec à Chicoutimi (UQAC)** is proud to make a complete version of this work available at no cost to the reader.

L'auteur conserve néanmoins la propriété du droit d'auteur qui protège ce mémoire ou cette thèse. Ni le mémoire ou la thèse ni des extraits substantiels de ceux-ci ne peuvent être imprimés ou autrement reproduits sans son autorisation.

The author retains ownership of the copyright of this dissertation or thesis. Neither the dissertation or thesis, nor substantial extracts from it, may be printed or otherwise reproduced without the author's permission.

UNIVERSITÉ DU QUÈBEC Â CHICOUTIMI

MÉMOIRE PRÉSENTÉ Â
L'UNIVERSITÉ DU QUÈBEC Â CHICOUTIMI
COMME EXIGENCE PARTIELLE
DE LA MAÎTRISE EN INGÉNIERIE

BY
HANY AMMAR

# EFFECT OF CASTING IMPERFECTIONS ON THE FATIGUE PROPERTIES OF ALUMINUM-SILICON CASTING ALLOYS

APRIL 2006

*Dedicated to my father and my mother*

*إهداء إلي أبي و أمي*

# RÉSUMÉ

L'énergie est le facteur simple le plus critique faisant face au monde aujourd'hui. L'industrie de l'automobile a fait un pas de géant en avant en réduisant le poids des voitures par le remplacement des produits moulés et malléables en fer avec des produits en aluminium. Les alliages aluminium-silicium de fonderie se retrouvent dans plusieurs applications dans ce secteur, en raison de leur rapport élevé de résistance/poids qui améliore leur performance et l'économie de carburant. Les coulées des alliages d'aluminium dans des moules en sable, die casting, et dans des moules permanents ont une importance critique lors de la construction de moteur, de blocs de moteur, de pistons, de têtes de cylindre, de chemises, de carters, de vilebrequins, de carburateurs, de valves de frein et de nombreuses autres composantes se retrouvant dans la conception d'une voiture.

Cinq alliages de fonderie Al-Si, avec différents contenus de silicium s'étendant de 7 à 17%, ont été choisis pour cette étude : les alliages hypoeutectiques LP PM319-F, A356-T6 et C354-T6, et alliages hypereutectiques AE425 et PM390, tous utilisés intensivement dans des applications automobile. Le but de ce travail était l'étude de l'effet des défauts de coulée sur les propriétés de fatigue de ces alliages en corrélant la vie en fatigue d'échantillons avec les défauts initiant les craques par fatigue et la caractérisation de ces défauts (c.-à-d., porosités, films d'oxyde, bandes de glissement, etc..), dans le but de comprendre leur rôle critique sur la vie en fatigue. La porosité a été étudiée en terme de taille de pore sur la surface de rupture d'échantillon et sa localisation, c.-à-d. près de la surface ou à l'intérieur de la pièce. L'effet de la pression isostatique chaude (HIPping) sur la vie en fatigue de l'alliage C354-T6 a été également étudié, et le comportement des échantillons non soumis au HIP et ceux soumis au HIP a été a comparé.

Les surfaces de rupture de 157 échantillons de fatigue ont été examinées en utilisant un microscope électronique à balayage (technique MEB) pour identifier l'emplacement du déclenchement des fissures par fatigue, complétée par un analyseur d'image pour les mesures quantitatives des défauts amorçant la fissure par fatigue. Les caractéristiques microstructurales (espacements secondaires des bras de dendrite, caractéristiques des particules eutectiques de silicium, taille des grains et phases intermétalliques) ont été examinées en utilisant des techniques d'analyse d'image et de microanalyse grâce à la microsonde d'électronique (EPMA) pour comprendre le comportement en fatigue.

Les résultats prouvent que la porosité surfacique est le défaut de coulée le plus important affectant la vie en fatigue, puisqu'elle agit en tant qu'emplacement le plus favorable pour le déclenchement de craque par fatigue: parmi les échantillons examinés,

82% ont rompus sous l'effet de la porosité surfacique agissant en tant qu'emplacement de déclenchement de fissure par fatigue. Par ailleurs, on peut constater que la durée de vie en fatigue des échantillons diminue à mesure que la taille des pores en surface augmente et vice versa.

En l'absence de porosités en surface, d'autres défauts de coulée tels que des films d'oxyde près de la surface peuvent être responsables du déclenchement de craque par fatigue : 3% de tous les échantillons examinés ont rompus en raison de la présence de tels films d'oxyde. En l'absence de porosités et de films d'oxyde, les bandes de glissement peuvent agir en tant qu'emplacement principal de déclenchement de craque; dans ce cas, on observe que, pour 3% de tous les échantillons examinés, la fracture est causée par des bandes de glissement.

L'initiation de craque par fatigue commence toujours à partir de la surface libre de l'échantillon quelque soit l'emplacement de l'amorce de la fissure (porosités, films d'oxyde, bandes de glissement), soit à l'endroit où l'effort maximum appliqué est observé; le niveau de contrainte diminue de la surface vers le centre de l'échantillon (intérieur du spécimen), ce qui est favorable pour la propagation de craque par fatigue. Ainsi, il est impossible qu'une fissure se propage de l'intérieur de l'échantillon vers la surface libre, c'est-à-dire contre le gradient de contraintes.

La localisation de la porosité (c.-à-d. près du bord ou à l'intérieur de l'échantillon) influence également le comportement en fatigue. On constate que, bien que les échantillons non rompus (fin de bande) contiennent des porosités, l'occurrence de cette porosité à l'intérieur des échantillons a beaucoup moins d'influence sur le déclenchement de craques que si la porosité était située au bord de la surface de l'échantillon, comme c'est le cas pour les échantillons rompus.

La technique de SEM par laquelle les mesures de porosité ont été effectuées, peut être appliquée avec une grande exactitude pour des mesures des pores simples responsables du déclenchement de fissure par fatigue. Cependant quand l'espace de déclenchement de fissures contient des pores multiples (comme dans le cas de l'alliage de LP PM319-F) ou une structure poreuse spongieuse (comme dans le cas d'alliage AE425), les mesures de SEM ne sont pas assez proportionnées pour déterminer l'emplacement exact du déclenchement des craques par fatigue. Dans ces cas-ci, les mesures devraient être effectuées en utilisant la microscopie optique sur une section longitudinale du spécimen rompu pour fournir une plus grande exactitude des résultats. Cependant, c'est un processus long.

La pression isostatique chaude (HIPping) permet d'améliorer la résistance en fatigue de l'alliage C354-T6 en réduisant ou en éliminant la porosité surfacique, et de ce fait la vie en fatigue augmente. En l'absence de la porosité surfacique, d'autres emplacements de déclenchement de fissures tels que des films d'oxyde et des bandes de glissement deviennent opératifs.

Les facteurs microstructuraux tels que les caractéristiques de particules de silicium eutectique (espacement secondaire des bras de dendrite, phases intermétalliques et taille des grains) ont une influence directe sur la durée de vie en fatigue et affectent fortement la propagation des fissures. Pour les alliages hypereutectiques, les particules primaires de silicium contribuent au comportement en fatigue en accélérant la propagation des fissures par la décohésion et la fissuration de ces particules sous chargement cyclique.

# ABSTRACT

Energy is the single most critical factor facing the world today. The automotive industry has taken a giant step forward in reducing the weight of the car by replacing cast and malleable iron castings with aluminum castings. Aluminum-silicon casting alloys find extensive applications in this sector, due to their high strength-to-weight ratio which improves the performance and fuel economy. Aluminum sand, die, and permanent mold castings are critically important in engine construction, where engine block, pistons, cylinder heads, intake manifolds, crankcases, carburetors, brake valves and callipers join innumerable components in car design importance.

Five Al-Si casting alloys with silicon contents ranging from 7 to 17% were selected for this study: hypoeutectic LP PM319-F, A356-T6 and C354-T6 alloys and hypereutectic AE425 and PM390 alloys, all used extensively in automotive applications. The aim of this work was to investigate the effect of casting defects on the fatigue properties of these alloys by correlating the sample fatigue life with the defect that initiated the fatigue crack, and to characterize these defects (i.e., porosity, oxide films, slip bands, etc.) by their critical role in affecting the fatigue life. Porosity was investigated in terms of the pore size at the sample fracture surface and its location i.e. near the edge or close to the interior. The effect of hot isostatic pressing (HIPping) on the fatigue life of C354-T6 alloy was also studied and the behavior of HIPped and non-HIPped samples compared.

The fracture surfaces of 157 fatigue samples were examined using a scanning electron microscope (SEM technique) to identify the fatigue crack initiation site, supplemented by image analysis for quantitative measurements of the defect(s) that initiated the fatigue crack. The microstructural characteristics (i.e. secondary dendrite arm spacing (SDAS), eutectic silicon particle characteristics, grain size and intermetallic phases) were examined using image analysis and electron probe microanalysis (EPMA) techniques to help in understanding the fatigue behavior.

The results show that surface porosity is the most important casting defect affecting the fatigue life, since it acts as the most favoured site for fatigue crack initiation: among the samples tested, 82% fractured under the effect of surface porosity acting as the fatigue crack initiation site. It was found that the sample fatigue life decreased as the surface pore size increased and vice versa.

In the absence of surface porosity, other casting defects such as oxide films close to the surface can be responsible for fatigue crack initiation: 3% of all tested samples fractured due to the presence of such oxide films. In the absence of porosity and oxide films, slip bands can also act as the main crack initiation site, where, in the present case, it was observed that 3% of all tested samples fractured due to slip bands.

Fatigue crack initiation always starts from the free surface of the sample whatever the crack initiation site (porosity, oxide films, slip bands), where the maximum stress applied is found there and the stress distribution from the surface towards the centre of the sample (sample interior) is favourable for fatigue crack propagation. For the same reason, it is impossible for the fatigue crack to propagate from the sample interior toward the sample free surface, against the stress gradient.

The location of the porosity (i.e. near the edge or close to the interior of the sample) also influences the fatigue behavior. It is found that although non-fractured (run-out) samples do contain porosity, the occurrence of this porosity within the interior of the samples has much less influence on crack initiation than if the porosity were located at the edge of the sample surface, as is the case for the fractured samples.

The SEM technique, by which the porosity measurements were carried out, can be applied with great accuracy for measurements of single pores responsible for fatigue crack initiation. However, when the crack initiation area contains multiple pores (as in the case of LP PM319-F alloy) or a spongy porous structure (as in the case of AE425 alloy), SEM measurements are not adequate enough to determine the exact fatigue crack initiation site. In such cases, the measurements should be carried out using optical microscopy and a longitudinal section of the fractured specimen to provide greater accuracy of results. However, this is a time consuming process.

Hot isostatic pressing (HIPping) is found to improve the fatigue strength of C354-T6 castings by reducing or eliminating the surface porosity, thus increasing the fatigue life. In the absence of surface porosity, other crack initiation sites such as oxide films and slip bands become operative.

Microstructural features such as the eutectic Si particle characteristics, secondary dendrite arm spacing, intermetallic phases, and grain size can influence fatigue life when they strongly affect crack propagation. For hypereutectic alloys, the primary silicon particles contribute to the fatigue behavior by accelerating crack propagation through the decohesion and cracking of these particles under cyclic loading.

# ACKNOWLEDGMENTS

It is a great pleasure to finally have the chance to convey my thanks to all those who were involved in making this work a success. I would like to express my sincere thanks to my supervisors, Professors F.H. Samuel and A.M. Samuel for their help and continuous guidance during the different stages of my work.

Financial support received from the Natural Sciences and Engineering Research Council of Canada (NSERC) and General Motors Powertrain Group (U.S.A.) is gratefully acknowledged.

I would like to thank Dr. Paul Crepeau and Dr. Qigui Wang from General Motors in U.S.A. for their useful discussions and invaluable comments.

I would like to express my appreciation to Madam Helen Campbell, McGill University for her help in the SEM work.

Thanks to Mr. Alain Bérubé and Mr. Mathieu Paradis of the Chair TAMLA group for their assistance in the experimental part of this work.

Finally, I wish to sincerely acknowledge all members of my family who strongly supported me and encouraged me to finish this work.

# TABLE OF CONTENTS

# LIST OF FIGURES

## CHAPTER 2

**CHAPTER 3**



**CHAPTER 4**

# LIST OF TABLES

## CHAPTER 2



## CHAPTER 3



## CHAPTER 4



## APPENDIX A

# LIST OF ACRONYMS

| | |
|---|---|
| AA | Aluminum Association |
| PSBs | Persistent slip bands |
| FCG | Fatigue crack growth |
| UTS | Ultimate tensile strength |
| YS | Yield strength |
| % EL | Percentage elongation |
| SEM | Scanning electron microscopy |
| OM | Optical microscopy |
| EPMA | Electron probe microanalyzer |
| EDX | Energy dispersive X-ray |
| WDS | Wavelength dispersive spectroscopy |
| SDAS | Secondary dendrite arm spacing |
| HCF | High cycle fatigue ($N > 10^4$) |
| LCF | Low cycle fatigue($N < 10^4$) |
| HIP | Hot isostatic pressing |

# LIST OF SYMBOLS

| | |
|---|---|
| $P_g$ | Equilibrium pressure of dissolved gases in the melt |
| $P_s$ | Pressure drop due to shrinkage |
| $P_{atm}$ | Pressure of the atmosphere over the system |
| $P_H$ | Pressure due to the metallostatic head |
| $P_{s\text{-}t}$ | Pressure due to surface tension at the pore/liquid interface |
| $P_i$ | Internal pressure |
| $P_{ext}$ | External pressure |
| $\sigma_{min}$ | Minimum stress |
| $\sigma_{max}$ | Maximum stress |
| $\sigma_r$ | Stress range |
| $\sigma_m$ | Mean stress |
| $\sigma_a$ | Alternating stress |
| R | Stress ratio |
| A | Stress ratio |
| S | Stress amplitude |
| N | Number of cycles |
| $N_f$ | Number of cycles to failure |
| $K_{cr}$ | Critical stress intensity amplitude |

# CHAPTER 1

# DEFINITION OF THE PROBLEM

# CHAPTER 1

# DEFINITION OF THE PROBLEM

## 1.1 INTRODUCTION

In the automotive industry, aluminum-silicon (Al-Si) casting alloys find extensive application, especially due to their high strength-to-weight ratio which increases the performance and fuel economy. Aluminum sand, die, and permanent mold castings are critically important in numerous applications such as engine blocks, pistons, cylinder heads, etc.

The increasing use of Al-Si casting components under conditions of repeated cyclic loading has generated a considerable interest in their fatigue properties. The fatigue performance of these alloys is strongly dependent on two factors: casting defects such as porosity, oxide films and inclusions found in the castings after production, and the quality of the microstructure, viz., the type, size and morphology of the microstructural constituents and features present, such as intermetallics, silicon particles and slip bands.

The main feature of Al-Si casting alloys is that a eutectic is formed between aluminum and silicon at a Si content of 11.5-12%. Depending on the amount of silicon, the alloys are divided into three main groups: hypoeutectic alloys with silicon content between

5 and 10%, eutectic alloys with 11-13% Si, and hypereutectic alloys, commonly with a Si content between 14 and 20%. Aluminum-silicon alloy castings are generally subjected to heat treatments to improve their mechanical properties and dimensional stability. The T6 treatment is the one most commonly used for these alloys. In the present work, the fatigue samples were obtained from castings either in the as-cast (F) condition (i.e. no heat treatment procedure was applied) or in the T6 condition (i.e. solution heat-treated and artificially aged).

Five different Al-Si casting alloys were selected in this work in order to study the effect of casting defects on their fatigue life. The alloys were selected to cover a range of Si contents, and included 319-F, A356-T6, and C354-T6 hypoeutectic alloys, as well as AE425 and 390 hypereutectic alloys. These alloys are used in a wide range of automotive applications, many of them under conditions of cyclic loading, where the cast parts can undergo sudden fracture due to fatigue failure. Therefore, an investigation of the causes of fatigue failure in the context of the casting defects present in these alloys was considered to be important and beneficial from both academic and industrial points of view.

In the present study, fatigue samples derived from actual automotive castings were tested to obtain the fatigue life data. Samples were then sectioned from the fractured fatigue tested specimens for SEM examination (fractography), to determine the sources (or defects) responsible for the fatigue failure. Particular emphasis was given to porosity defects, as porosity is known to play a critical role in affecting the fatigue performance of Al-Si alloys.

Porosity refers to the presence of minute holes or cavities in a solid metal or alloy. To date, it is well understood that porosity in castings is caused by the cooperative effects

of shrinkage and dissolved gases (mainly hydrogen, which has a high solubility in liquid aluminum but a very low solubility in the solid state, giving rise to gas porosity in the solidified casting). Porosity is considered as the major casting defect found in Al-Si casting alloys and plays a critical role in affecting the fatigue life.

## 1.2 OBJECTIVES

The present work aimed at investigating the effect of casting imperfections on the fatigue life of LP PM319-F, A356-T6, C354-T6, AE425, and PM390 Al-Si casting alloys. This was carried out by means of the following steps:

1. Characterization of the fracture surfaces of fatigue specimens and correlation of the defect that initiated the fatigue crack with the sample fatigue life.
2. Classification of the defects according to the importance of their role in fatigue crack initiation; the defects including
    - Porosity;
    - Inclusions and oxides; and
    - Other microstructural constituents and features (*e.g.,* intermetallics, slip bands, and silicon particles).
3. Classification of the porosity characteristics according to their influence on fatigue crack initiation. The porosity parameters examined were pore size (average area and average length) and shape, and pore location (with respect to the free surface of the sample).

4. Determination of a suitable technique for the qualitative and quantitative analysis of the porosity associated with the crack initiation site, based on the fatigue and porosity data obtained.

# CHAPTER 2

# LITERATURE SURVEY

# CHAPTER 2

# LITERATURE SURVEY

## 2.1 INTRODUCTION

Aluminum, the most plentiful metallic element on the earth, became an economic competitor in engineering applications as recently as the end of the 19th century. The properties of aluminum that make this metal and its alloys the most economical and attractive for a wide variety of uses are appearance, light weight (aluminum has a density of only 2.7 g/cm$^3$, approximately one third that of steel (7.83 g/cm$^3$)), fabricability, physical properties (excellent electrical and thermal conductivity), mechanical properties, and excellent corrosion resistance.[1]

Aluminum alloys containing silicon as the major alloying element offer excellent castability, high wear and corrosion resistance, good weldability, good machinability, hot tearing resistance, fluidity, low specific gravity, high thermal conductivity, reduction of thermal expansion (by silicon), and good retention of physical and mechanical properties at elevated temperatures. As a result, aluminum-silicon (Al-Si) alloy castings constitute 85% to 90% of the total aluminum cast parts produced.[2, 3, 4, 5]

The single most critical factor facing the world today is "Energy". The automotive industry has taken a giant step forward in reducing the weight of the car (and hence reducing fuel consumption) by replacing cast and malleable iron castings with Al castings.[6] Studies have shown that, a fuel reduction of 1 liter per 120 km is obtained with a weight reduction of 200 kg. This amounts to 1000 liters over the life of the vehicle. Savings in fuel consumption range from 3,6 to 6,3 liters per kilogram weight reduction per car over its average life (estimated at 120,000 km).[7] Another study has demonstrated that the replacement of steel components by 50 kg of aluminum results in an 850 liter fuel saving over a ten-year period.[3] It is expected that, by 2015, the total weight of aluminum/vehicle will rise to 250 - 340 Kg, as the material for engine blocks, one of the heavier parts, is switched from cast iron to aluminum.[8]

With respect to automotive applications, aluminum sand, die, and permanent mold castings are critically important in engine construction, and include engine block, pistons, cylindrical heads, intake manifolds, crankcases, carburetors, transmission housings, and rocker arms. Brake valves and brake callipers join other components in car design importance.[1]

## 2.2 ALUMINUM CASTING ALLOY DESIGNATION SYSTEM

The most widely used casting alloy designation system in North America is that of the Aluminum Association (AA).[9] In the AA alloy designation, there are four numeric digits, with a period between the third and fourth. The meanings of the four digits are:[9]

- First digit: Principal alloying constituent(s)
- Second and third digits: Specific alloy designation (number has no significance but is unique)
- Fourth digit: Casting (0) or ingot (1, 2) designation

Variations in the composition limits that are too small to require a change in numeric designation are indicated by a preceding letter (A, B, C, etc). The first version of an alloy, say 356.0, contains no letter prefix; the first variation has an A, e.g., A356.0, the second a B, for example, B356.0, and so forth.

The first digit defines the major alloying constituent or constituents, with the following categories being defined:

1xx.x: Pure aluminum (99.00% or greater)

2xx.x: Aluminum-copper alloys

3xx.x: Aluminum-silicon + copper and/or magnesium alloys

4xx.x: Aluminum-silicon alloys

5xx.x: Aluminum-magnesium alloys

6xx.x: Unused series

7xx.x: Aluminum-zinc alloys

8xx.x: Aluminum-tin alloys

9xx.x: Aluminum + other elements

## 2.3 TEMPER DESIGNATION SYSTEM

The Aluminum Association casting temper designation system is used in general for all aluminum and aluminum alloy product forms except for ingot.[5, 9] The system uses letters and numbers to indicate the major types of thermal treatments applicable to engineered castings:[5, 9]

*F, as-cast:* This applies to products for which no heat treatment procedures are carried out.

*O, annealed:* Thus applies to cast products that are annealed to improve ductility and dimensional stability.

*W, solution heat-treated:* This is applicable only to alloys whose strength naturally changes at room temperature over a duration of time.

*T, solution heat-treated:* This applies to alloys whose strength is stable within a few weeks of solution heat treatment. The T is always followed by one or more digits, each digit indicating a specific sequence of basic treatments. Some of these treatments are listed below:

*T4, solution heat-treated and naturally aged to a substantially stable condition:* this signifies products that are not cold worked after solution heat treatment and for which mechanical properties have been stabilized by room temperature aging.

*T5, cooled from an elevated-temperature shaping process and artificially aged:* This includes products that are not cold worked after an elevated temperature shaping process and for which mechanical properties have been improved by precipitation hardening.

*T6, solution heat-treated and artificially aged:* This includes products that are not cold-worked after solution heat treatment and for which mechanical properties and dimensional stability have been improved by precipitation heat treatment.

## 2.4 SELECTION AND APPLICATIONS OF Al-Si CASTING ALLOYS

The main feature of Al-Si casting alloys is that a eutectic is formed between aluminum and silicon at a Si content of 11.5-12%, as illustrated by the phase diagram in Figure 2.1. Depending on the amount of silicon, the alloys are divided into three main groups: hypoeutectic alloys with a silicon content between 5 and 10%, eutectic alloys with 11-13% Si, and hypereutectic alloys, with a Si content commonly between 14 and 20%.[10]

Five Al-Si casting alloys with different silicon contents ranging from 7 to 17% were selected for this study: hypoeutectic LP PM319-F, A356-T6 and C354-T6 alloys, and hypereutectic AE425 and PM390 alloys used extensively in automotive applications.

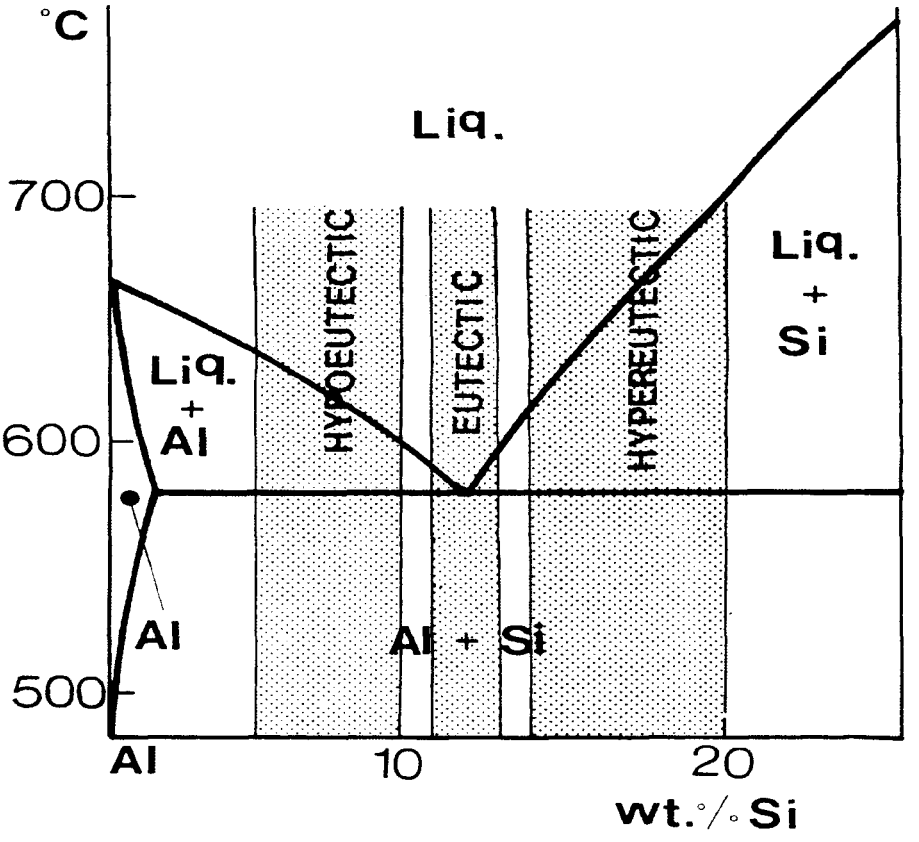


**Figure 2.1** Part of the Al-Si phase diagram showing composition ranges of various alloy types.[10]

### 2.4.1 Al-Si-Cu (319) hypoeutectic casting alloys

Aluminum-silicon-copper alloys such as 319 alloy offer good casting characteristics, higher strength and hardness, and improved machinability with reduced ductility and lower resistance to corrosion.[9] Automotive cylindrical heads, internal combustion engine crankcases, engine blocks, gear cases, impellers, gas meters and regulators, fuel pump, transmission cases, machinery, gear blocks, instrument cases, intake manifolds, lawnmower decks, oil pans, outboard motor propellers, motor parts and housings are among the many applications for which 319 type alloys are used.[5, 9]

### 2.4.2 Al-Si-Cu-Mg (354) hypoeutectic casting alloys

Aluminum-silicon-copper-magnesium alloys such as 354 alloy have a greater response to heat treatment as a result of the presence of both Mg and Cu.[11] These alloy types offer excellent strength and hardness with some sacrifice in ductility and corrosion resistance. While the properties in the as-cast condition are acceptable for some applications, these alloys are typically heat treated for optimal properties. These alloys are used for a wide range of applications, including engine cooling fans, crankcases, high speed rotating parts (e.g., fans and impellers), structural aerospace components, air compressor pistons, fuel pumps, compressor cases, timing gears, rocker arms, and machine parts.[9]

### 2.4.3 Al-Si-Mg (356) hypoeutectic casting alloys

Aluminum-silicon-magnesium alloys such as 356 alloy have excellent casting characteristics, weldability, pressure tightness, and resistance to corrosion. These alloys are heat treatable to provide various combinations of tensile and physical properties that are attractive to many applications including machinery, and automotive, military, and aerospace parts. Some typical uses include aircraft pump parts, automotive transmission cases, aircraft fittings and control parts, water-cooled cylindrical blocks, automotive space frames, automotive wheels, truck wheels, cylinder heads, compressor body, machine parts, pump bodies, meter bodies, intake manifolds, suspension saddles, aircraft pylons, truck and bus frames and chassis components, electronic cases, and fuel pumps.[5, 9, 11]

### 2.4.4 Al-Si-Cu-Mg (390 and AE425) hypereutectic casting alloys

Hypereutectic aluminum-silicon-copper-magnesium 390 and AE425 type alloys, containing silicon concentrations >12% Si, have outstanding wear resistance, a lower thermal expansion coefficient, low specific gravity, very good casting characteristics, and elevated temperature strength. Some typical applications include automotive cylindrical blocks, pistons, brake rotors, cylinder liners, marine engines, four cycle air-cooled engines, air compressors, pumps requiring abrasive resistance, pulleys, and brake shoes.[5, 9, 11]

Numerous studies on the occurrence of porosity in Al-Si alloys and the factors controlling its formation were carried out as presented in the following sections.

## 2.5 POROSITY FORMATION IN Al-Si CASTING ALLOYS

Porosity is the most common defect found in Al-Si alloys, and is the major cause of rejection of castings. Porosity is the term used to indicate voids or cavities that form within a casting during solidification. It is often the cause of degraded mechanical properties in rejected castings, including limited strength and ductility, variable fracture toughness, irregular crack initiation and propagation characteristics, and lack of pressure tightness.[3, 12, 13, 14]

Two main effects contribute to the formation of porosity in Al-Si alloys during solidification: (i) shrinkage resulting from the volume contraction accompanying solidification, as well as inadequate liquid metal mobility (bad feeding), and (ii) gas evolution (mainly hydrogen) resulting from the decrease in gas solubility in solid metal compared to the liquid.[15, 16, 17, 18, 19]

### 2.5.1 Types of porosity

Depending on the origin, porosity may be classified into three types.[3]

*Pure shrinkage porosity:* Macroscopic voids found in the casting are almost always due to shrinkage caused by poor feeding.[3] Shrinkage occurring during the solidification of Al-Si casting alloys is a primary source of porosity formation in solidifying castings. Volumetric shrinkage in metals on transforming from liquid to solid state may range from 3-10%, with 5-8% being typical of most cast alloys. Shrinkage porosity can occur on a much smaller scale in the form of dispersed "microshrinkage" or "microporosity". Liquid metal feeding in the dendritic solidification zone plays a key role in the formation of this type of porosity.[15] The tendency for the formation of shrinkage porosity is related to both the liquid/solid volume fraction at the time of final solidification and the solidification temperature range of the alloy.[9] An example of a shrinkage pore found within a casting is shown in Figure 2.2(a).

*Pure gas porosity:* The other main source of porosity arises from the entrapment of a gas bubble in the solidifying alloy resulting from the decrease in the solubility of the gas on solidification.[3, 19] Hydrogen is the only gas soluble in aluminum alloys and is thus the leading contributor to porosity in these alloys.[20] An example of a gas pore found within an Al-8% Si alloy casting is shown in Figure 2.2(b).

*Porosity due to gas and shrinkage:* The vast majority of porosity encountered in castings is due to a combination of gas and shrinkage. These pores typically occur in the interdenderitic regions, which are the last parts of the structure to freeze.[3] Some examples are shown in Figure 2.2(c) and (d).

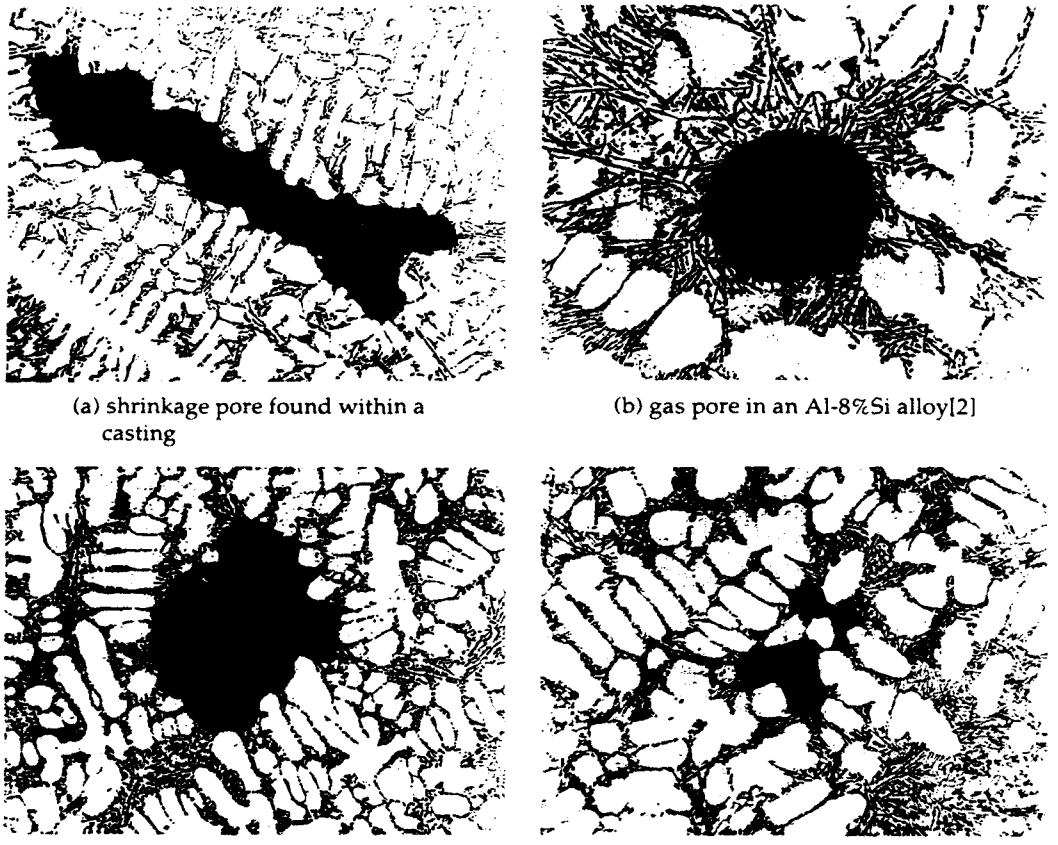

(a) shrinkage pore found within a casting

(b) gas pore in an Al-8%Si alloy[2]

(c) microporosity (gas plus shrinkage)

(d) microporostiy (gas plus shrinkage)

**Figure 2.2** Typical porosity in cast aluminum alloys.[3]

### 2.5.2 Theory of porosity formation

The following equation can be considered to describe the conditions under which a pore is stable and can grow.[3, 21]

$$P_g + P_s \geq P_{atm} + P_H + P_{s\text{-}t}$$

where $P_g$ = equilibrium pressure of dissolved gases in the melt;

$P_s$ = pressure drop due to shrinkage;

$P_{atm}$ = pressure of the atmosphere over the system;

$P_H$ = pressure due to the metallostatic head;

$P_{s\text{-}t}$ = pressure due to surface tension at the pore/liquid interface.

In order for a pore to exist, its internal pressure ($P_i = P_g + P_s$) must be sufficient to overcome all the external forces ($P_{ext} = P_{atm} + P_H + P_{s\text{-}t}$) which can act to make it collapse. The dissolved gas pressure $P_g$ and the pressure drop due to shrinkage $P_s$ are the main driving forces for porosity formation.

### 2.5.3 Effect of hydrogen

As mentioned above, hydrogen is the only gas soluble in aluminum alloys and is thus the leading contributor to gas porosity in these alloys. As Figure 2.3 shows, the sharp decrease in hydrogen solubility in going from the liquid to the solid state results in the rejection of the dissolved hydrogen with the progress of solidification and, hence, the formation of gas porosity. As can be seen, both the temperature and the presence of alloying elements and impurities affect the solubility (and hence the porosity).[22] There are many potential sources of hydrogen contamination in aluminum including:[9]

i) The atmosphere;

ii) Incompletely dried refractories;

iii) Fluxes;

iv) Tools, flux tube, and ladles;

v) Products of combustion in gas-fired furnaces;

vi) Remelt ingots, master alloys, metallurgical metals, and other charge components.

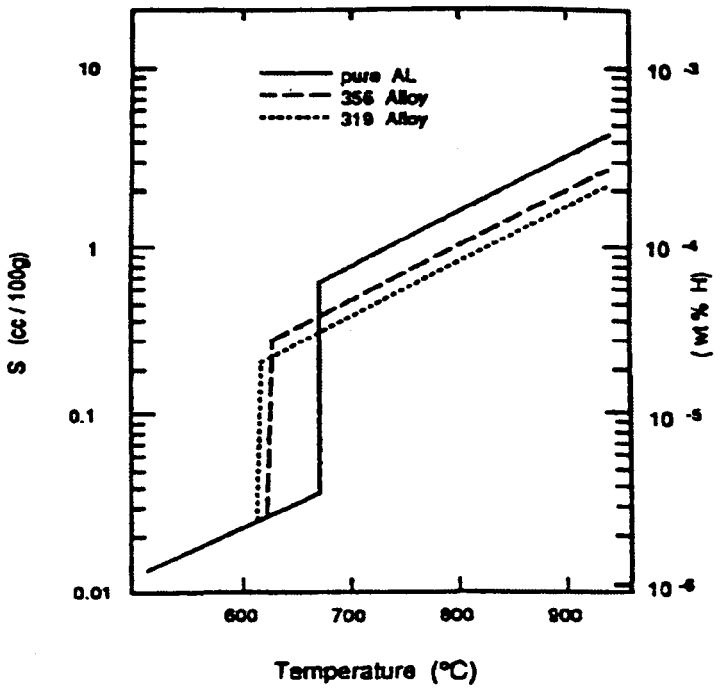


**Figure 2.3** The solubility of hydrogen in pure aluminum, and 319 and 356 aluminum alloys.[22]

Most hydrogen which finds its way into molten aluminum comes from the dissociation of water vapor at the surface of the liquid aluminum according to the reaction[23]

$$2Al\ (Liquid) + 3H_2O \rightarrow Al_2O_3 + 6H$$

where hydrogen gas dissolves in liquid aluminum according to an atomistic process that involves the following steps:[22]

(i) Dissociation of diatomic hydrogen gas into the atomic form at the boundary between the atmosphere and the melt;

(ii) Dissolution of the atomic hydrogen into the boundary layer; and

(iii) Transport of atomic hydrogen into the bulk of the melt through a diffusion process.

Rooy [24] proposed the following steps for hydrogen gas formation in molten aluminum:

(i) The diffusion of hydrogen atoms within the liquid pool;

(ii) The formation of subcritical nuclei as a function of time and cooling;

(iii) The random emergence of stable precipitates exceeding the critical size required for sustained growth;

(iv) Continued growth of the precipitated phase as long as hydrogen atoms are free to diffuse to the melt/bubble interface.

The result of this sequence is a general distribution of voids occurring throughout the solid structure. A schematic representation is provided in Figure 2.4.

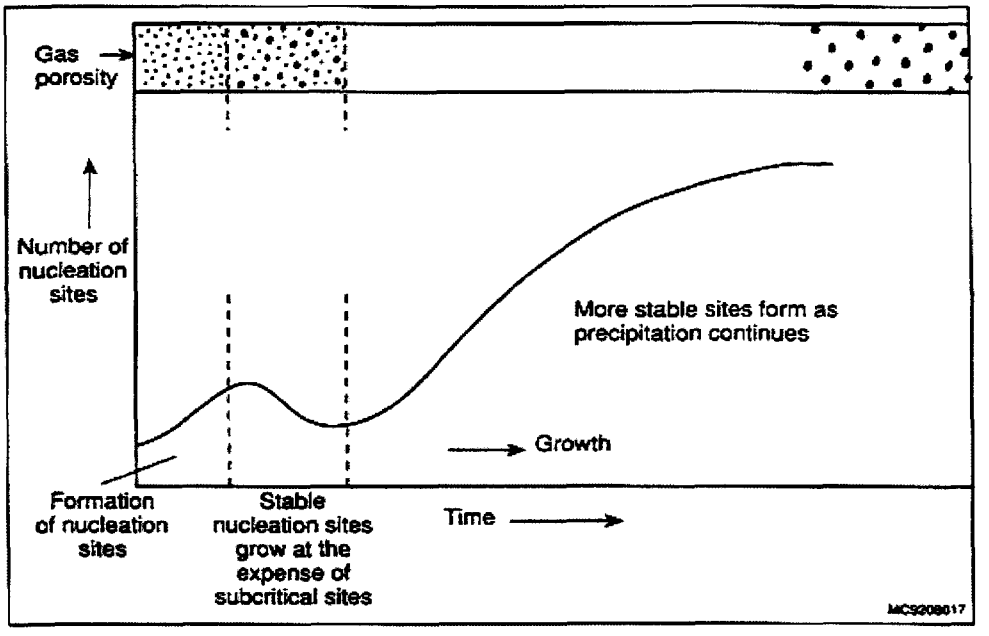


**Figure 2.4** Schematic diagram showing the effect of nucleation sites on porosity development.[24]

Fang and Anyalebechi [25] studied the effect of hydrogen content and cooling rate on porosity formation in Al-4.7 Mg and A356 alloys. They observed that the pore volume fraction always decreased as the cooling rate increased, and that the amount of reduction depended on the hydrogen content at each cooling rate as depicted in Figure 2.5, where curves 3, 4 and 5 show lower pore volume fractions due to their lower hydrogen contents. As Figure 2.6 shows, the pore volume fraction increases as the hydrogen content increases, and the slopes of the corresponding curves increase rapidly with the decrease in cooling rate. There exists a corresponding threshold hydrogen concentration for a given residual pore volume fraction at a given cooling rate for each alloy. A higher cooling rate gives a higher threshold value.

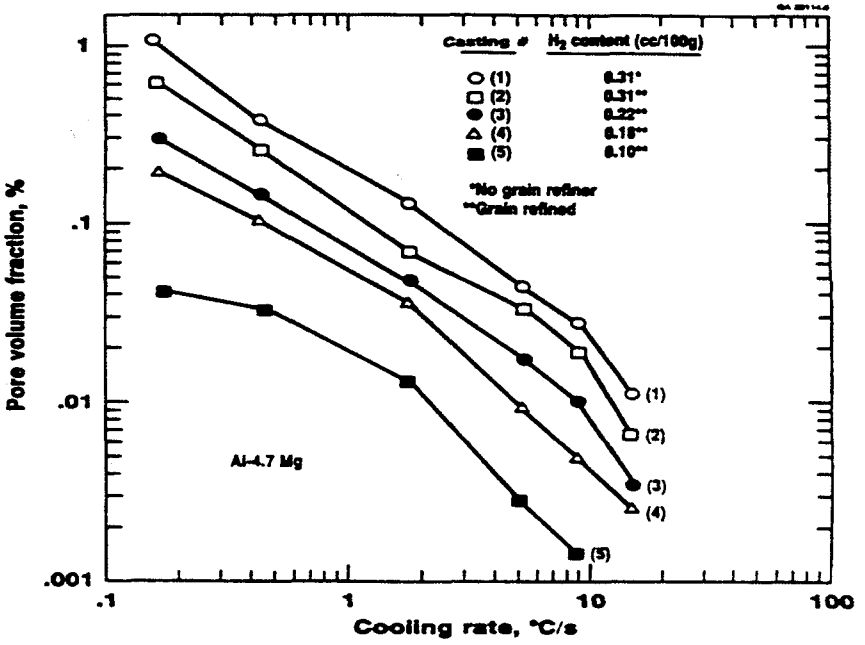


**Figure 2.5** Effect of hydrogen level and cooling rate on pore volume fraction obtained in A-4.7 Mg castings.[25]

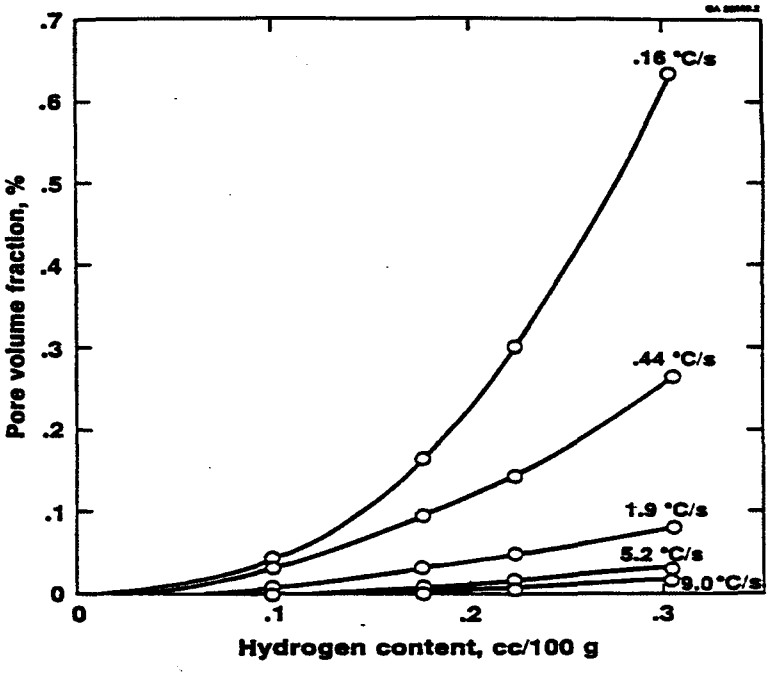


**Figure 2.6** Pore volume fraction as a function of hydrogen content at different cooling rates in grain refined Al-4.7 Mg alloy.[25]

### 2.5.4 Effect of modification

The addition of certain elements termed modifiers to Al-Si casting alloys aims at improving their mechanical properties by changing the morphology of the normally acicular eutectic silicon to a fine, fibrous form that improves the alloy ductility and strength. Only sodium (Na), strontium (Sr) and antimony (Sb) have found significant industrial use.[3] Today, due to its advantages compared to other modifiers, strontium is the modifier of choice for Al-Si castings in many foundries. However, it is generally agreed that the addition of Sr increases the porosity in a casting. Various explanations have been proposed, as summarized below.[26]

*Depression of the eutectic temperature and concomitant morphological change*

Addition of Sr is observed to result in a depression of the silicon eutectic temperature, as shown in Figure 2.7. This depression is considered as one of the reasons for the change in the porosity level observed. As can be seen, the depression extends the alloy freezing range (i.e., extends the length of the mushy zone), leading to an increase in the solidification time, resulting in larger pores.[27, 28, 29]

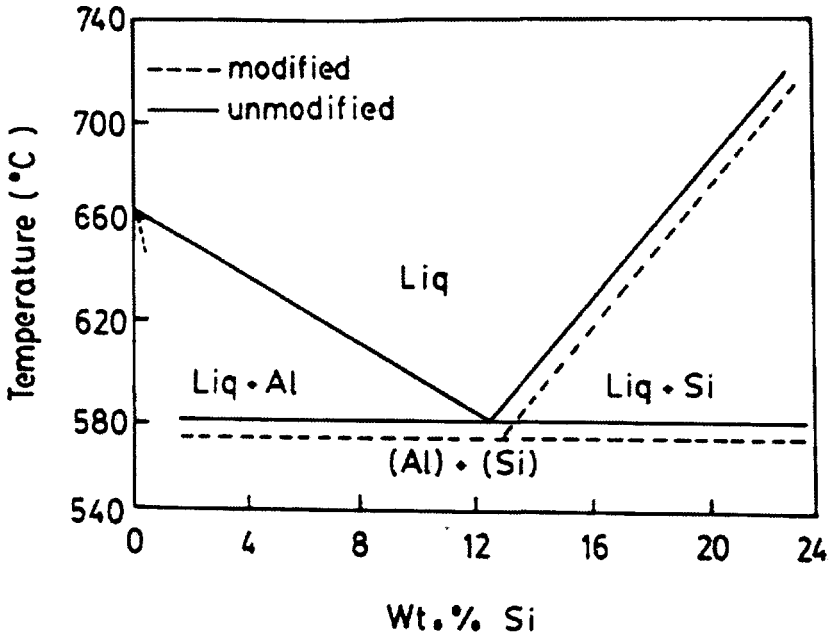


**Figure 2.7** Suppression of the eutectic temperature due to modification.[29]

Argo and Gruzleski[29] found that the formation of microshrinkage is a two-stage process involving both interdenderitic feeding and eutectic solidification. For the unmodified alloys, the interdendritic feeding distance is short, leading to an easy feeding which concentrates any porosity in the last solidified region of the casting. As this area is reached, an irregular solidification of the final eutectic liquid causes small pockets of eutectic to become trapped behind the advancing solid/liquid interface, resulting in fine porosity. In the modified alloy, the interdenderitic feeding distance is relatively long as a result of the depression of the eutectic temperature, where the longer mushy zone makes feeding more difficult and the possibility of larger isolated pockets of eutectic liquid being trapped in the interdenderitic regions more likely. A schematic representation of their explanation is shown in Figure 2.8.

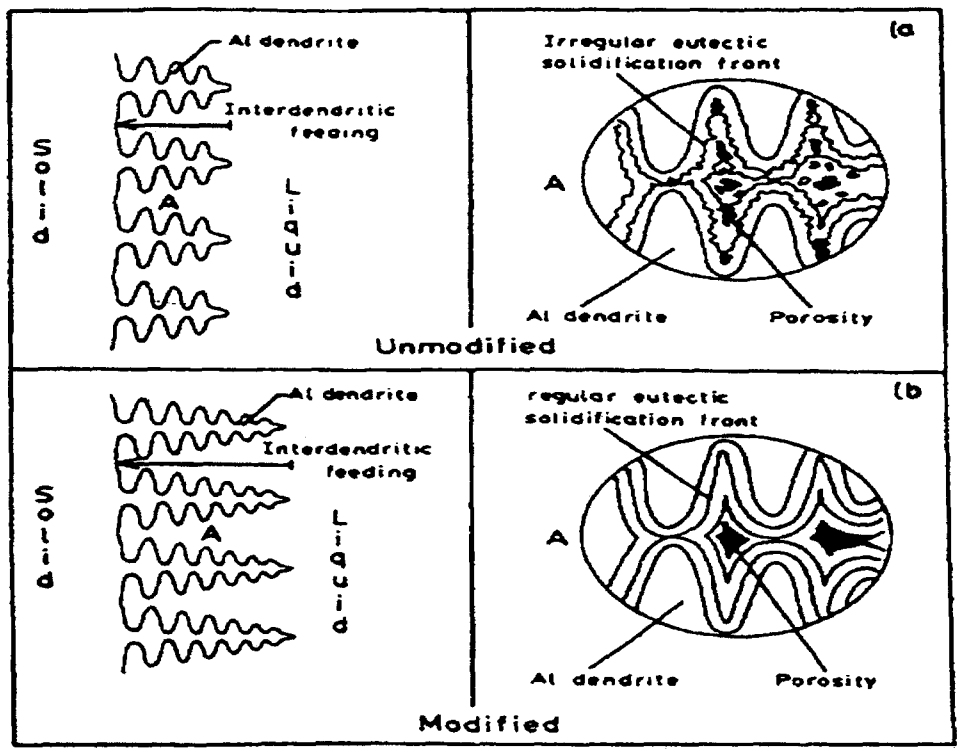


**Figure 2.8** Two-stage solidification process showing microshrinkage formation in: a) an unmodified casting with a short interdenderitic feeding distance and an irregular eutectic solidification front, and b) a modified casting with a long interdenderitic feeding distance and a regular eutectic solidification front.[29]

*Reduction of interfacial energy and increase in volumetric shrinkage*

Sr modification reduces the surface tension of an aluminum melt which facilitates pore nucleation, thereby increasing the pore volume fraction and pore size.[27] Emadi *et al.*[30] measured the effect of Sr and Na modification on the interfacial energy and volumetric shrinkage of aluminum. They concluded that these two elements decreased the surface tension of the liquid and increased the volumetric shrinkage, facilitating porosity formation and increasing the pore size and amount of porosity observed. Addition of about 0.01 wt

pct Sr and about 0.005 wt pct Na respectively caused about 19% and 10% reductions in the surface tension of the liquid, and increased the volume shrinkage by about 12%.

*Enhanced hydrogen solubility in the melt*

A modification treatment with either Na or Sr could increase the hydrogen content of a liquid alloy due to one or a combination of the following: [3]

(i) The direct addition of hydrogen to the melt along with the modifier;

(ii) An increase in the rate of hydrogen pick-up by the modified melt;

(iii) An increase in the hydrogen solubility of the modified melt.

Bian *et al.*[31] found that Sr addition markedly increases the hydrogen content in Al-Si melts and accelerates the gassing rate of the melt. In contrast, in unmodified melts the hydrogen level decreases with time, finally reaching a stable level, as shown in Figure 2.9.

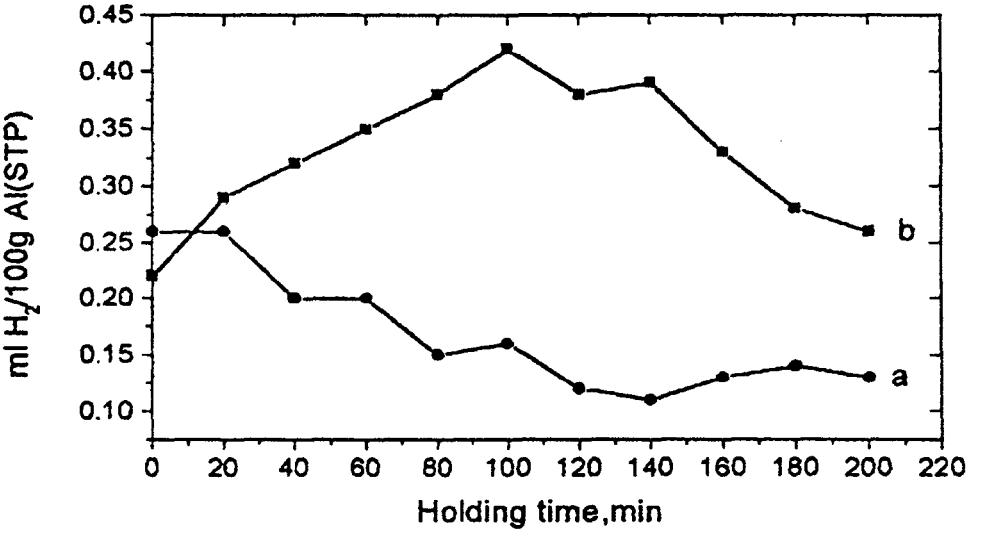


**Figure 2.9** Hydrogen content vs. holding time in the unmodified and modified Al-10 wt%Si melts. Holding temperature: 750°C, a) Unmodified, b) Modified with addition of 0.05 wt%Sr at 720°C.[31]

*Changes in the concentration and type of the oxide formed*

Addition of Sr to the melt increases the tendency for oxide formation due to the high affinity of oxygen for Sr. Liu *et al.* [32] reported that the microporosity observed in Sr-modified alloys is frequently associated with Sr oxides (films or particles). These particles/films are formed during melting due to the high oxygen affinity of Sr. The stoichiometric composition of these oxides was found to be $Al_{2.3}SrO_{3.3}$ or $Al_2SrO_3$, from wavelength dispersion spectroscopic (WDS) analysis.

### 2.5.5 Effect of grain refining

Grain refining is another important melt treatment carried out for Al-Si alloys to refine the grain size in the cast structure, a small grain size being known to enhance the alloy properties. The grain refining is carried out by the addition of grain refiners, usually Al-Ti, Al-Ti-B or Al-B master alloys, to the Al-Si alloy melt, which introduces $TiAl_3$ and $TiB_2$ particles in the melt, these being known to act as nucleation sites for the primary $\alpha$-Al dendrites. The introduction of a large number of these nuclei assists in significantly increasing the number of grains formed, thus refining the grain size. Addition of $TiB_2$ as a grain refiner results in increasing nucleation sites as well as the number of grains, which lead to a remarked reduction in pore size with an increase in the pore density.[16]

Lee and Sridhar [28] found that the addition of $TiB_2$ to Al-Si casting alloys as a grain refiner has the effect of increasing the pore density and the pore nucleation temperature, while decreasing the pore length. They attributed this to (a) a greater supersaturation due to more nucleated grains causing a higher fraction solid at a given temperature and, hence, an

increase in H content in the liquid during the initial stages of solidification, or (b) the effect of $TiB_2$ as a nucleation agent for pores. A combination of these is also possible.

### 2.5.6 Effect of alloying elements

Magnesium and copper are two important alloying elements generally added to Al-Si alloys to improve their properties through precipitation hardening following heat treatment. The addition of magnesium is known to reduce the percentage porosity without a noticeable change in the pore size or shape.[33] Dash and Makhlouf[34] found that copper has a negative effect on porosity formation. Copper has two important effects: (i) it significantly increases the hydrogen gas pressure associated with a given amount of dissolved gas, and (ii) its presence in the melt results in a ternary eutectic reaction that occurs at much lower temperatures than the solidification of both primary $\alpha$ -Al and the Al-Si eutectic.

$$\text{Liq} \rightarrow \quad \alpha\text{-Al} + \text{Si} + \text{Al}_2\text{Cu}$$

This ternary liquid solidifies when the bulk of the casting is already solid and thus this part of the liquid is very difficult to feed where there is no liquid metal flow.

### 2.5.7 Effect of iron

The presence of impurity or trace elements in an alloy can affect the microstructure and, consequently, its properties. Among the impurity elements present in Al-Si alloys, iron is perhaps the most deleterious as, together with other alloying elements, it leads to the formation of intermetallics among which the $\beta$-$Al_5FeSi$ iron intermetallic phase, due to its brittle platelet form, is detrimental to the alloy properties. The presence of these platelets limits the flow of the liquid metal in the surrounding areas, leading to feedability-related

porosity formation in the solidified casting. The addition of 'neutralizing' elements such as Mn or Cr helps in controlling the precipitation of iron in the script-like $\alpha$-$Al_{15}(Fe,Mn)_3Si_2$ from which, due to its more compact morphology, is less harmful to the properties.

In their studies on porosity formation in 380 type aluminum alloys, Roy *et al.*[16] reported that the $\beta$-$Al_5FeSi$ platelets (which appear as needles in an optical micrograph) are very active sites for pore nucleation. Figure 2.10 shows clearly how pores nucleate along the sides of the $\beta$-iron intermetallic needles. On the other hand, these $\beta$-needles also limit the growth of both gas and shrinkage pores, as illustrated in Figure 2.11.

Taylor *et al.* [35] studied the role of iron in the formation of porosity in Al-Si-Cu-based casting alloys. They found that iron exhibits a strong threefold influence on porosity and shrinkage defect formation:

(i) The overall porosity level decreases with iron content until a minimum value occurs at 0.4 pct Fe, as shown in Figure 2.12. As further additions are made, the overall porosity level increases.

(ii) A change in the pore morphology from discrete isolated pores to spongy interdenderitic pores occurs even at small, deliberate additions of iron. These spongy regions become increasingly connected as the iron content increases above 0.4 pct.

(iii) Under the poorest cooling and feeding conditions, increases in iron content above 0.4 pct lead to the development of a major, localized shrinkage defect.

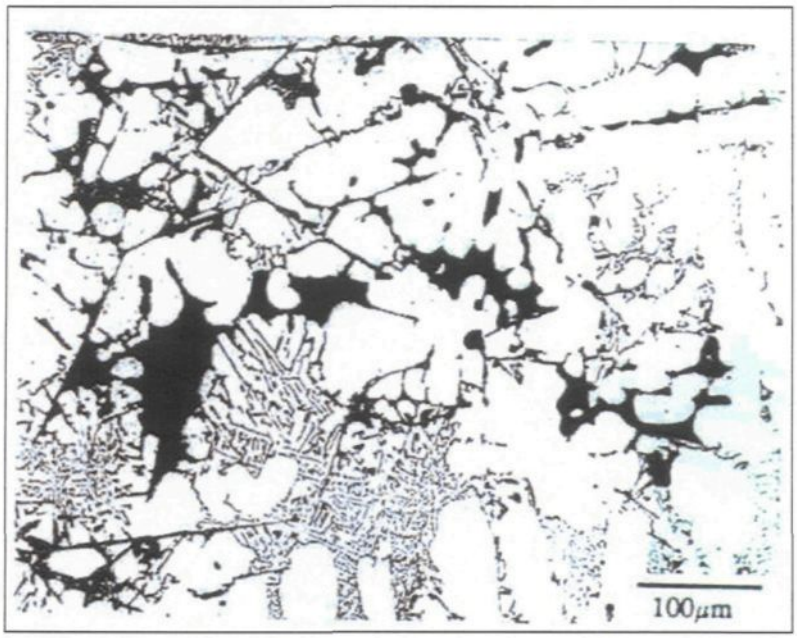


**Figure 2.10** Nucleation of pores along the long sides of $\beta$ needles. [16]

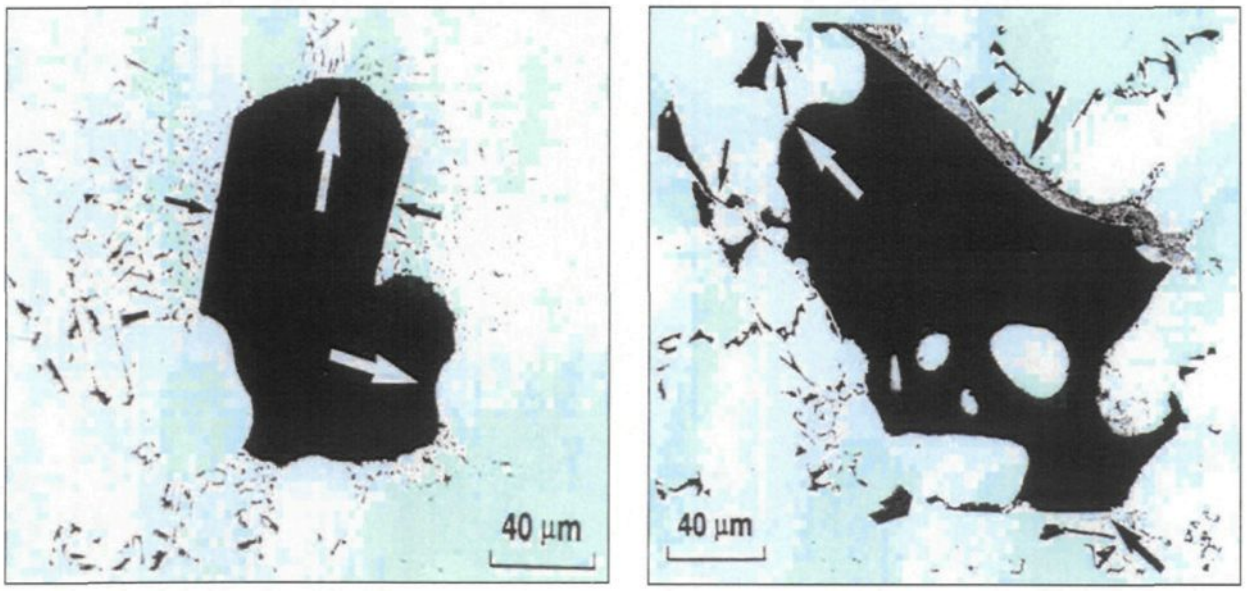


**Figure 2.11** Role of $\beta$-$Al_5FeSi$ needles in the restricting the growth of (a) a gas pore, and (b) a shrinkage pore.[16]

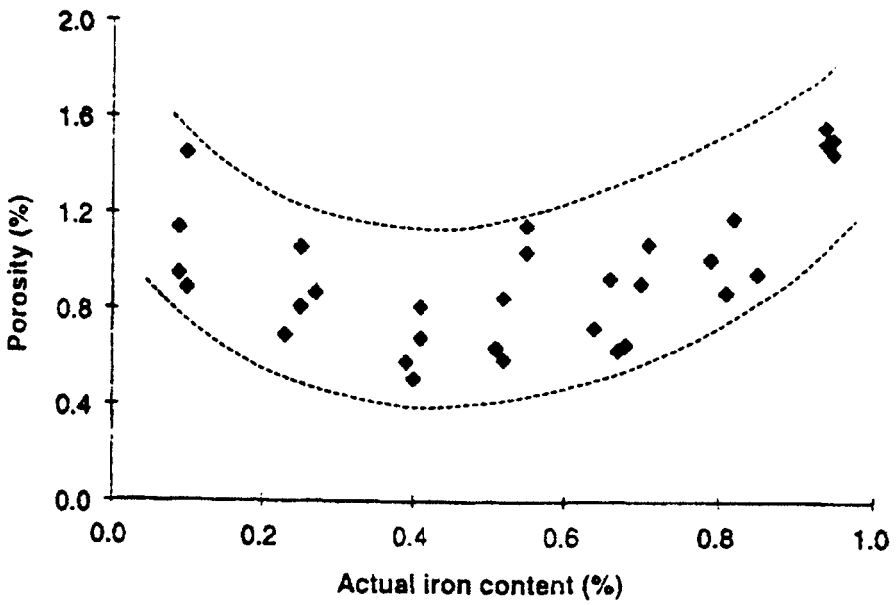


**Figure 2.12** The average total porosity level vs. the actual iron content. [35]

### 2.5.8 Effect of inclusions

Pore nucleation is also influenced by the presence of impurities viz., surfaces of gas bubbles and solid inclusions within the melt, as well as other surfaces such as the mold wall (i.e., the crevices and irregularities present on the mold surface).[36] The presence of inclusions in the melt leads to problems in the casting in terms of casting quality and machinability-related tool wear. In addition, such inclusions also affect porosity formation in that they act as nucleation sites and increase the amount of porosity observed in the casting.

The inclusion level present in the molten metal determines the melt cleanliness, and processes such as degassing and filtration are applied to the liquid metal to minimize the amount of gases and inclusions present in the melt before pouring/casting is done. Melt

cleanliness, particularly in the context of oxides and inclusions, is well recognized as an important factor influencing hydrogen gas nucleation in the melt (and hence porosity).[37, 38]

Tian *et al.* [38] studied the effect of melt cleanliness on the formation of porosity defects in automotive aluminum high pressure die castings, and found that the probability of rejection due to excessive porosity present at critical locations in the castings increased as the number of inclusions in the melt increased. They also observed that the effect of inclusions on porosity formation depends not only on the number, size and spatial distribution but also on the nature i.e., type and shape of the inclusions.

Laslaz and Laty [39] studied the effect of metal cleanliness in aluminum casting alloys and provided experimental evidence of the effect of inclusions or oxides on porosity. They reported that melts that are deliberately oxidized by addition of chips or by stirring in natural atmosphere lead, after solidification, to a higher gas porosity level than the reference melt for the same hydrogen content, where the number of pores is increased in the case of the oxidized melt, all other parameters remaining constant. Also the shape of the pores is rounder in comparison, due to the presence of many oxide/inclusion nucleation sites.

### 2.5.9 Effect of mold design

The design of a mold comprises many parameters including the mold type (material/casting process used), the mold shape, application of chilling and insulation, and the gate and riser design (gating system). All these parameters affect the solidification and feeding conditions of the melt and, as a result, the soundness of the casting produced. Irani

and Kondic [40] reported that thin sections are generally sounder than thick sections in a casting, as determined by the porosity level observed in these sections. This is related to the solidification time, as shown in Figure 2.13, which decreases as the cooling rate increases, which is the case with thinner sections (see Figure 2.5 and Figure 2.6).

The section geometry also affects the feeding conditions and hence the porosity level of the casting. The authors[40] suggested that the casting soundness could be improved by using a tapered form of the feeder. The application of chilling and insulation also affect the solidification time and, consequently, the casting soundness. The appropriate location and sizing of risers is thus very important in the production of high-quality castings.[41]

Sigworth and Caceres [42] reported that in directionally solidified castings, a significant increase in the amount of dispersed microporosity is observed when moving from a location near the chill to a location near the riser. This can create problems in alloys which have extremely long freezing range, in that the riser section may become mushy and stiff long before the interior of the casting freezes completely.

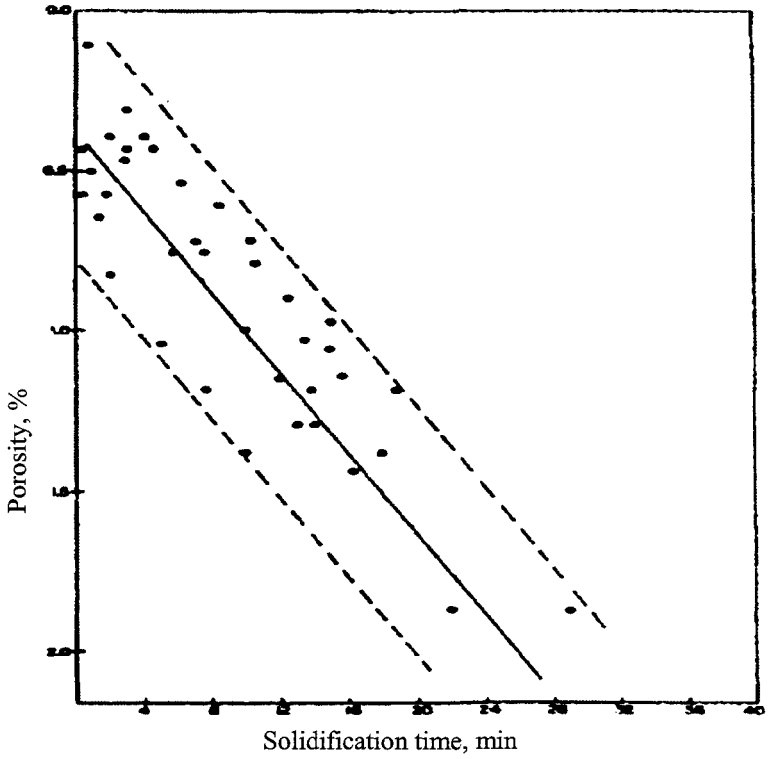


**Figure 2.13** Effect of solidification time on porosity of Al-Cu-Si alloys.[40]

## 2.6 FATIGUE PROPERTIES

Fatigue is considered the most common mechanism by which engineering components fail, and accounts for at least 90% of all service failures due to mechanical causes. Failures occurring under conditions of dynamic loading are termed fatigue failure. A fatigue failure is particularly insidious because it occurs without any obvious warning, resulting in sudden or catastrophic failures.[43] Fatigue can be defined as "the process of progressive localized permanent structural change occurring in a material subjected to conditions that produce fluctuating stresses and strains at some point or points and that may culminate in cracks or complete fracture after a sufficient number of fluctuations".[44]

Three factors are necessary for the occurrence of fatigue failure:[43]

(i) A maximum tensile stress of sufficiently high value;

(ii) A large variation or fluctuation in the applied stress; and

(iii) A sufficiently large number of cycles of the applied stress.

The fatigue process can be roughly divided into four stages: cyclic hardening/softening, crack nucleation, crack propagation, and overload (fracture). At low amplitudes, the nucleation stage can occupy the majority of the fatigue life time, while at high amplitudes nucleation is usually accomplished within a small fraction of the fatigue life.[44]

### 2.6.1 General types of stress cycles causing fatigue failure

Figure 2.14 illustrates the three main types of fluctuating stress cycles which can cause fatigue failure.[43] These constitute:

(i) A completely reversed stress cycle of sinusoidal form, shown in Figure 2.14(a), in which the minimum stress and maximum stress are equal.

(ii) A repeated stress cycle, illustrated in Figure 2.14(b), in which the maximum and minimum stress are not equal.

(iii) An irregular or random stress cycle, as shown in Figure 2.14(c), a complicated type of stress cycle which might be encountered in a part such as an aircraft wing that is subjected to periodic unpredictable overloads due to gusts.

A fluctuating stress cycle can be considered to be made up of two components, a mean stress, $\sigma_m$, and an alternating stress, $\sigma_a$. Taking into consideration the maximum

stress, $\sigma_{max}$, the minimum stress, $\sigma_{min}$, and the stress range $\sigma_r$ (defined as $\sigma_{max}$-$\sigma_{min}$), $\sigma_m$ and $\sigma_a$ are defined as follows:

$$\text{Mean stress, } \sigma_m = \frac{\sigma_{\max} + \sigma_{\min}}{2}$$

$$\text{Alternating stress, } \sigma_a = \frac{\sigma_r}{2}$$

Fatigue data is generally presented in terms of the stress ratio, R, and A, where these terms are defined as:

$$R = \frac{\sigma_{\min}}{\sigma_{\max}}, \text{ and } A = \frac{\sigma_a}{\sigma_m}.$$

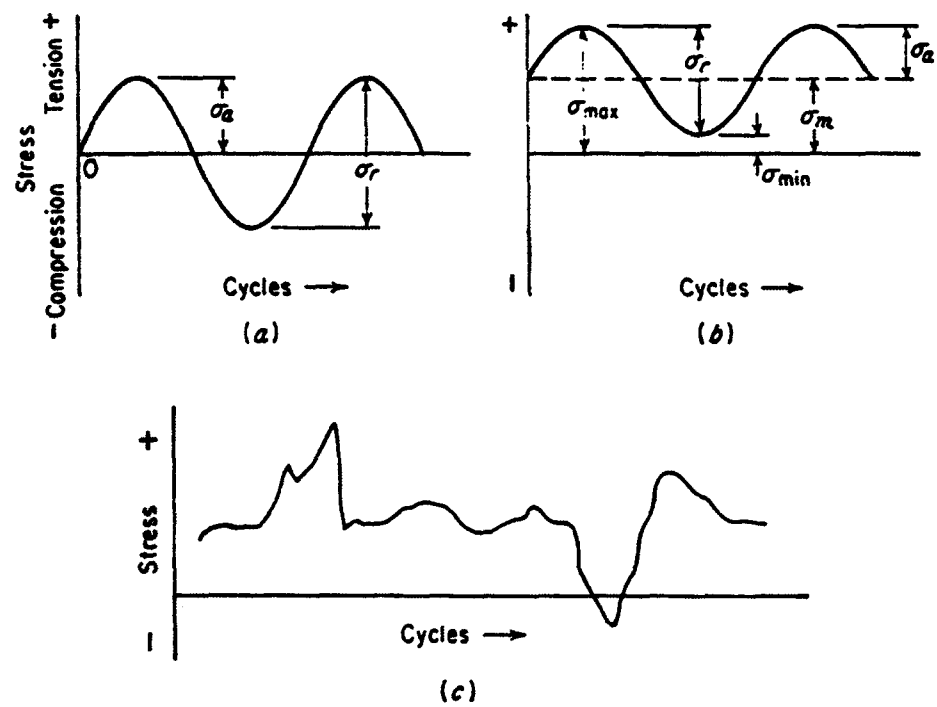


**Figure 2.14** Typical fatigue stress cycles: (a) Reversed stress cycle; (b) Repeated stress cycle; and (c) Irregular or random stress cycle.[43]

### 2.6.2 The S-N curve

The basic method for presenting engineering fatigue data is the S-N curve, which is a plot of stress ($\sigma$) against the number of cycles to failure (N), as shown in Figure 2.15. A log scale is almost always used for N. The value of stress that can be plotted is $\sigma_{max}$, $\sigma_{min}$ or $\sigma_a$. The S-N relationship is determined for a specified value of mean stress $\sigma_m$ and stress ratio R. For a few important engineering materials such as steel and titanium, the S-N curve becomes horizontal at a certain limiting stress, termed the fatigue or the endurance limit, at which the material can endure an infinite number of cycles without failure. Most non-ferrous metals like aluminum, magnesium, and copper alloys, however, do not have a true fatigue limit as the S-N curve never becomes horizontal.[43]

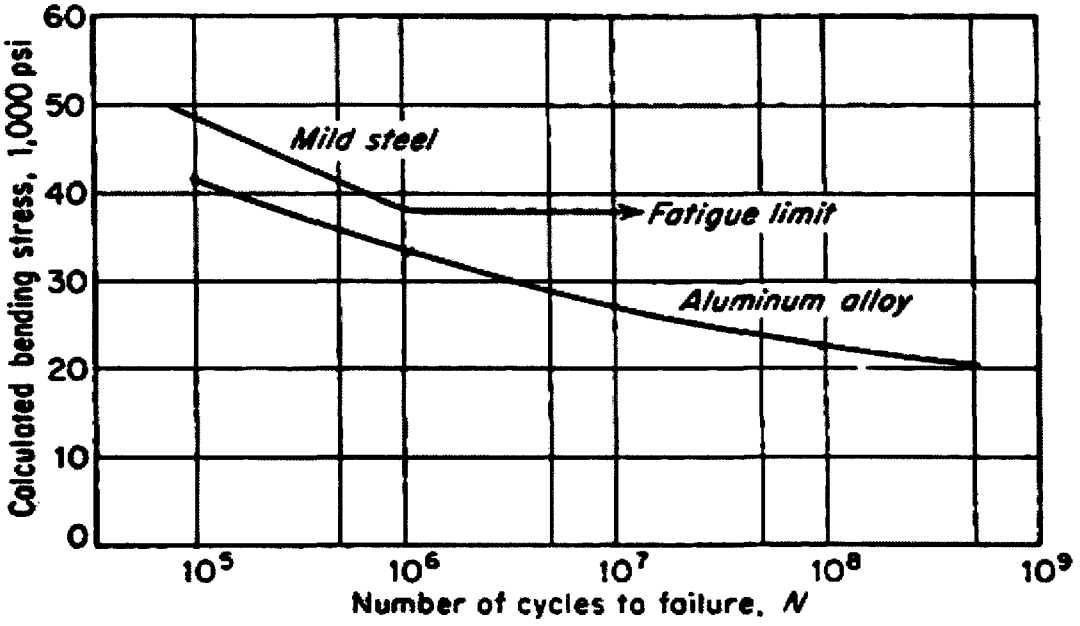


**Figure 2.15** Typical fatigue curve for ferrous and nonferrous metals.[43]

### 2.6.3 Fracture characteristics of fatigue failure

On the macroscopic scale, a fatigue failure can usually be recognized from the appearance of the fracture surface, which consists of two main region: (i) a smooth region, due to the rubbing action as the crack propagates through the section (top portion of Figure 2.16), and (ii) a rough region, where the component has failed in a ductile manner when the cross section is no longer able to carry the applied load. The progress of the fracture is indicated by a series of rings, or "beach marks" progressing inward from the point of initiation of the failure.[43] Fracture surfaces similar to that shown in Figure 2.16 are often called typical fatigue failures because they exhibit the following common features:[45]

(i) A distinct crack nucleation site (or sites);

(ii) Beach marks indicative of crack growth; and

(iii) A distinct final fracture region.

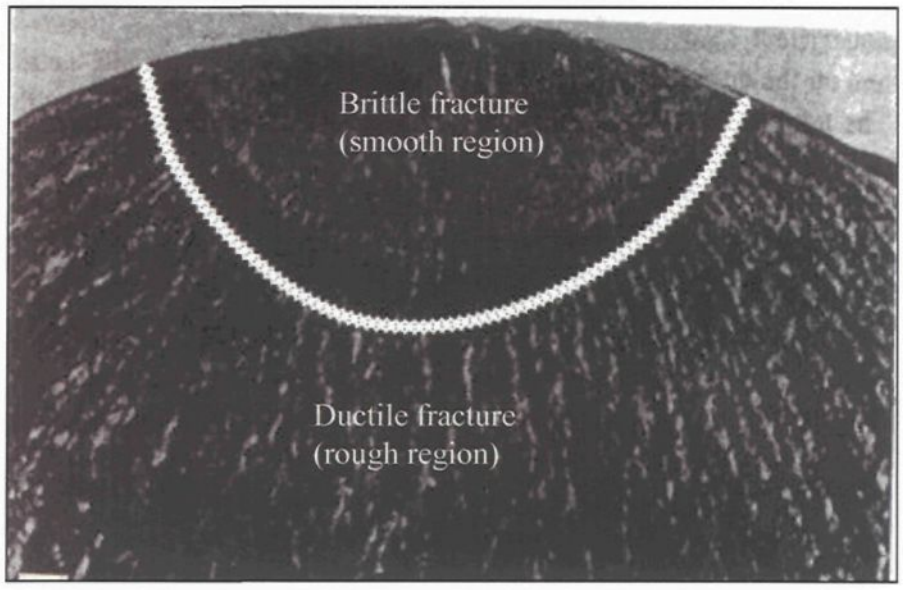


**Figure 2.16** Fatigue fracture surface of a torsion shaft.[45]

### 2.6.4 Factors affecting fatigue life of aluminum alloy castings

The general factors affecting fatigue life of cast aluminum alloys include the stress amplitude, mean stress, stress concentration, surface effects (surface roughness, stress raiser at the surface, surface hardening), size and design of the component, effects of environment (corrosion, oxidation, fretting, temperature), thermal stresses, and the effect of metallurgical variables.[43, 45] The metallurgical factors taken into account to ensure optimum fatigue performance include heat treatment, alloying additions, stacking fault energy, grain size, and inclusion and porosity content. The present work concentrated on the effect of porosity on the fatigue life of the five cast aluminum alloys that were studied.

## 2.7 EFFECT OF POROSITY ON FATIGUE PROPERTIES OF Al-Si CASTING ALLOYS

The presence of porosity - either gas or shrinkage type, is one of the potentially damaging factors with respect to casting quality. While porosity can be detrimental to a casting by reducing its pressure tightness or its surface quality after machining, its effect on the mechanical properties is of critical importance. Numerous studies have shown that porosity plays an important role in determining the fatigue performance of Al-Si casting alloys.

Wickberg *et al.*[46] studied the effect of porosity on fatigue strength of A356 alloy. Figure 2.17 shows the fatigue behavior of A356-T6 alloy specimens with different porosity levels in terms of S-N curves. The porosity levels were varied by adding hydrogen gas to the alloy melt. The corresponding porosity ratings according to ASTM E155 and volume fractions measured from polished sections are listed in Table 2.1. As shown in Figure 2.17,

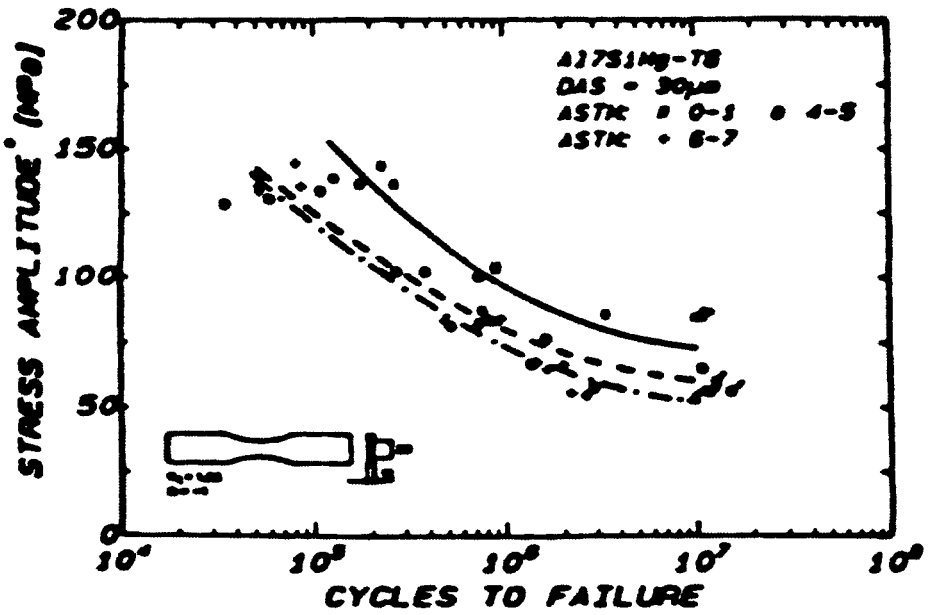


**Figure 2.17** Influence of porosity on fatigue strength of Al7SiMg-T6 casting alloy.[46]

the pores have a negative effect on the fatigue strength in that as the porosity volume fraction in the specimen increases, the fatigue life decreases. Using scanning electron microscopy to examine the fatigue fracture surface, they found that the fatigue crack is often nucleated at pores.

**Table 2.1** Porosity data for the fatigue-tested specimens of Figure 2.17 [46]

| Approx. $H_2$ content (ppm) | ASTM rating | Volume% porosity |
|---|---|---|
| 0.2-0.3 | 0-1 | 0.5 |
| 0.4 | 4-5 | 3.0 |
| 0.5 | 6-7 | 4.3 |

Donlon *et al.*[47] studied the effect of porosity on fatigue properties of low pressure permanent mold cast 356-T6 aluminum wheels. They found that fatigue life curves exhibited a large amount of scatter due to the effect of casting defects, mostly shrinkage

and gas porosity. They verified the concept that fatigue testing is a better indicator of casting quality than either X-ray inspection or metallographic examination.

Inguanti[48] studied the effect of porosity on the fatigue properties of A201.0 and A357-T6 cast alloys. He found that any foundry or post-foundry process which reduces shrinkage porosity in A201.0 alloy will substantially increase its fatigue strength, and that A357-T6 alloy castings free of large shrinkage voids exhibit the optimum combination of tensile and fatigue properties.

Stanzl-Tschegg *et al.*[49] studied the effect of microporosity on fatigue crack initiation and propagation in AlSi7Mg cast alloy at very high ($10^8$-$10^9$) numbers of cycles. They concluded that crack initiation sites are casting voids, which lead to stress concentrations. Using two (almost identical) alloys with different microporosity levels, they showed that a reduction of the number of voids increases the number of cycles necessary for crack initiation. Also, there is no obvious correlation of static and fatigue properties of both alloys: microporosity mainly governs fatigue crack initiation but has no significant influence on the static strength.

Sonsino and Ziese[50] studied the effect of porosity on the constant and variable amplitude fatigue of age-hardened G-Al-7Si-0.6Mg and non-age-hardened G-Al-11Si-Mg-Sr alloys. They found that the porosity level influences fatigue strength in different ways. If the porosity level is increased from about 0 to 8%, fatigue strength in the un-notched condition is reduced by about 17% for both alloy groups. In the notched condition, the age-hardened alloy displays a 7% drop in fatigue strength, while for the non-age-hardened alloy, the fatigue strength drops by 20% because of the lower yield point in the notched

condition. They found no evidence that the size of the solidified cross-section had any influence on fatigue strength in the porous condition. Thus, they proposed that even in safety parts porosity can be tolerated, however, not in highly-stressed fatigue-critical areas.

Couper *et al.*[51] measured the fatigue properties of un-notched polished specimens of Al-7Si-0.4Mg (Australian designation CP601) aluminum casting alloy for various heat treatment conditions and at various mean stresses. They observed that failure initiated at interdendritic shrinkage defects. Although evidence of classical crack initiation from persistent slip bands was also seen, such cracks, being less severe than the casting defects, never caused failure. They attributed the insensitivity of the fatigue (S-N) behavior to heat treatment to the fact that fatigue crack initiation occurred at casting defects, notably shrinkage porosity. Reducing the size of shrinkage defects would increase the fatigue life, but only up to the stage at which crack initiation from persistent slip bands on the surface became operative.

Suzuki and Kunio[52] carried out rotating fatigue tests on two types of Al-Si-Cu aluminum casting alloys containing pores of different sizes resulting from solution heat treatments at 470°C (L material) and 495°C (H material), respectively. Lowering the temperature of the solution treatment improved the fatigue strength due to the reduction in the pore size. Fractographic analysis using scanning electron microscopy revealed that the origin of fatigue fracture in both materials was a porous defect (casting porosity or blister). The quantitative relation between the fatigue strength and the porous defects was determined as follows: the S-N diagram was replotted in the form of an $S\sqrt{\pi d}$ –N diagram, d being the dimension of the porous defect in the direction of the centre of the specimen

and S the stress amplitude. Figure 2.18 shows the corresponding $S\sqrt{\pi d}$ –N plot. As can be seen, the relation between $S\sqrt{\pi d}$ and N is correlative. It can be comprehended that the scatter in the fatigue strength values with the solution treatment is controlled by the dimensions and distributions of the porosity defects in the tested specimens.

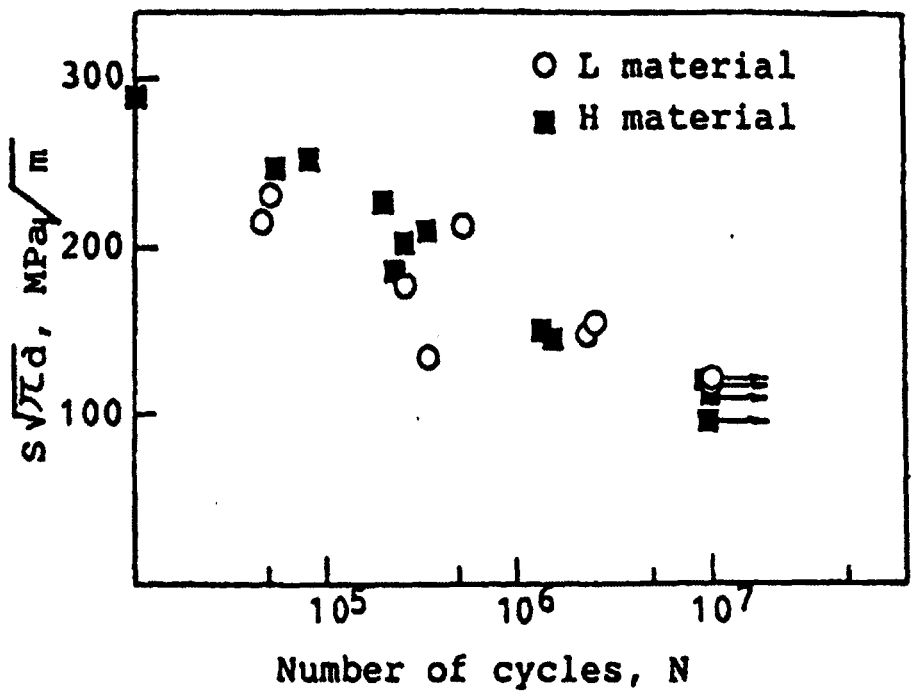


**Figure 2.18** $S\sqrt{\pi d}$ –N diagram.[52]

Ting and Lawrence[53] studied the influence of casting porosity on the fatigue life of as-cast and smooth (polished surface (30 μm)) specimens of AA 319 cast aluminum alloy containing casting porosity. Fatigue initiating sites were observed using a scanning electron microscope. Fatigue cracks were observed to initiate from the near-surface casting pores in the polished specimens and from the as-cast surface texture discontinuities in the as-cast

specimens. Plots of the observed fatigue life against the depth of the fatigue initiating defect for various stresses of smooth specimens are shown in Figure 2.19.

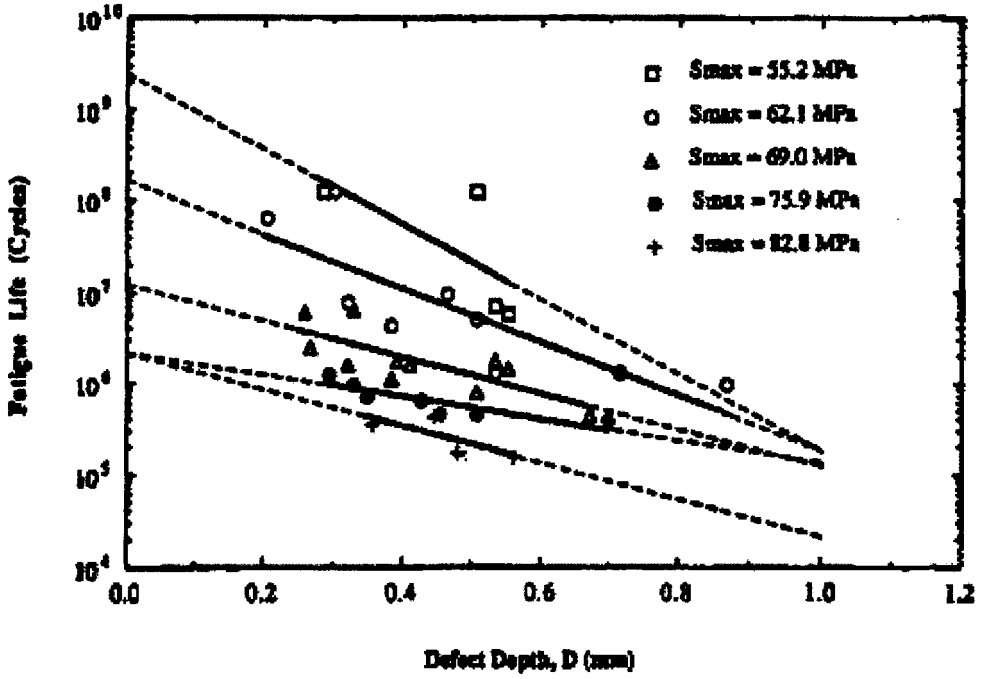


**Figure 2.19** Linear regression analysis of the fatigue life of smooth specimens of AA319 as a function of the depth of the casting pore that caused fatigue failure.[53]

Gundlach *et al.*[54] studied the effects of microstructural variables such as solidification rate, dendrite arm spacing (DAS), level of porosity, eutectic silicon modification and Fe-rich intermetallic phases on the thermal fatigue properties of 319 and 356 alloys. They found that when the increase in porosity content was accompanied by an increase in DAS, thermal fatigue life dropped by 66%, probably as a result of an increase in the size of microporosity voids. Figure 2.20 shows the effect of void (pore) size on the thermal fatigue life of the 319 casting alloy. As expected, thermal fatigue life decreased as the void size increased.

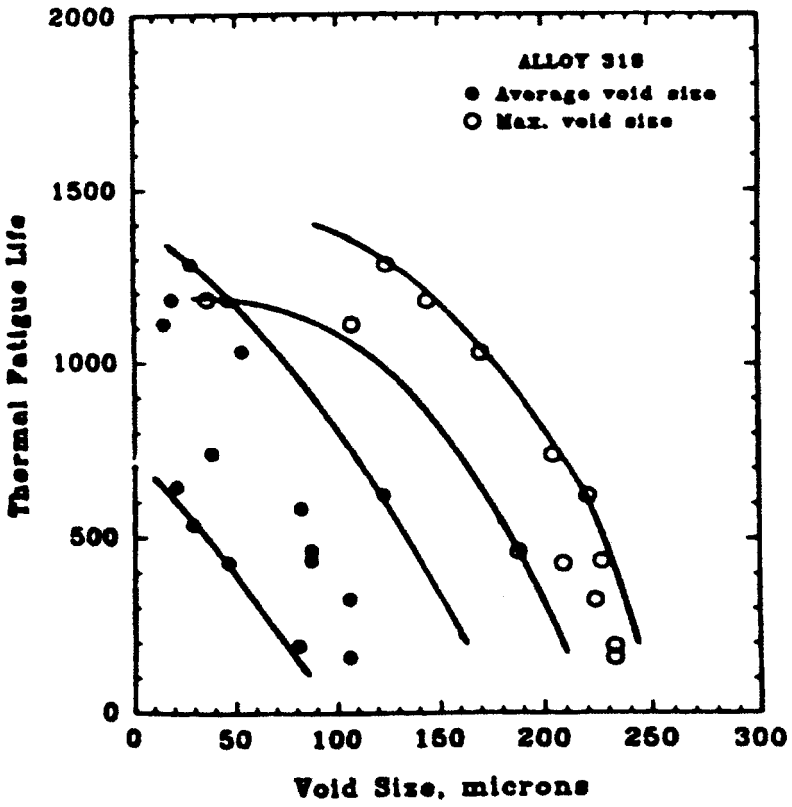


**Figure 2.20** Influence of microporosity void size on thermal fatigue life in alloy 319.[54]

Mayer *et al.*[55] studied the fatigue properties of some magnesium and AlSi9Cu3 aluminum alloys (produced by high-pressure die-casting) in ambient air in the regime of $10^5$ to $10^9$ cycles. They concluded that in 98.5% of the specimens, the fatigue crack initiated at a pore (or porous region). The smallest pore size at the crack initiation location was 0.025 $mm^2$. All investigated alloys showed a pronounced fatigue limit, meaning that while cracks may have initiated at a pore, they did not propagate to failure. They proposed that the critical stress intensity amplitude can be used to correlate the most damaging porosity in a specimen to its critical stress amplitude. If porosity is considered as equivalent to an

initial crack, the fatigue limit can be determined by the critical stress intensity amplitude, $K_{cr}$. The stress amplitude with fracture probability is determined by the critical stress intensity amplitude $K_{cr}$, the probability of porosity to exceed a certain size (defect area) and the probability of crack initiation either at the surface or in the interior.

Buffière *et al.*[56] studied the microstructure and the fatigue properties of three model AS7G03 cast aluminum alloys with different contents of artificial pores, using three-dimensional characterization of porosity by means of synchrotron X-ray tomography. They observed that two types of pores are present in the material: microshrinkage pores and artificial gas pores. The amount of gas introduced in the alloys during processing has almost no influence on the volume fraction of microshrinkage but increases exponentially the volume fraction of gas pores. Most pores are intergranular, their convex parts corresponding to interdenderitic zones containing brittle eutectic silicon particles. With respect to the fatigue properties, the porosity level of the alloys was found to be a first order parameter which greatly altered both the average number of cycles to failure and the lifetime scatter, specially at high stress levels. The initiation of fatigue cracks occurred by decohesion of Si particles located near the convex parts of pores located at or below the surface of the samples.

Avalle *et al.*[57] studied the effect of porosity and other casting defects on the static and fatigue properties of specimens and components of an Al-Si-Cu alloy obtained by high pressure die casting. For the three batches of specimens tested, obtained from castings that had different sprue-runner designs, the observed decrease in fatigue strength for the three batches was related to a combination of the increased porosity level and metallurgical

defects. The authors also proposed that for castings subject to fatigue loading, criteria used for quality control based on a maximum acceptable level of porosity are not appropriate if the average density is not affected and if the cavities are located at the centre of thick sections.

Wang *et al.*[58, 59, 60] carried out different studies on the effect of casting defects on the fatigue performance of cast aluminum alloys. It was observed that casting defects have a detrimental effect on fatigue life by shortening not only the crack propagation period, but also the crack initiation period. Castings with defects exhibited fatigue lives at least an order of magnitude lower compared to that of defect-free ones. The decrease in fatigue life was directly related to the increase in the defect size. For defects of the same size (projected area) oxide films were often less detrimental to fatigue life than pores, this could be attributed to the nature of the microstructures adjacent to porosity and oxide films and also porosity is a 3-D cavity which results in its isotropic adverse influence on fatigue properties, whereas oxide films tend to be 2-D morphology and their adverse effect on fatigue thus depend more on the applied stress direction. Porosity played the most important role in determining fatigue performance of the material. According to Wang *et al.*,[58, 59, 60] there is a critical defect size for fatigue crack initiation, below which the fatigue crack initiates from other competing crack initiators such as eutectic particles and slip bands. Figure 2.21 and Figure 2.22 show the effect of pore size on the fatigue life of Sr-modified A356-T6 alloy specimens obtained at high and low cooling rate, and that of pore size and shape on the fatigue life of Al-Si-Mg alloys obtained from their work.

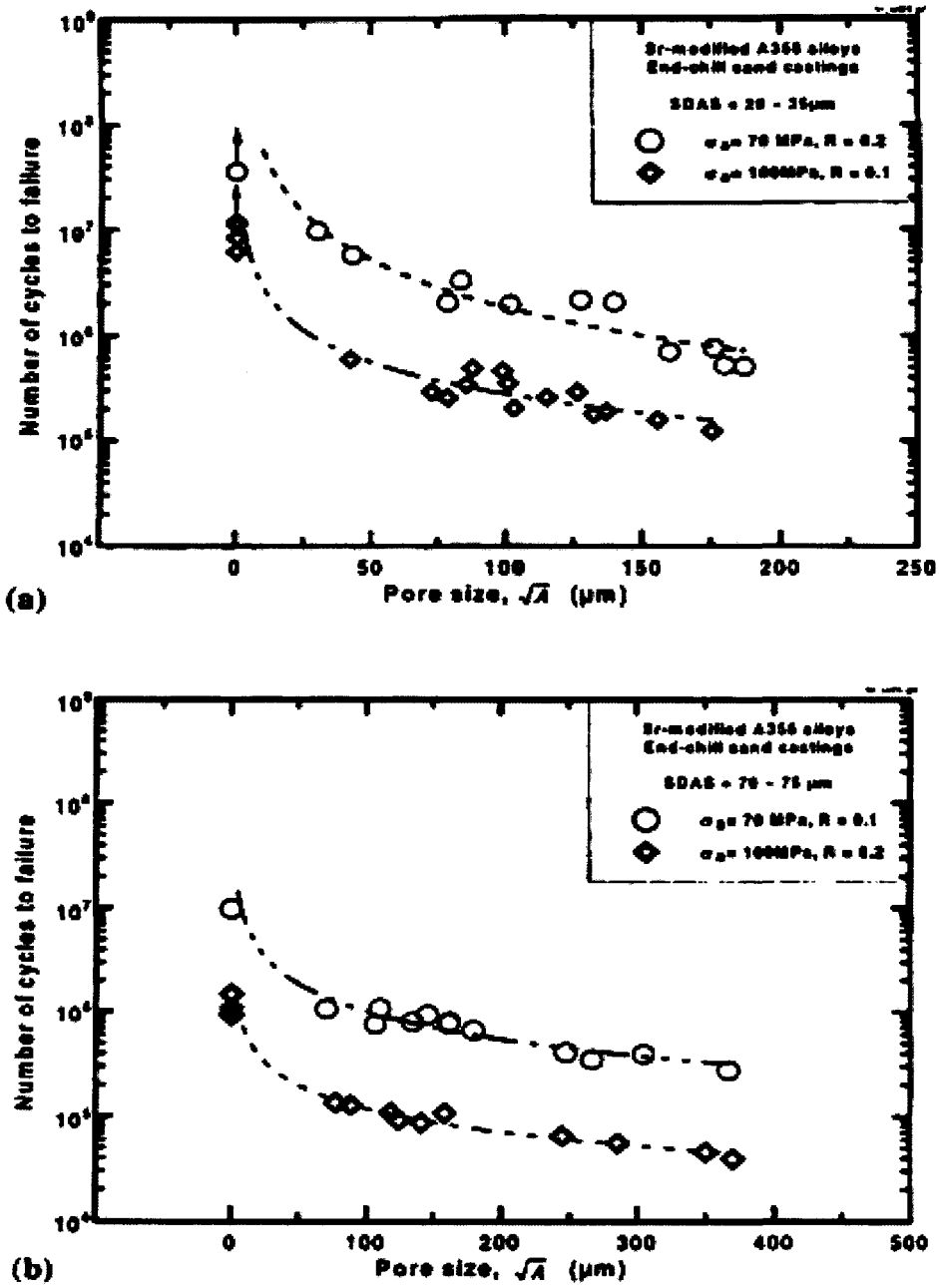


**Figure 2.21** Fatigue life of a Sr-modified A356-T6 alloy as a function of pore size: (a) SDAS: 20-25$\mu$m, (b) SDAS: 70-75$\mu$m.[58]

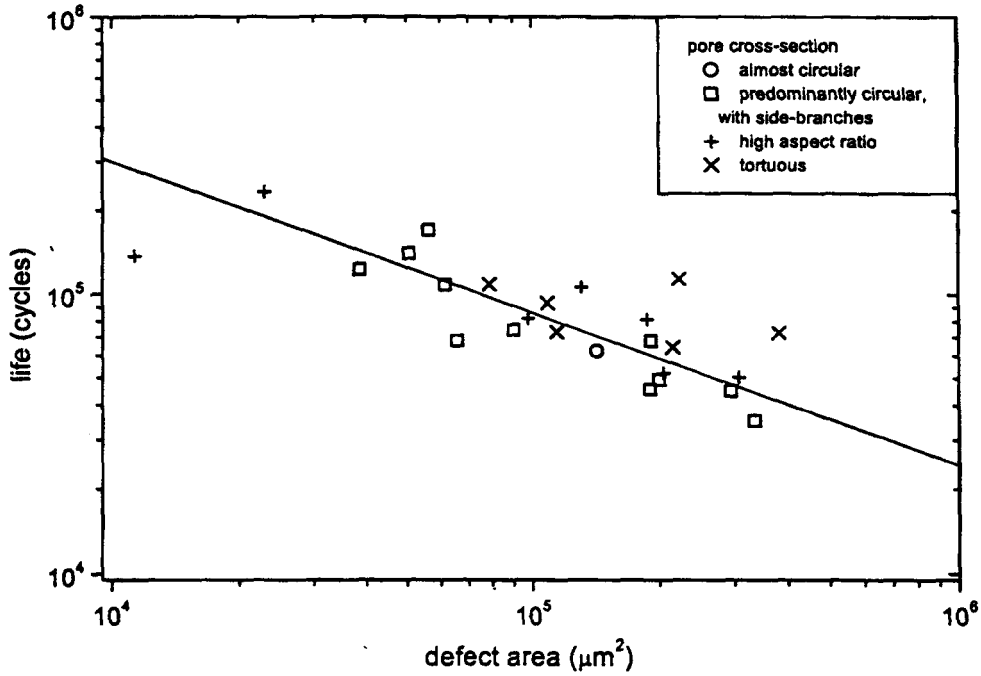


**Figure 2.22** The effect of pore size and shape on fatigue life in an Al-7Si-0.6Mg casting tested at R=0 and 190MPa maximum stress.[59]

Boileau *et al.* [12, 61, 62] carried out different studies on the fatigue properties of cast 319 and A356-T6 aluminum alloys. It was observed that pore size was found to have a statistically significant effect on the fatigue life of T7-treated W319 alloy (this alloy differs in composition from Aluminum Association 319 alloy, and so is referred to as W319). A comparison between porosity-containing, non-hot isostatic pressed (non-HIPped) and pore-free, hot isostatic pressed (HIPped) W319 alloy specimens revealed that the absence of porosity increased the fatigue resistance and fatigue strength, as shown in Figure 2.24, the magnitude of this increase being dependent upon the solidification time.

Porosity was found to dramatically affect the fatigue life of the A356-T6 Al alloy. In the samples containing porosity (non-HIPped), all initiation sites contained large pores

that arose from microshrinkage. Such porosity-containing material showed an approximate ten-fold decrease in the fatigue life compared to as-cast + HIPped material, as shown in Figure 2.25. This trend was observed regardless of the solidification time of the tested samples. In the as-cast + HIPped specimens, the initiation sites contained a large, irregular, flat-shaped feature, believed to be the remnants of microshrinkage pores that were closed and welded during the HIPping process.

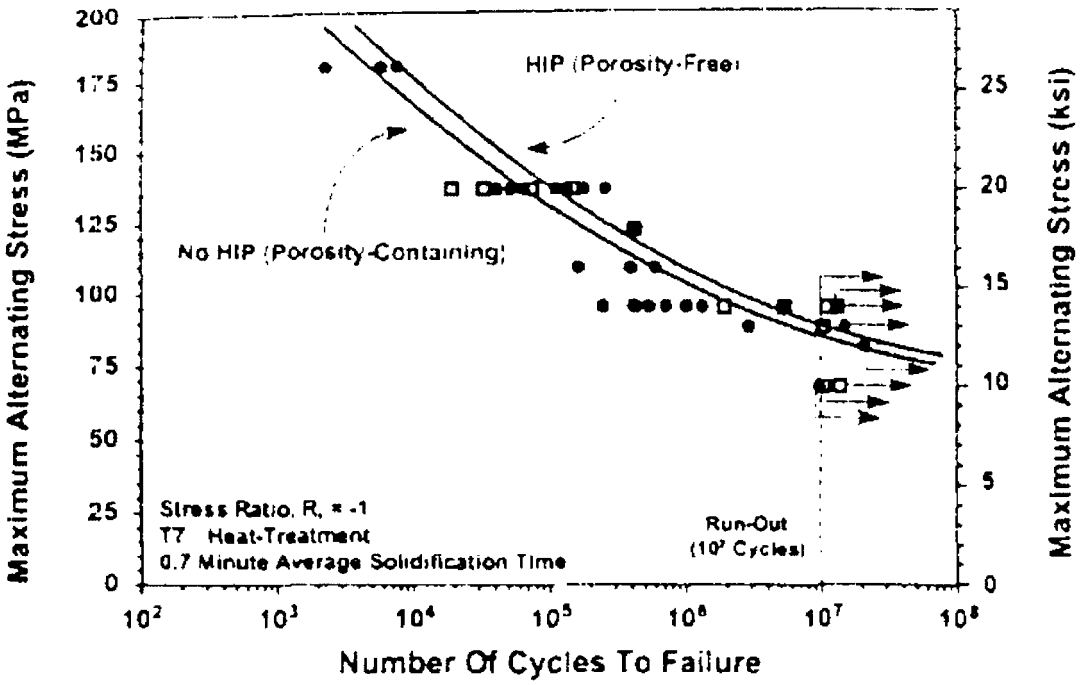


(a)

**Figure 2.23**

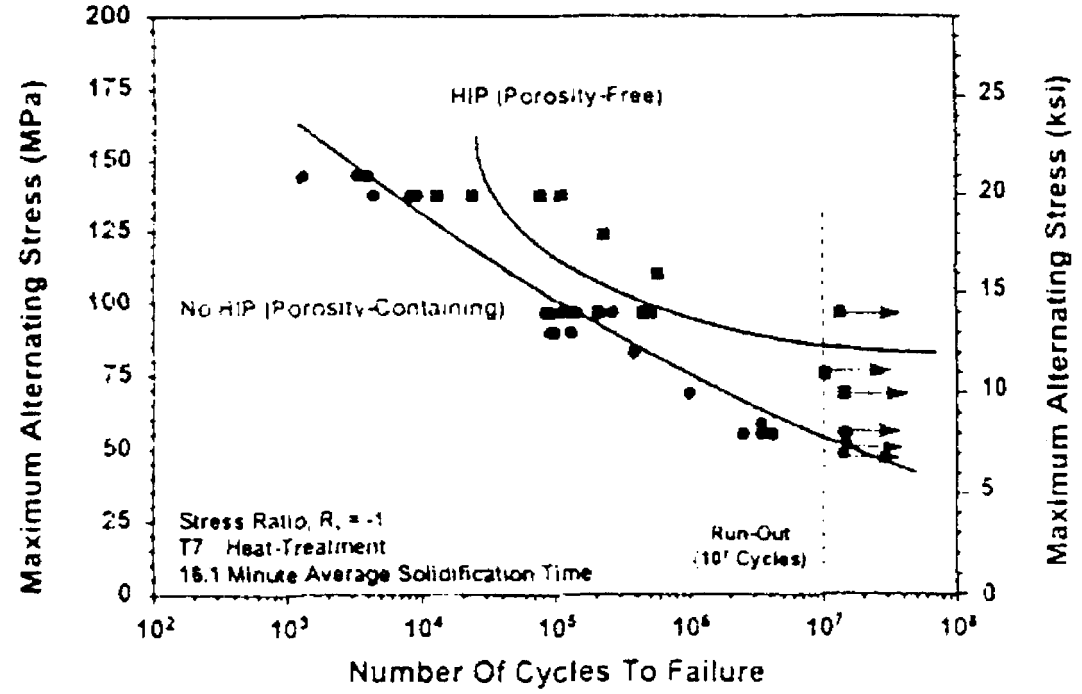


(b)

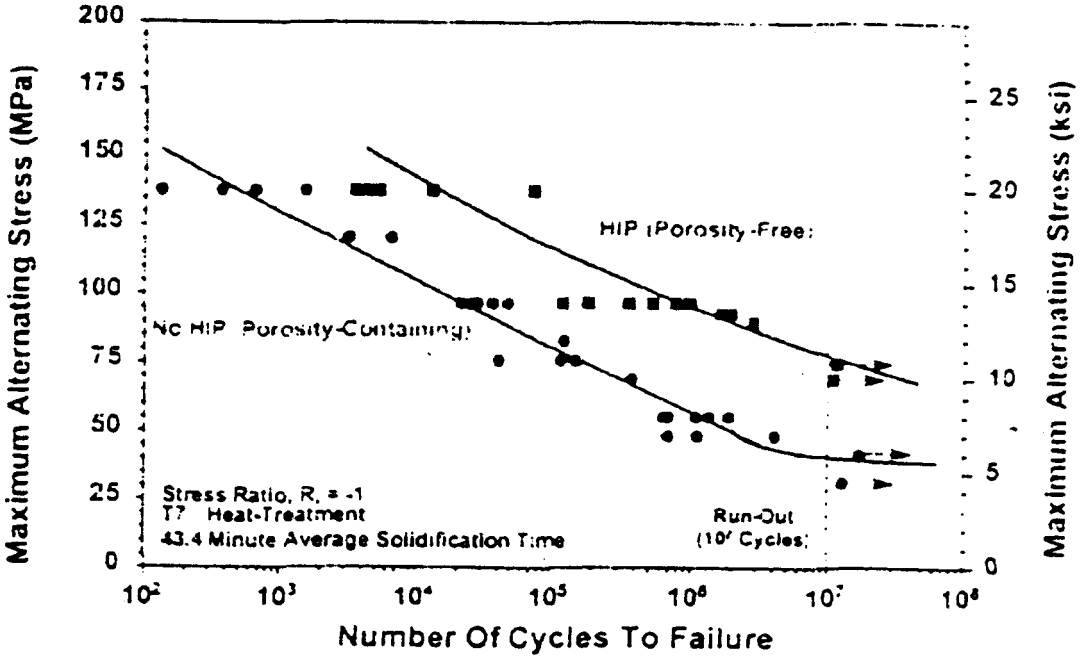


(c)

**Figure 2.24** A comparison of the fatigue properties of W319-T7 Al in the HIPped and non-HIPped conditions: (a) average solidification time of 0.7 min, (b) 16.1 min, and (c) 43.4 min.[61]

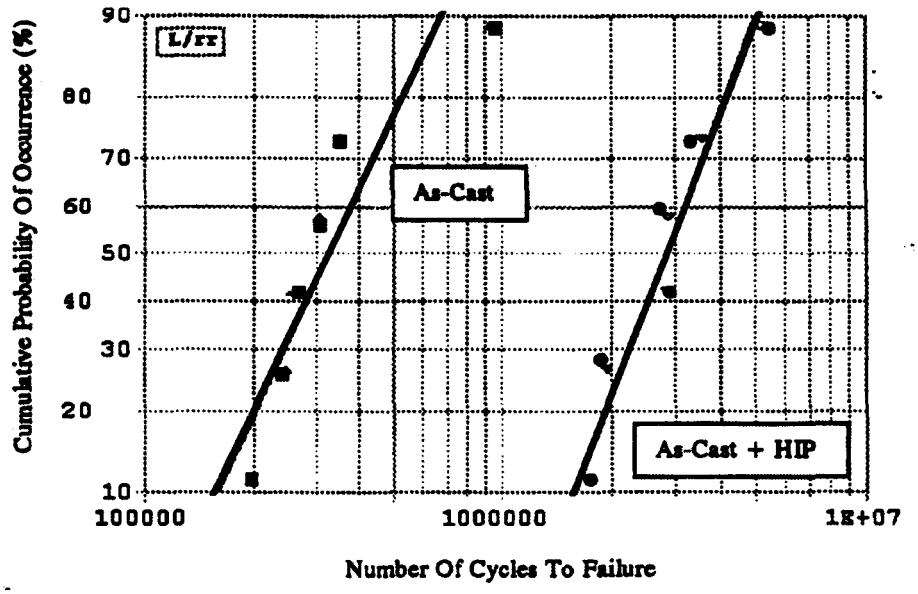


**Figure 2.25** Statistical analysis of the effect of porosity on the fatigue lives of as-cast and as-cast + HIPped A356-T6 aluminum (30 mm SDAS) tested at 138 MPa.[62]

Lee *et al.*[63] studied the effect of HIPping on the high-cycle fatigue properties of investment cast A356 Al alloys. The results indicated that the fatigue strength of HIPped alloys was higher than that of non-HIPped alloys due to the significant reduction in volume fraction of pores by HIPping. In the non-HIPped specimens, fatigue cracks initatited at large pores adjacent to the specimen surface and then propagated down to several hundred micrometers depth while coalescing with other large pores. The HIPped specimens showed 40-50% improvements in fatigue strength over the non-HIPped specimens, and where the fatigue crack initatited mainly at eutectic Si particles and propagated along them. These results are in keeping with those reported by Wang[58] and Boileau[61] on the effect of HIPping in improving the fatigue performance of Al-Si casting alloys.

Odegard and Pedersen[64] studied the fatigue properties of an A356 (AlSi7Mg) alloy by comparing materials free from, and containing, casting defects. It was observed that in an A356 alloy free from casting defects such as shrinkage and pores, persistent slip bands (PSBs) acted as sites for crack initiation. Material containing pores showed approximately 50% reduction in fatigue life compared to the defect-free material, and the fatigue strength at $10^7$ cycles was reduced by 20%. It was also found that cracks initatited from the casting defects and that most of the fatigue life was spent in the fatigue crack growth regime.

Rading *et al.*[65] studied the fatigue crack growth (FCG) characteristics of cast Al-Cu A206 alloy samples containing different levels of porosity. It was observed that the fatigue crack growth rate increased with increasing levels of porosity, particularly close to the threshold level. This enhancement in FCG rate is attributed to the size and morphology of the interdendritic pores, which lead to initiation of secondary cracks ahead of the main crack as well as intermittent jumps in the crack length. Hot isostatic pressing is effective in reducing the porosity level. However, its effect on FCG rate is limited to the near-threshold regime.

Major[66] studied the effect of porosity on the fatigue behavior in A356-T61 aluminum alloy and found that the parameters that directly affect fatigue life are the largest pore size, DAS, and the stress amplitude. Once these parameters are taken into account, indirect parameters-which are important in determining the largest pore size - lose their significance. The parameter that had the largest impact on the fatigue life was the largest pore size. The impact of DAS on the fatigue life was weaker than that of the largest pore size and tended to decrease with decreasing stress amplitude.

Savelli *et al.*[67] studied two AlSiMg0.3 alloys with different porosity contents with regard to fatigue properties. It was observed that quantitative parameters characterizing size or shape of internal pores could be measured on three dimensional reconstructed images and correlated to the fatigue properties. For the two alloys investigated, the fatigue properties appeared to be dependent on the size rather than the shape of the pores.

Skallerud *et al.*[68] studied the effect of casting defects on the fatigue life of AlSi7Mg(0.4) alloy. It was observed that shrinkage cavities (interdendritic pores) in components cast from the alloy have a significant effect on the lifetime. With pores present, the initiation period of the total lifetime was very short, and almost negligible, and a typical fatigue crack initiated around pores at or near the specimen surface, due to the high stress concentration associated with the shrinkage pores.

Zhang *et al.*[69] investigated the influence of SDAS and porosity on high cycle fatigue (HCF) crack initiation and propagation in A356.2-T6 alloy. The HCF cracks initiate at porosity, oxides, or eutectic constituents, depending on the SDAS. When the SDAS is greater than 25-28 μm, pores with lengths greater than ~100 μm act as the main crack initiation site. For HCF, the effect of SDAS is overshadowed by the effect of porosity. At SDAS below 25-28 μm, the pore size is below the critical value; in this case large eutectic constituents initiate the HCF cracks.

Seniw *et al.*[70] studied the influence of pore morphology and location on the fatigue life of die cast aluminum A356 alloy. They found that in cases when the pore size is small and at a large distance form the free surface, the samples exhibited the longest fatigue life. This is shown in Figure 2.26, which shows the relation between cycles to failure, $N_f$, pore

area, A, and its distance from the surface, d. The curved line in the x-y plane suggests an accept/reject boundary, based on the influence of the pore parameters A and d on the fatigue life.

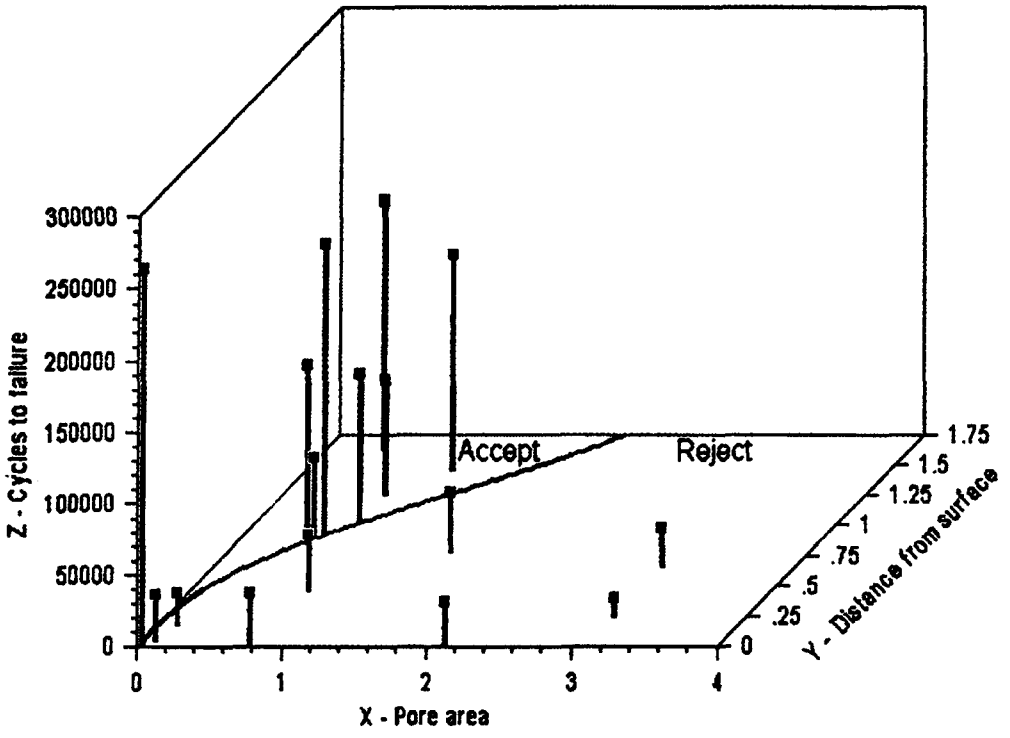


**Figure 2.26** Relation between $N_f$, A, and d. The curved line in the x-y plane suggests an accept/reject boundary for pore size/location in terms of the fatigue life.[70]

From the literature review [46-70] it appears that porosity is the key factor which controls the fatigue properties of Al-Si casting alloys. Pores are preferred crack initiation sites in these alloys, and thus constitute the main effect on fatigue performance, independent of the loading condition and of the applied stress. Compared with porosity, eutectic structure and intermetallic phases play a minor role in crack initiation.

The effect of porosity on fatigue life may be summarized as follows: pores reduce the time for crack initiation by creating a high stress concentration in the material adjacent to the pores. As a result, most of the fatigue life is spent in crack growth. In terms of its importance in crack initiation, a single shrinkage pore close to or at the surface is considered to be the most critical, followed by a series of shrinkage pores at the surface, with a gas pore at the surface being the least critical.

In the present study, the effect of casting imperfections on the fatigue properties of various Al-Si casting alloys was investigated, in terms of the importance of these defects on fatigue crack initiation, with emphasis on the role of porosity on the latter. The effects of casting process, heat treatment conditions, and alloy chemistry were also incorporated. The alloys investigated, namely LP PM319-F, A356-T6, C354-T6, AE425 and PM390, include both hypoeutectic and hypereutectic alloys, of the type employed in automotive applications.

# CHAPTER 3

# EXPERIMENTAL PROCEDURES

# CHAPTER 3

# EXPERIMENTAL PROCEDURES

The five Al-Si alloys studied in the present work were 319, A356, C354, AE425 and 390 alloys. The fatigue specimens were sectioned from real automotive castings prepared from these alloys, and machined according to ASTM E466 specifications. One hundred and fifty seven (157) fatigue-tested samples were received from General Motors Powertrain corresponding to the five alloys. Samples sectioned from the fractured samples were examined using scanning electron and optical microscopy to characterize the casting defects present on the fracture surface, and to subsequently determine the correlation between the fatigue properties and these defects. The experimental procedure, covered in six steps, is described in Sections 3.1 through 3.6 below.

## 3.1 CLASSIFICATION OF SPECIMENS

The castings prepared from the five alloys were obtained from various casting processes and used in the as-cast (F) or, more often, the T6 heat-treated condition. Accordingly, the samples were classified as LP PM319-F, A356-T6, C354-T6, AE425 and PM390 alloy samples, where the 319 alloy castings were obtained using low pressure permanent mold die casting (LP PM), and employed in the as-fabricated (F) condition, i.e., without any heat treatment; the A356 and C354 castings were heat-treated following the T6

regime. In the case of the AE425 and the permanent mold cast PM390 alloy castings, each alloy was fatigue tested at two temperatures: 150 °C and 300 °C. The C354 alloy castings were produced in two groups - with or without the use of hot isostatic pressing (HIP) to provide hipped and non-hipped casting samples. The aim was to study the effect of hipping on the porosity and hence fatigue life in the two cases. The chemical compositions of the five alloys are presented in Table 3.1.

## 3.2 SPECIMEN PREPARATION AND DIMENSIONS

### 3.2.1 Fatigue specimens

The fatigue test specimens were prepared according to ASTM E466 standard specifications, where the specimens have circular cross-sections with tangentially blending fillets between the test section and the ends. According to these standards, the diameter (D) of the test section should preferably be between 0.200 in. (5.08 mm) and 1.000 in. (25.4 mm). The grip cross-sectional area should be at least 1.5 times but is preferably selected to be at least 4 times the test section area for most materials and specimens. The blending fillet radius (R) should be at least 8 times the test section diameter. The test section length (L) should be greater than three times the test section diameter.[71]

In the present work, while the dimensions of the fatigue samples obtained from any one alloy were *identical,* the dimensions of the samples obtained from one alloy varied from those obtained from another alloy (for the five alloys studied), dictated by the type of casting and the selected test locations from which these samples were sectioned. More importantly, the ratios of D, R and L were kept the same to maintain uniform geom-

**Table 3.1** Chemical compositions of the Al-Si alloys studied in the present work

| Alloy Code | Element Concentration (Wt %) | | | | | | | | | | | |
|---|---|---|---|---|---|---|---|---|---|---|---|---|
| | Si | Fe | Cu | Mn | Mg | Na | Ni | Zn | Ti | P | Sr | Al |
| LP PM319-F | 7.500 | 0.4000 | 3.5200 | 0.0190 | 0.3600 | <0.005 | <0.005 | 0.0390 | 0.1300 | <0.005 | 0.0290 | Bal |
| A356-T6 | 7.190 | 0.1200 | 0.0100 | 0.0060 | 0.2700 | <0.005 | <0.005 | 0.0060 | 0.1200 | <0.005 | <0.0050 | Bal |
| C354-T6 | 8.828 | 0.0674 | 1.7072 | 0.0054 | 0.5456 | <<< | <<< | 0.0086 | 0.1933 | <<< | 0.0143 | Bal |
| PM390 | 17.000 | 0.6500 | 4.2300 | 0.2000 | 0.5100 | <0.005 | 0.140 | 0.5100 | 0.0630 | 0.008 | <0.0050 | Bal |
| AE425 | 16.400 | 0.6300 | 2.0900 | 0.7000 | 0.7000 | <0.005 | 0.550 | 0.4300 | 0.0670 | 0.008 | <0.0050 | Bal |

etry, always in keeping with the ASTM E466 norms. A sketch of the specimen used is shown in Figure 3.1. The specimens were sectioned and prepared from different positions in the casting, as shown in Figure 3.2 and Figure 3.3.

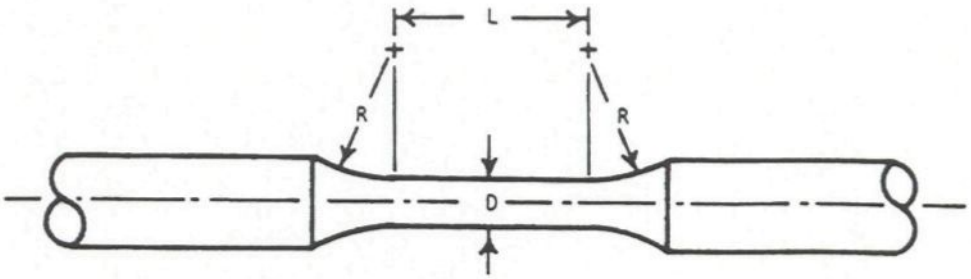


**Figure 3.1** Geometry and dimensions of the ASTM E466 standard specimen used for fatigue testing.[71]

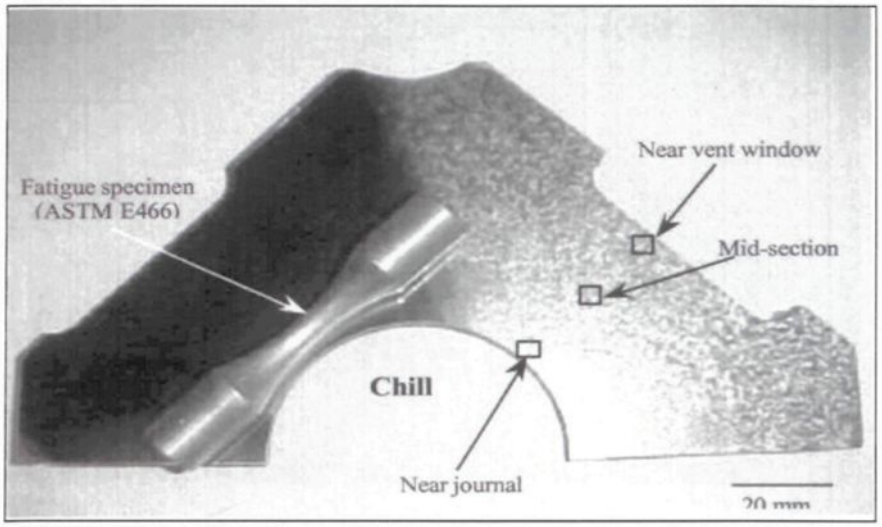


**Figure 3.2** Location of fatigue sample taken from the bulkhead of a "V" engine block.[60]

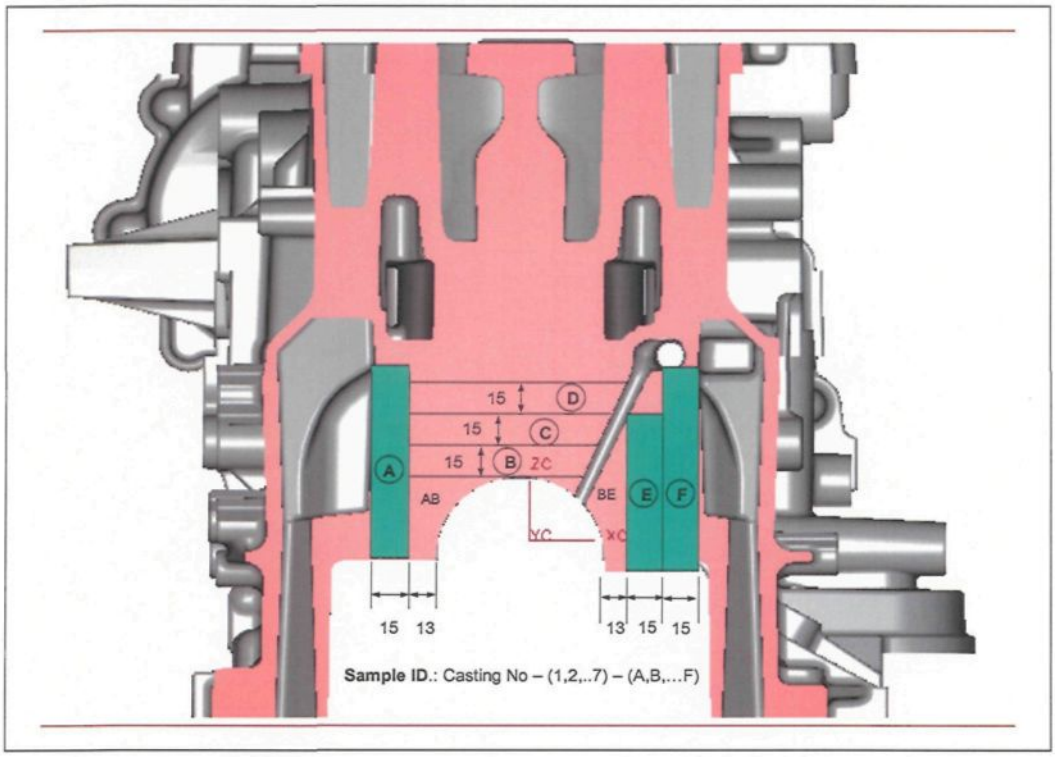


**Figure 3.3** Fatigue samples taken from different positions (A to F) from the real cast.

### 3.2.2 Specimens for SEM examination

Samples for SEM examination were prepared from the fatigue-tested specimens by sectioning them about 1 cm below the fracture surface, and mounting them carefully for fracture surface examination using scanning electron microscopy. Some examples of the samples prepared for SEM examination are shown in Figure 3.4.

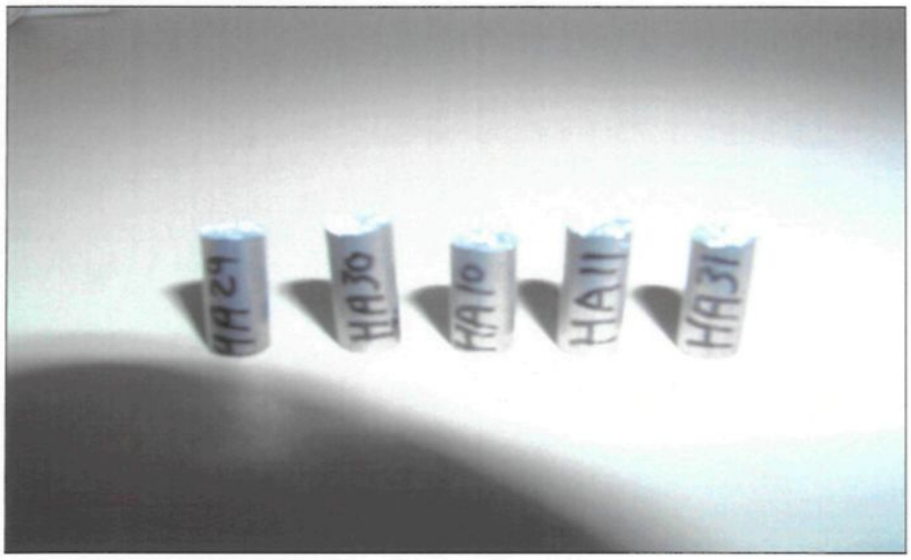


**Figure 3.4** Samples prepared for SEM examination.

## 3.3 METALLOGRAPHY

The microstructural characteristics of the LP PM319 and A356-T6 alloy samples were examined using an optical microscope-image analysis system, where quantitative measurements of the grain size, average secondary dendrite arm spacing, and eutectic silicon particle characteristics were carried out. In each case, the samples were examined in a regular, systematic manner to cover the entire sample surface. The intermetallics present were identified using an electron probe microanalyzer (EPMA) coupled with energy dispersive X-ray (EDX) and wavelength dispersive spectroscopic (WDS) facilities. Figure 3.5 shows the Jeol JXA-8900L WD/ED Combined Microanalyzer (operating at 20 kV and 30 nA) used in the present study.

**Figure 3.5** The electron probe microanalyzer (EPMA) system used in the present study.

## 3.4 TENSILE AND FATIGUE PROPERTIES

The tensile and fatigue tests were carried out at Westmoreland Mechanical Testing and Research, Inc. Youngstown, PA, U.S.A. The tensile properties of the alloys, namely ultimate tensile strength (UTS), yield strength (YS) and percentage elongation (%EL), corresponding to the samples received and the conditions of testing are listed in Table 3.2. The fatigue testing conditions and data obtained for these alloys are provided in Appendix A, in Tables A.1 through A.9.

**Table 3.2** Tensile properties of the alloys studied

| Alloy | UTS, MPa | YS, MPa | % EL |
|---|---|---|---|
| LP PM319-F (25°C) | 223 | 172 | 1.7 |
| A356-T6 (25°C) | 244 | 225 | 0.63 |
| C354-T6 (25°C)-Non-HIPped | 244 | 244 | 0.11 |
| C354-T6 (25°C)-HIPped | 317 | 301 | 0.40 |
| AE425 (150°C) | 191 | 178 | 0.37 |
| AE425 (300°C) | 70 | 57 | 5.42 |
| PM390 (150°C) | 201 | 172 | 0.63 |
| PM390 (300°C) | 72 | 56 | 7.12 |

## 3.5 EXAMINATION OF THE FATIGUE FRACTURE SURFACE

In order to better understand the effect of casting imperfections on the fatigue properties and to create a quantitative database of measurements of the features associated with the fatigue failure, the fracture surfaces of the fatigue specimens were examined using a JEOL 840A scanning electron microscope (SEM) attached with an EDAX Phoenix system for image acquisition and energy dispersive X-ray (EDX) analysis. The voltage selected for this work was 15 kV, with a filament current of 3 amp max. Figure 3.6 shows a photograph of the SEM used.

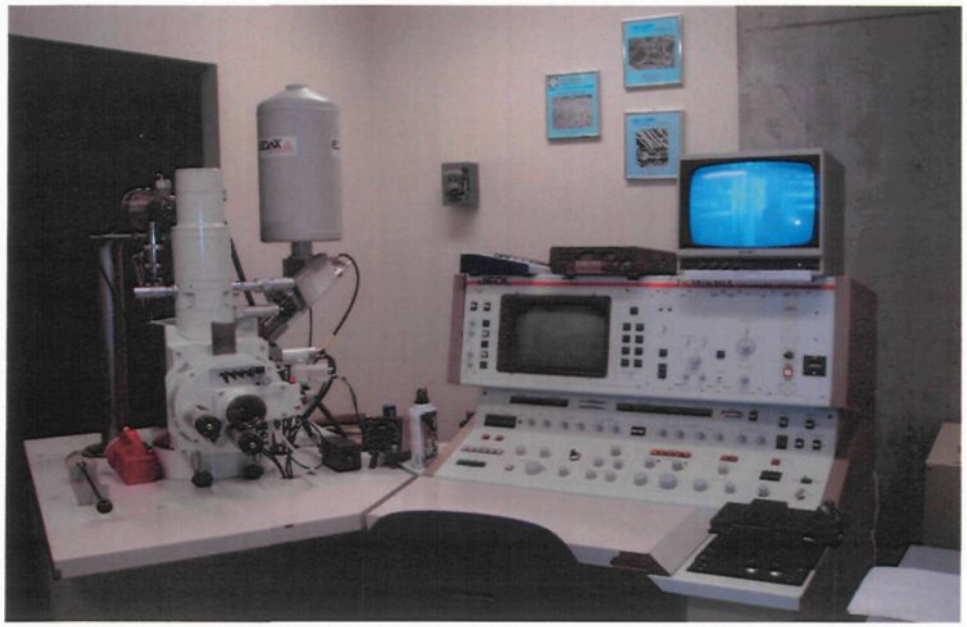

**Figure 3.6** Scanning electron microscope system used in the present work.

## 3.6 CHARACTERIZATION OF CRACK INITIATION SITES

The characteristics of porosity and other crack initiation sites on the fracture surfaces of the fatigue samples were also examined using optical microscopy. For quantification purposes, a Clemex Vision PE4 image analysis system was used, as shown in Figure 3.7. Quantitative measurements of the pore or porous region containing multi-pores were carried out for which the pore areas were measured. For this, the SEM images of the fatigue fracture surfaces obtained were transferred to the image analysis system to carry out the measurements. The magnifications used when obtaining the SEM images ranged from 25X to 350X, depending on the surface pore size and with the aim of obtaining the clearest image of the surface pore(s) responsible for the fatigue crack initiation.

The SEM image transferred to the image monitor screen of the Clemex system was first calibrated to obtain the correct magnification with respect to the image analysis system. Porosity measurements were carried out by outlining the surface pore region, then using a program designed to calculate the pore area automatically.

In the case when oxide films or slip bands were identified as being responsible for the fatigue crack initiation, no quantitative measurements were carried out.


**Figure 3.7** Clemex Vision PE4 image analysis system used in the present work.

# CHAPTER 4

# RESULTS AND DISCUSSION

# CHAPTER 4

# RESULTS AND DISCUSSION

## 4.1 INTRODUCTION

The fatigue properties of an Al-Si alloy casting are controlled by a number of factors including the alloy microstructural features (size and morphology of the eutectic Si particles, secondary dendrite arm spacing, intermetallics, slip bands, and grain size) and casting defects (porosity and oxides) present in the casting. Surface porosity plays an important role in determining the fatigue life as, with the increase in the surface porosity/pore size, the fatigue life decreases, and *vice versa*.

Qualitative and quantitative analysis of porosity was carried out on the fracture surface of 157 fatigue-tested samples obtained from LP PM319-F, A356-T6, C354-T6, AE425 and PM390 Al-Si alloys using scanning electron microscopy and image analysis. The SEM fractographs were analyzed using image analysis to obtain a comprehensive understanding of the defects (pores) responsible for the fatigue crack initiation observed on the fracture surface. The results are reported separately for the hypoeutectic and hypereutectic alloys.

With respect to the hypoeutectic alloys, the fracture surface of 94 fatigue-tested samples of LP PM319-F, A356-T6 and C354-T6 alloys were examined in order to correlate the defect that initiated the fatigue crack with the sample fatigue life. The results for each alloy are presented separately. A comparison of the fatigue behavior of the 319 and A356 alloys has been made, while in the case of the C354 alloy, the effect of HIPping on the fatigue life is presented, through a comparison of the fatigue behavior of HIPped and non-HIPped samples.

The two hypereutectic alloys studied, namely AE425 and PM390, are Al-Si-Cu-Mg alloys that are used in a wide range of automotive applications. The high Si content of these alloys (between 14 and 20%) results in the formation of a large volume fraction of hard, polygonal primary silicon particles in the microstructure, giving them their high strength and hardness and a high degree of wear resistance at medium or elevated temperatures. On the other hand, low ductility and toughness and an unfavourable shrinkage behavior are the disadvantages that result from the presence of such massive primary silicon particles. [9, 10, 72, 73]

As will be observed, the data presented in some of the sections that follow are limited due to the number of fatigue-tested samples received for the corresponding alloy in question. Also, as mentioned previously in Chapter 3, the fatigue test data are listed separately in Appendix A at the end.

## 4.2 METALLOGRAPHIC ANALYSIS OF LP PM319-F AND A356-T6 ALLOYS

The microstructural features examined included the grain size, the secondary dendrite arm spacing, and the eutectic silicon particle characteristics (area, length, and aspect ratio). Intermetallic phases observed were also identified, using electron probe microanalysis (EPMA) and wavelength dispersion spectroscopy (WDS). Representative examples are provided in this section.

Table 4.1 lists the average grain size, SDAS and eutectic Si particle characteristics typically observed in the samples obtained from the LP PM 319-F and A356-T6 alloys. The SDAS measurements were made over 25 fields for the 319 alloy, and over 14 fields for the A356 alloy, each at 5X magnification. The eutectic Si particle measurements were carried out over 50 fields for the 319 and A356 alloys, at 50X and 20X magnifications, respectively, to obtain a correct and reliable assessment of the range of particle sizes observed in the microstructure. The 319 alloy being Sr-modified (0.029 wt% Sr), and the A356 alloy being slightly modified (<0.005 wt% Sr), resulted in fine well-modified eutectic Si particles in the former case and coarse acicular Si particles in the latter.

**Table 4.1** Average grain size, SDAS, and eutectic Si particle characteristics measured for LP PM319-F and A356-T6 alloys

| Alloy | SDAS (μm) | | Eutectic Si Particle Characteristics | | | Grain Size (μm) |
|---|---|---|---|---|---|---|
| | | | Area ($\mu m^2$) | Length (μm) | Aspect Ratio (%) | |
| LP PM319-F | Av. | 21 | 3 | 2.5 | 2 | 343 |
| | S.D. | 6.45 | 6.41 | 2.66 | 0.94 | 83 |
| A356-T6 | Av. | 63 | 51 | 14 | 3 | 1182 |
| | S.D. | 15.29 | 74.5 | 13.5 | 1.6 | 316 |

As the optical micrographs of Figure 4.1 and Figure 4.2 show, the LP PM319-F alloy exhibits a much more refined structure both in terms of the $\alpha$-Al dendrite size and the eutectic Si particle characteristics. Similarly, the macrographs of Figure 4.3 bring out the significant difference in the grain sizes observed in the two cases (*cf.* 343μm with 1182 μm). The samples shown in the figure were etched using a solution composed of 66% HCl, 33% $HNO_3$ and 1% HF to reveal the grains. The high cooling rate associated with the low pressure permanent mold die casting technique used for the 319 alloy, and the relatively slower cooling rate obtained with the lost foam casting technique used for the A356 alloy would explain the values obtained in the two cases.

Intermetallic phases present in the two alloys were identified using EPMA and WDS analysis, employing a Jeol JXA-8900L WD/ED Combined Microanalyzer, operating at 20 kV and 30 nA, with an electron beam size of ~ 2μm. In the 319 alloy the $\alpha$-Fe $Al_{12}(MnCuFe)_3Si_2$ phase, the Mg-containing $Al_8Mg_8Cu_2Si_6$ phase, and the $Al_2Cu$ phase were identified, while in 356 alloy only the $\beta$-Fe $Al_5FeSi$ phase and $Mg_2Si$ were observed, as shown in Figure 4.4 and Figure 4.5, respectively.

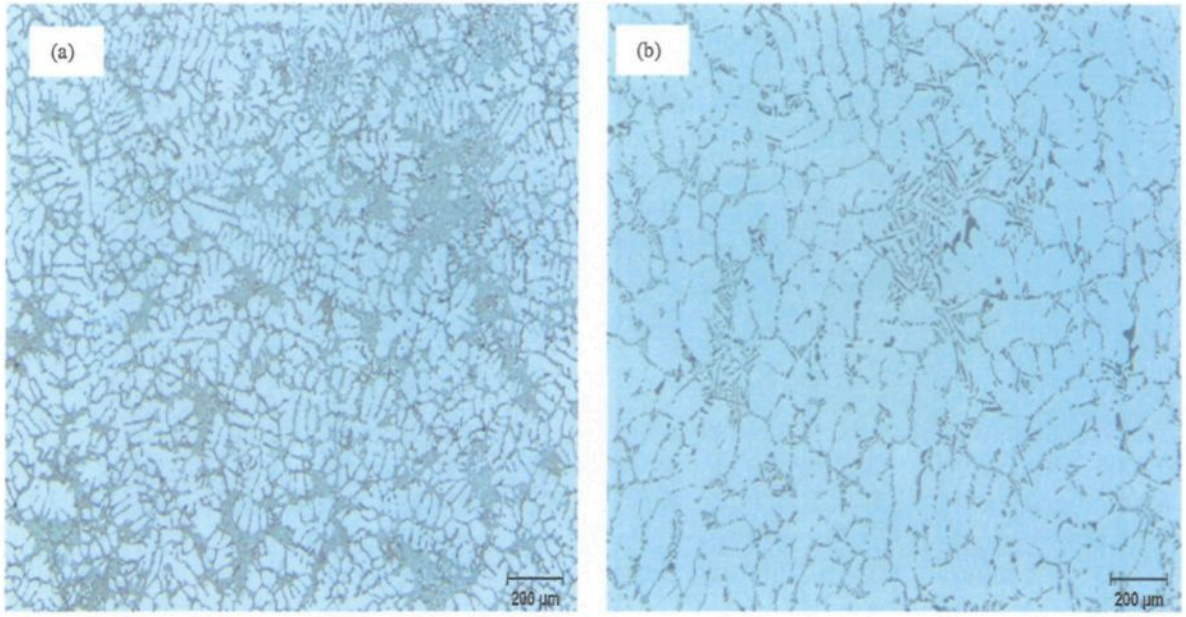


**Figure 4.1** Optical micrographs showing the size of the $\alpha$-Al dendrites in: (a) LP PM319-F, (b) A356-T6 alloys.

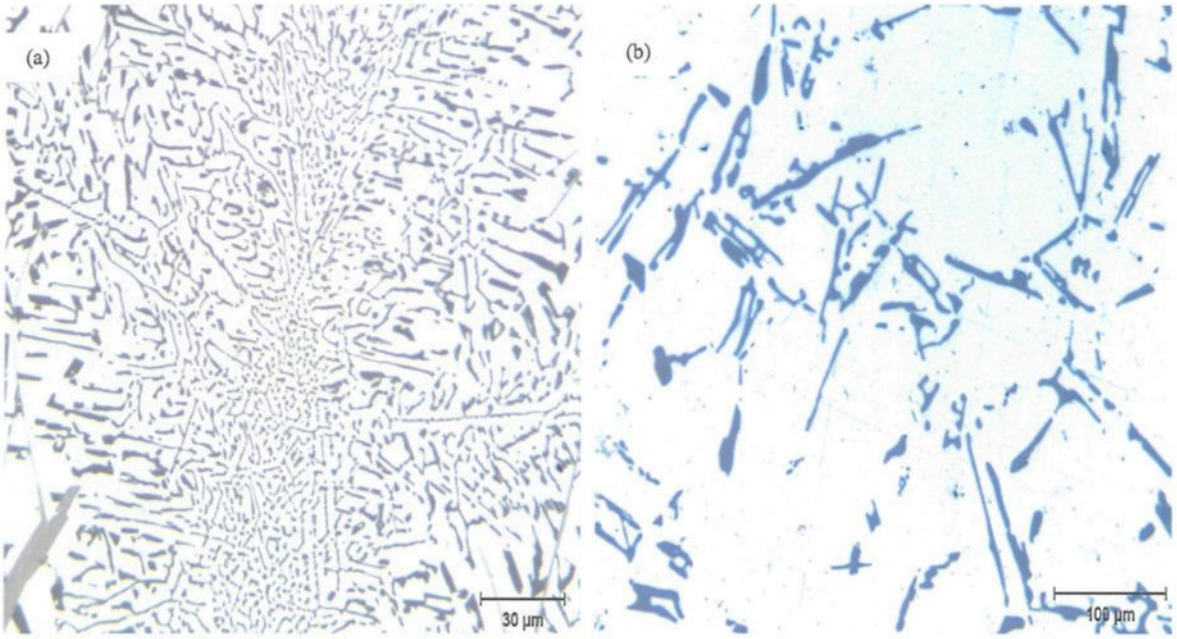


**Figure 4.2** Optical micrographs showing the size and morphology of eutectic silicon particles in: (a) LP PM319-F, (b) A356-T6 alloys.

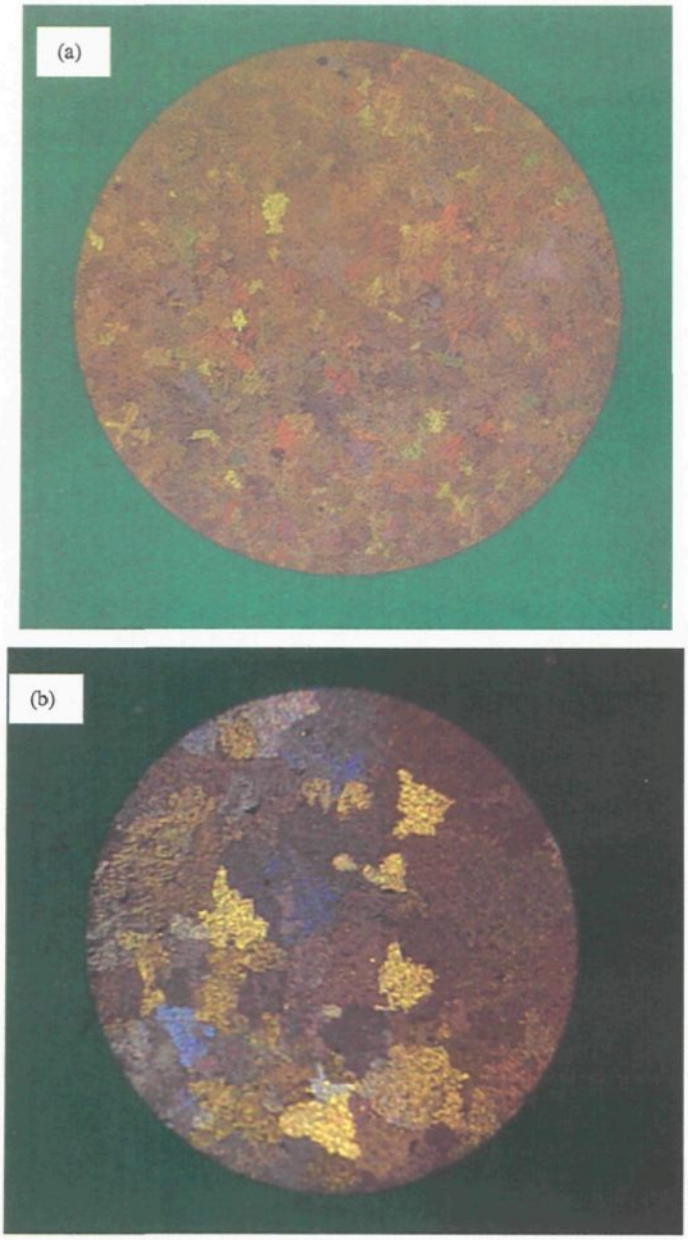


**Figure 4.3** Macrographs comparing the grain sizes in etched samples of (a) LP PM319-F and (b) A356-T6 alloys.

The intermetallic phases observed in 319 alloy influence the matrix stiffness, where the formation of the $\alpha$-Fe intermetallic in the form of Chinese script inside the $\alpha$-Al dendrites increases the matrix strength and improves the material resistance to crack propagation. In addition, the Mg and Cu phases - considered as hardening phases - also improve the matrix strength. The chemical compositions of the $\alpha$-Fe intermetallic phase and the Mg-Cu phase observed in the 319 alloy are shown below in Table 4.2.

**Table 4.2** Chemical compositions of investigated $\alpha$-Fe intermetallic phase and Mg-Cu phase observed in 319 alloy

| Phase # | Element | Wt % | At % | Calculated formula | Shape & colour | Suggested formula |
|---|---|---|---|---|---|---|
| 1 | Al | 57.77 | 69.961 | | | |
| | Si | 10.44 | 12.141 | | Chines | |
| | Fe | 13.54 | 7.919 | $Al_{12}(MnCuFe)_3Si_2$ | script- | $Al_{12}(MnFe)_3Si_2$ |
| | Cu | 1.79 | 0.919 | | grey | |
| | Mn | 13.60 | 8.089 | | | |
| | Total | 97.14 | 99.029 | | | |
| 2 | Al | 32.075 | 29.667 | | | |
| | Si | 25.635 | 23.386 | $Al_8Mg_8Cu_2Si_6$ | Particles | $Al_5Mg_8Cu_2Si_6$ |
| | Mg | 27.595 | 29.179 | | - grey | + Al |
| | Cu | 18.335 | 7.380 | | | |
| | Total | 103.64 | 89.612 | | | |

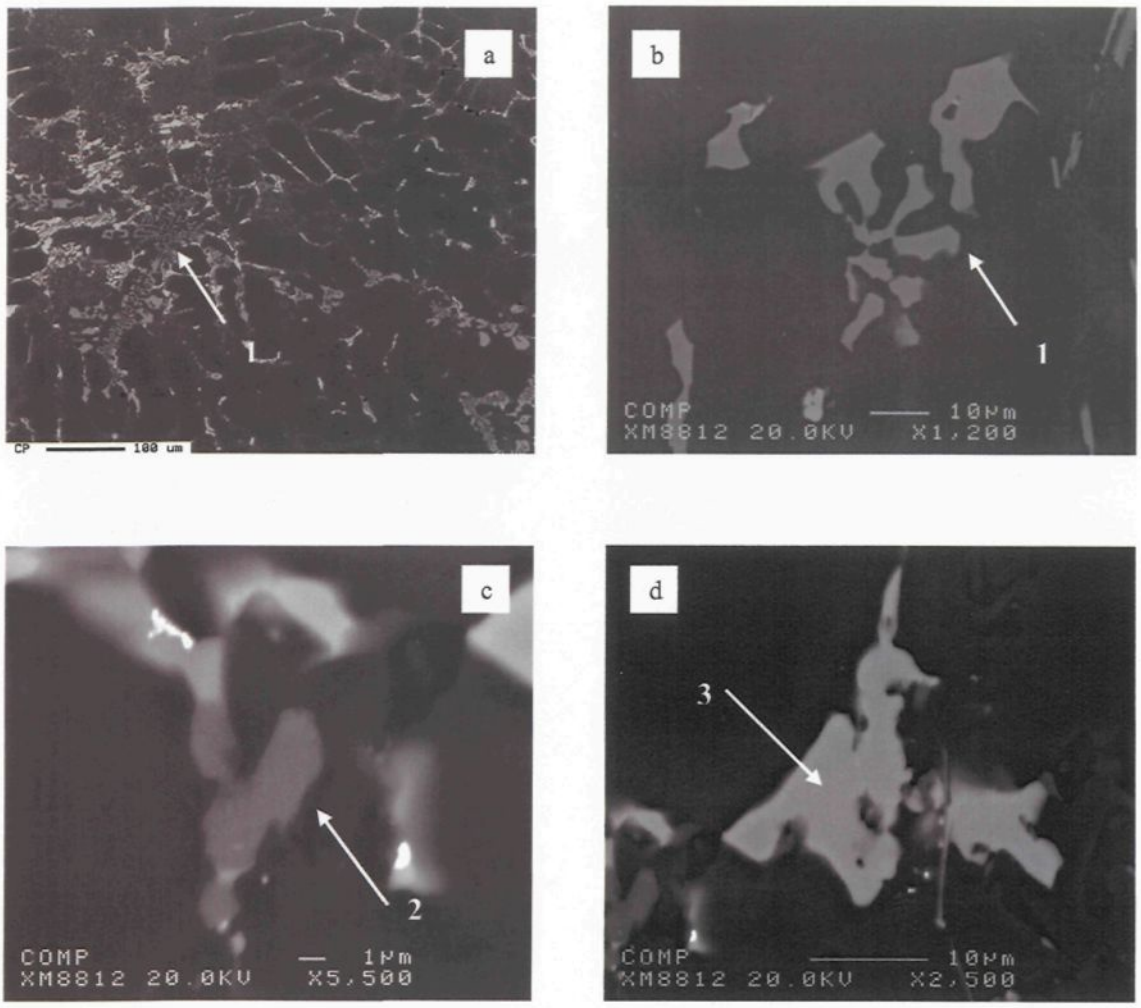


**Figure 4.4** Backscattered images obtained from LP PM319-F alloy. The various phases marked 1 to 3 in (a), (b), (c) and (d) are 1-$Al_{12}(MnCuFe)_3Si_2$; 2-$Al_8Mg_8Cu_2Si_6$; 3-$Al_2Cu$.

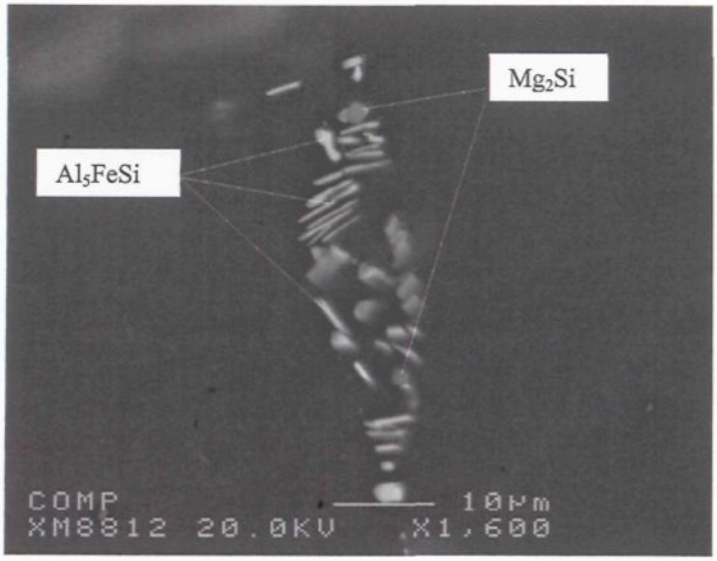


**Figure 4.5** Backscattered images obtained from A356-T6 alloy showing the $Al_5FeSi$ and $Mg_2Si$ phases.

The processing variables such as eutectic modification, solidification rate, heat treatment as well as composition have a profound influence on the resultant cast structure. In turn, these processing and compositional variables significantly influence the fatigue properties.[74] The metallographic characterization of both alloys showed that the LP PM319-F alloy has a much more refined structure compared to that exhibited by A356-T6 alloy, as well as a larger amount of the strengthening phases, which must be taken into consideration when studying the fatigue behavior of the two alloys.

## 4.3 FRACTOGRAPHY OF LP PM319-F AND A356-T6 ALLOYS

The fatigue fracture surfaces of 63 hypoeutectic alloy specimens (LP PM319-F and A356-T6) were examined using scanning electron microscopy (SEM) to identify the fatigue crack initiation sites. Following this, quantitative measurements of these crack initiation

sites were carried out using an image analyzer. To identify the fatigue crack initiation site we had to take into consideration that the fatigue fracture surface generally consisted of three main regions:[12] (i) fatigue crack initiation, (ii) fatigue crack growth, and (iii) fast fracture regions.

To identify the exact crack initiation site using scanning electron microscopy, the initiation sites were located in regions that contained "beach marks" (macroscopic arc-shaped features that are concentric with and move away from the initiation site) and/or "river lines" (macroscopic linear features that radiate away from the initiation site), as indicated in section 2.6.3. The following results were obtained.

### 4.3.1 LP PM319-F alloy

The fatigue fracture surfaces of 23 specimens of LP PM319-F alloy were examined to show the effect of casting defects on the fatigue life. It was found that, in 22 of the 23 samples (i.e. in 96% of all samples examined), the fracture occurred due to the presence of a pore at the surface which acted as the main crack initiation site. Figure 4.6 shows examples of the SEM images obtained from the fatigue fracture surface of an LP PM319-F alloy sample. The arrow in Figure 4.6(a) points to the pore which initiated the fatigue crack.

Quantitative measurements of the surface pores which initiated the fatigue crack were carried out using the image analysis system and the results of the effect of surface pore size, perimeter, length, and width on the fatigue life of LP PM319-F alloy are shown in Figure 4.7 and Figure 4.8. The fatigue tests were carried out at room temperature (25°C),

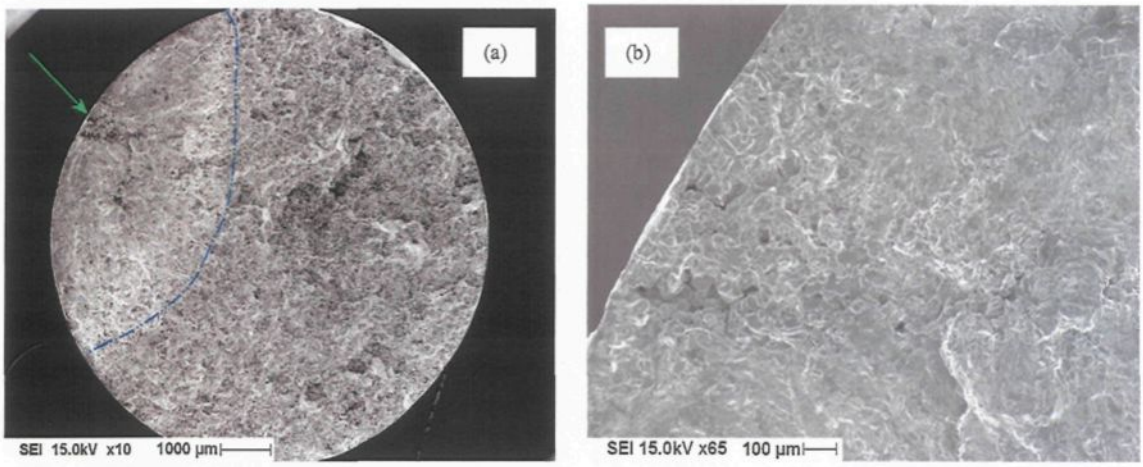


**Figure 4.6** SEM images of the fatigue fracture surface of an LP PM319-F alloy specimen, taken at (a) low magnification, showing the bright area and the crack initiation site, (b) high magnification, showing the surface porosity associated with the crack initiation site.

using a stress ratio R = -1, a sinusoidal waveform, and under high cycle fatigue conditions (i.e., the number of cycles to failure were greater than $10^4$ cycles). The stress applied ranged from 76 MPa to 83 MPa. The values for all stress levels are plotted together in Figure 4.7(a) through Figure 4.7(d) and show the effect of surface pore dimensions (area, perimeter, length and width) on the fatigue life, and separately in Figure 4.8 for the different stress levels, showing the effect of surface pore size (area) on the fatigue life at each stress level.

The effect of surface porosity on the fatigue life is obvious: as the surface pore dimensions increase (i.e. surface pore area, perimeter, length, and width), there is a marked decrease in the fatigue life. This decrease in fatigue life is related to the high stress concentration at these surface pores which leads to the setting up of a stress gradient between the sample free surface (extremity) where the pore is located, and the centre of the specimen (sample interior). This stress gradient acts as the driving force for crack propaga-

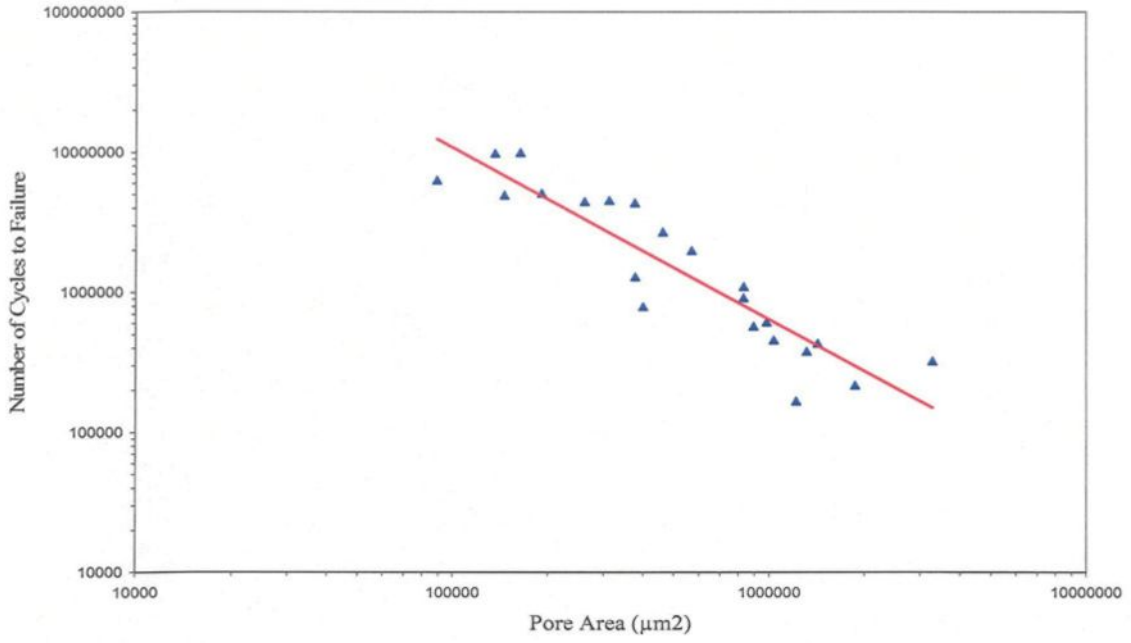
100000000
10000000
1000000
100000
10000
Number of Cycles to Failure
10000
100000
1000000
10000000
Pore Area (μm2)

(a)

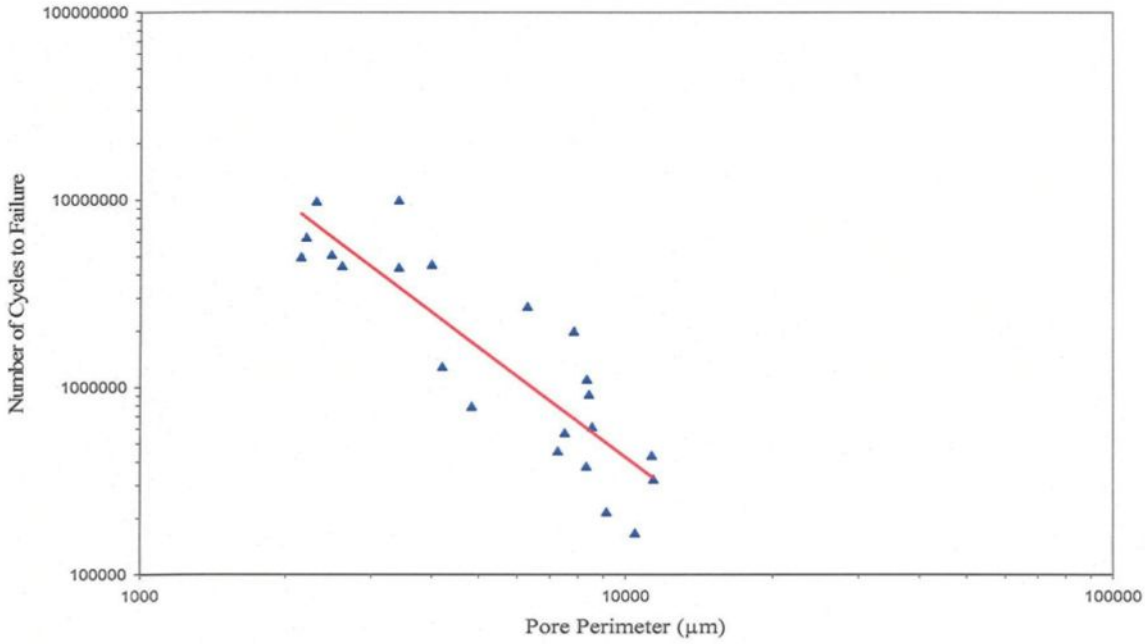
100000000
10000000
1000000
100000
Number of Cycles to Failure
1000
10000
100000
Pore Perimeter (μm)

(b)

**Figure 4.7**

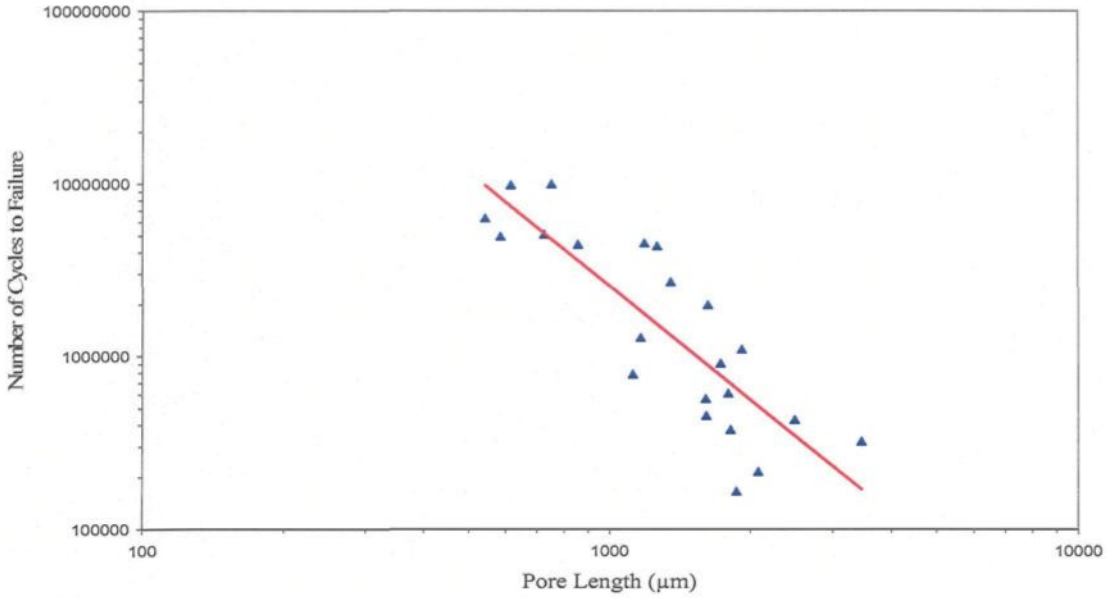


(c)

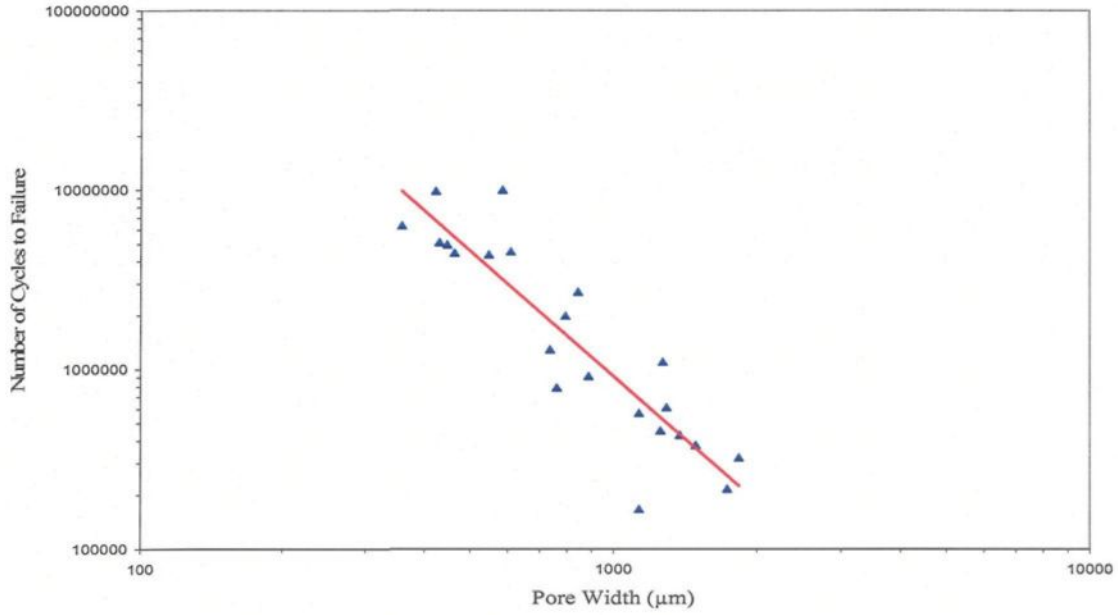


(d)

**Figure 4.7** Effect of surface pore (a) area, (b) perimeter, (c) length, and (d) width on the fatigue life of LP PM319-F alloy.

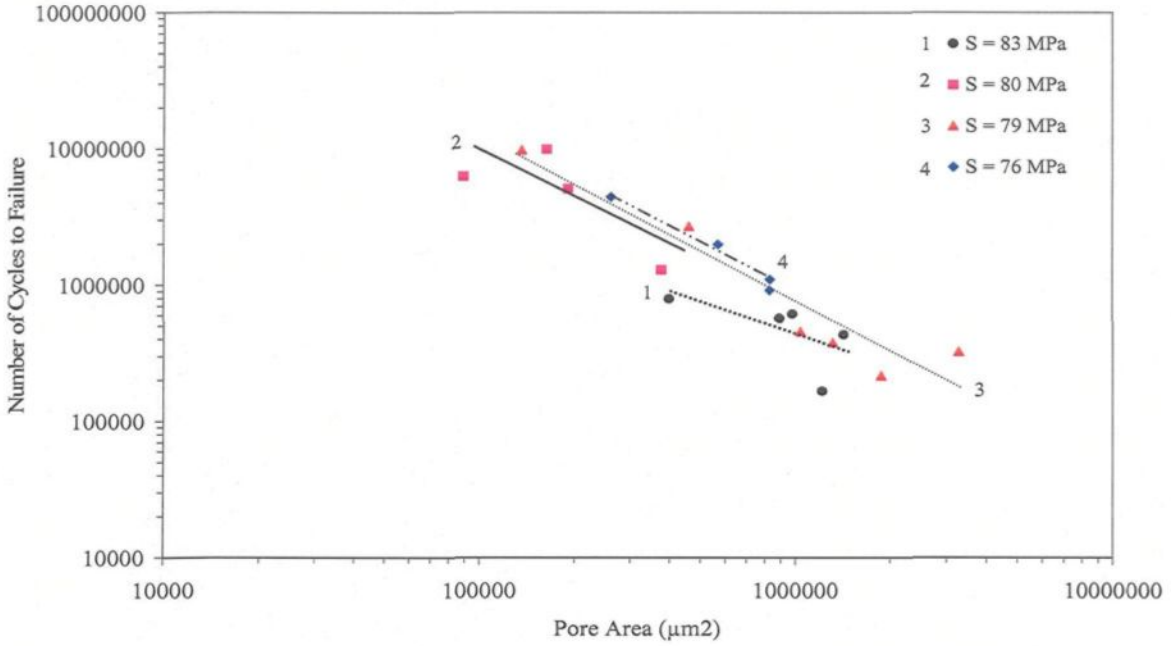


**Figure 4.8** Effect of surface pore size (area) on the fatigue life of LP PM319-F alloy at different stress levels.

tion toward the interior or centre of the sample, where this direction is favored, since the stress gradient decreases on progressing toward the sample interior. When the crack has propagated to a certain extent, the material fails at the point where the cross section of the specimen becomes unable to carry the applied load. A schematic representation of this is shown in Figure 4.9. As the surface pore dimensions increase, the stress concentration associated with the pore increases, as does the stress gradient towards the sample interior, thereby increasing the driving force for fatigue crack propagation and shortening the fatigue life of the sample. The results of Figure 4.8 confirm those shown in Figure 4.7(a), emphasizing, in addition, the effect of an increase in stress amplitude on the fatigue life.

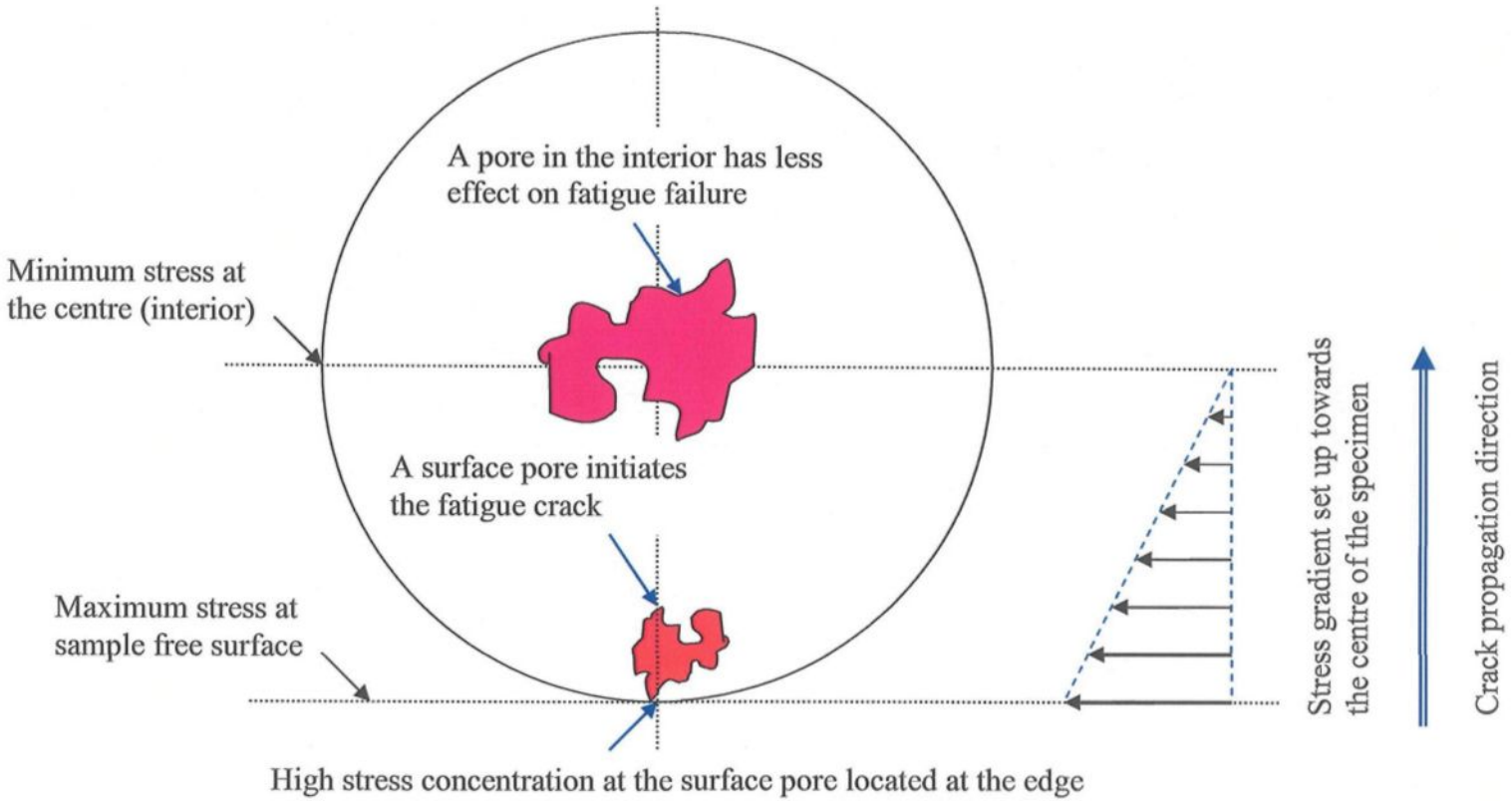


**Figure 4.9** A schematic representation of the stress concentration and stress gradient associated with a surface pore.

### 4.3.2 A356-T6 alloy

The fatigue fracture surfaces of 40 specimens were examined in two conditions: 26 specimens were tested under high cycle fatigue (HCF-where the number of cycles to failure should be greater than $10^4$ cycles) conditions, while the other 14 specimens were tested under low cycle fatigue (LCF-where the number of cycles to failure should be less than $10^4$ cycles) conditions. The fatigue tests were carried out at room temperature (25°C), at a stress ratio R= -1, using a sinusoidal waveform. The stress applied for HCF A356-T6 alloy ranged from 54 MPa to 86 MPa while that for LCF A356-T6 alloy ranged from 157 MPa to 182 MPa.

Here, too, surface porosity was found to have a great influence on the fatigue life of A356-T6 alloy. It was found that in 23 of the 26 samples tested under HCF conditions and 7 of the 14 samples tested under LCF conditions, the fracture occurred due to the presence of a pore at the surface which acted as the main crack initiation site *i.e.* 75% of all tested specimens of A356-T6 alloy fractured due to the effect of surface porosity.

Figure 4.10 shows examples of the SEM images obtained from the fatigue fracture surfaces of two A356-T6 alloy samples tested under high and low cycle fatigue conditions. The arrows in Figure 4.10 (a) and (c) point to the surface pore which initiated the fatigue crack in each case.

The effect of the surface pore parameters on the fatigue life of A356-T6 alloy is shown in Figure 4.11 through Figure 4.13. All conditions are plotted together for the HCF samples in Figure 4.11(a) through Figure 4.11(d), and separately in Figure 4.12 for the

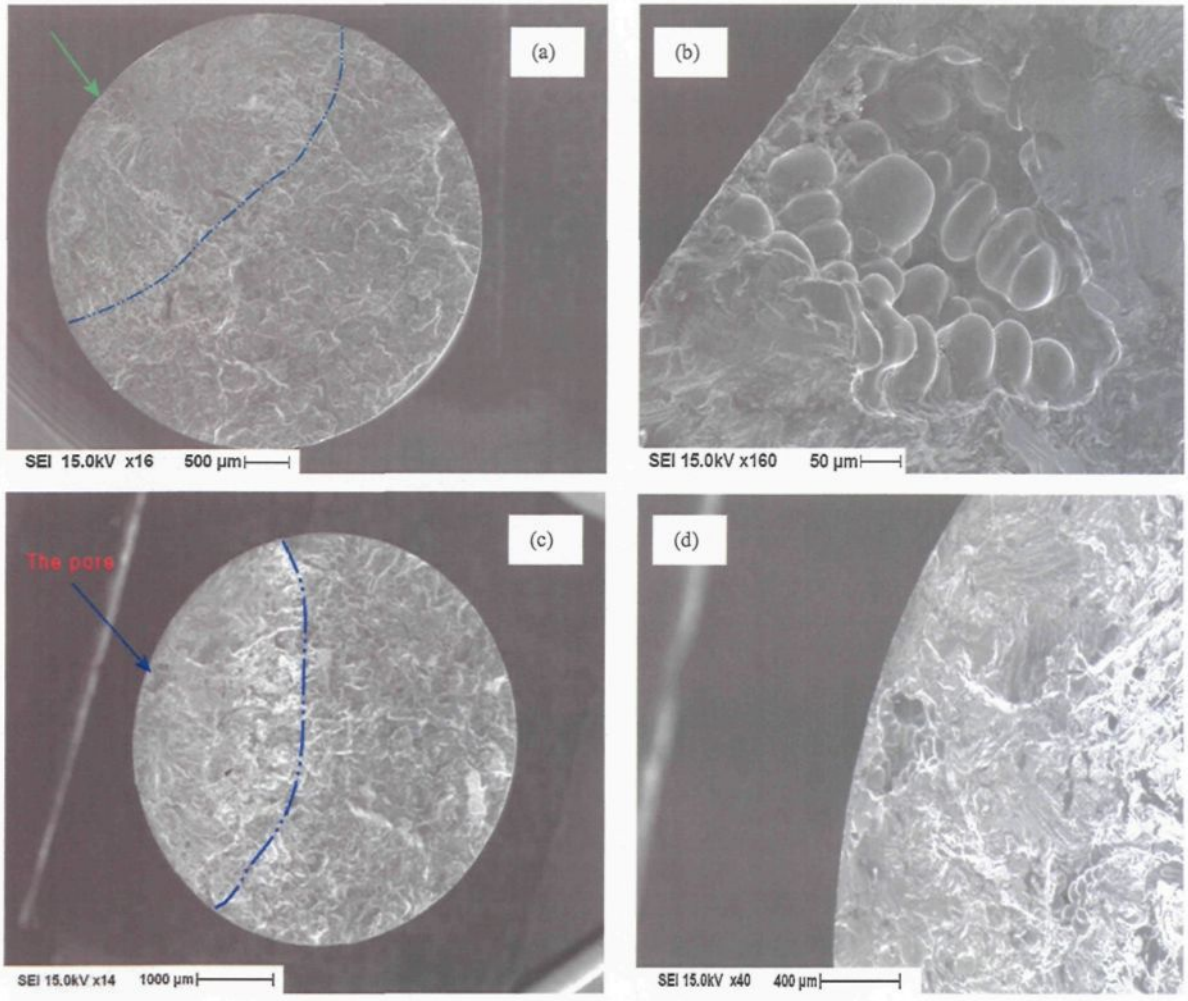


**Figure 4.10** SEM images of the fatigue fracture surfaces of A356-T6-HCF and A356-T6-LCF alloy specimens, taken at: (a, c) low magnification showing the bright area and the crack initiation site; (b, d) high magnification, showing the surface porosity associated with the crack initiation site.

different stress levels used for the HCF samples. As in the case of the 319 alloy, Figure 4.12 shows that for the A356 alloy also, the fatigue life decreases with the increase in stress amplitude and surface pore size.

For the LCF samples, tested at stress levels ranging from 157 MPa to 182 MPa, the results are plotted together in Figure 4.13(a) through Figure 4.13(d), and again reveal the marked decrease in fatigue life with increase in the pore dimensions. As discussed previously, the negative effect of surface pores on the fatigue life is due to the high stress concentration at these surface pores which makes them favoured sites for fatigue crack initiation. Fatigue crack propagation is accelerated in the presence of surface pores, as the stress gradient associated with these pores increases the driving force for crack propagation, shortening the sample fatigue life.

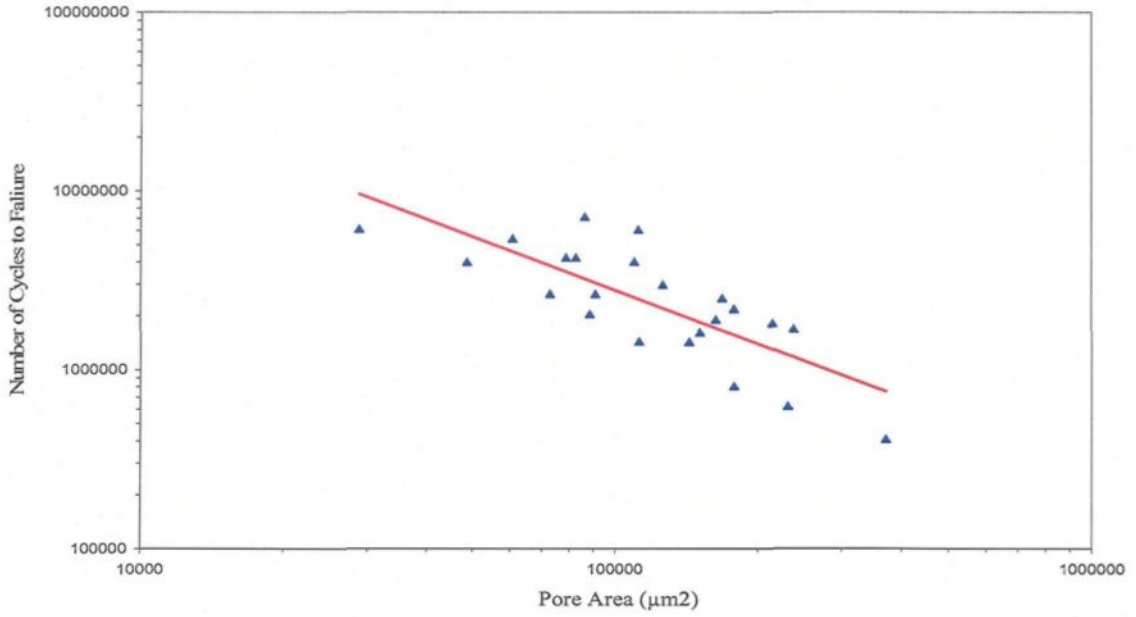


(a)

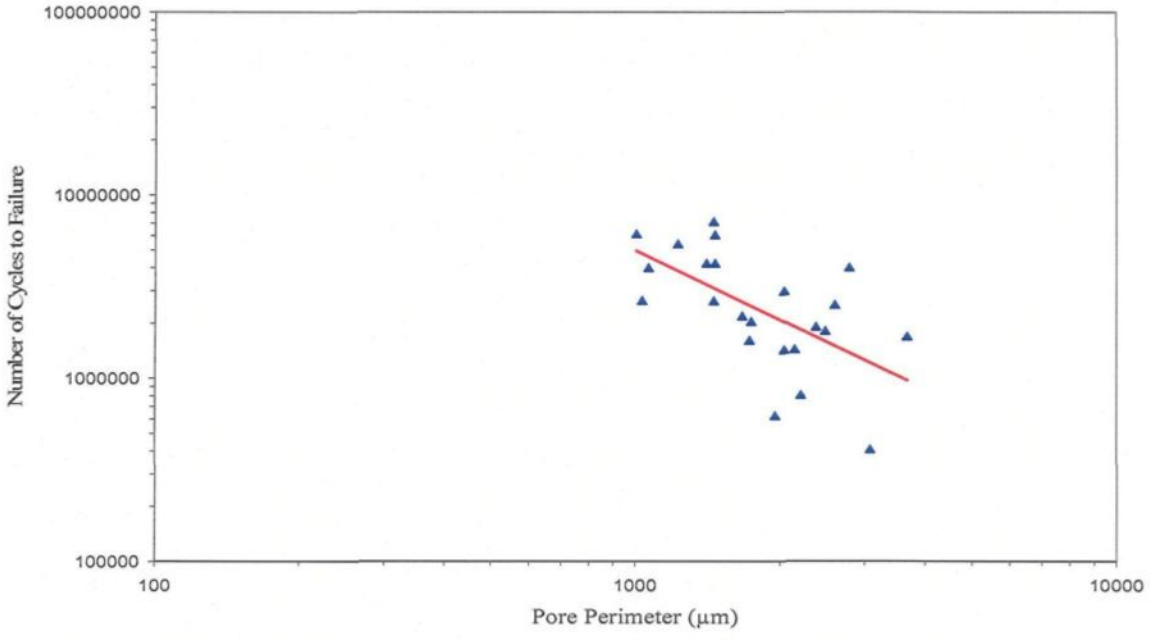


(b)

**Figure 4.11**

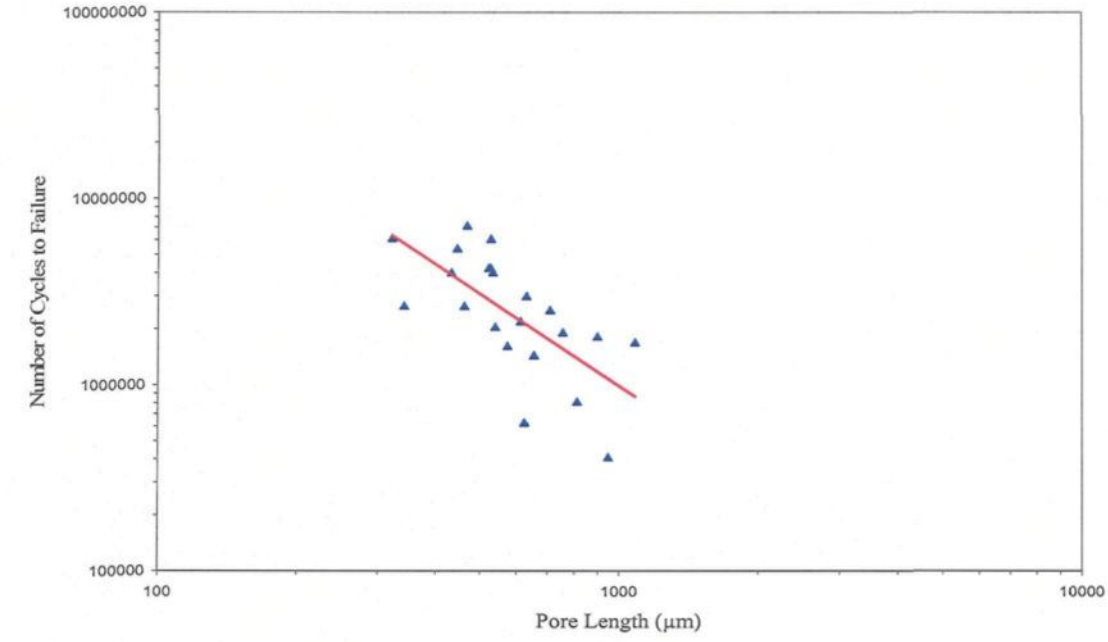


(c)

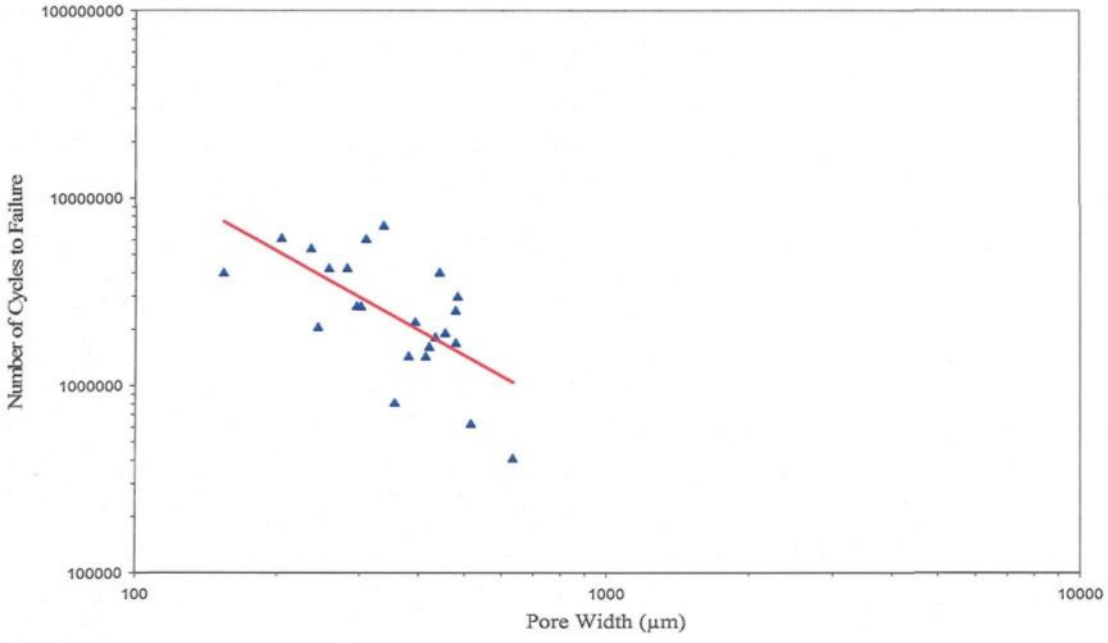


(d)

**Figure 4.11** Effect of surface pore (a) area, (b) perimeter, (c) length, and (d) width on the fatigue life of HCF-A356-T6 alloy.

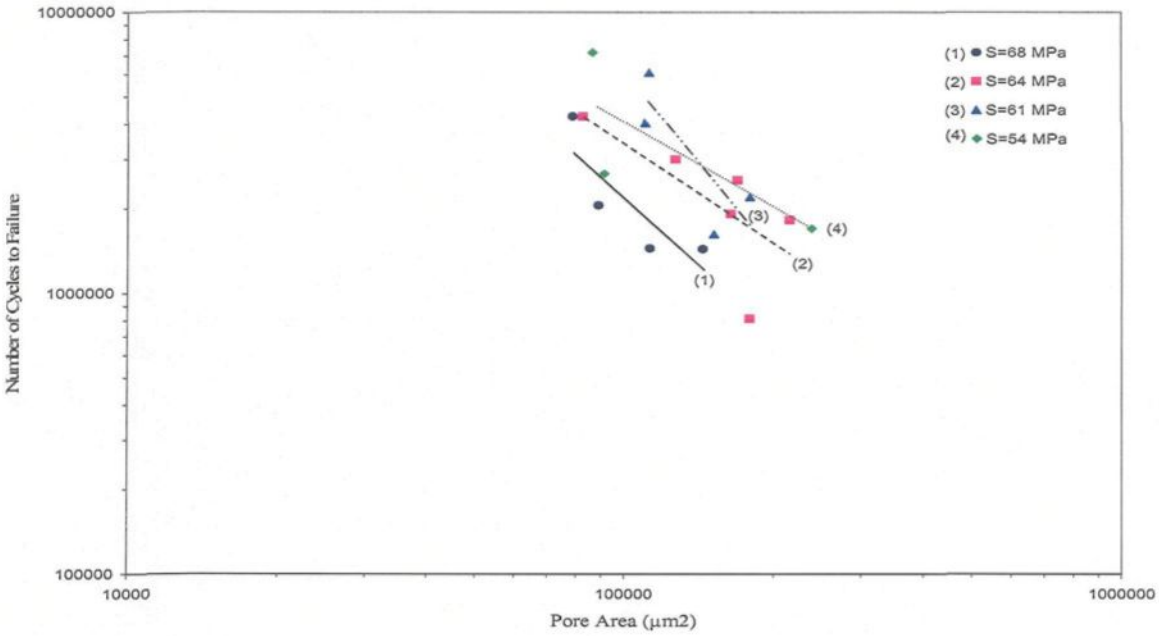


**Figure 4.12** Effect of surface pore size (area) on the fatigue life of HCF-A356-T6 alloy at different stress levels.

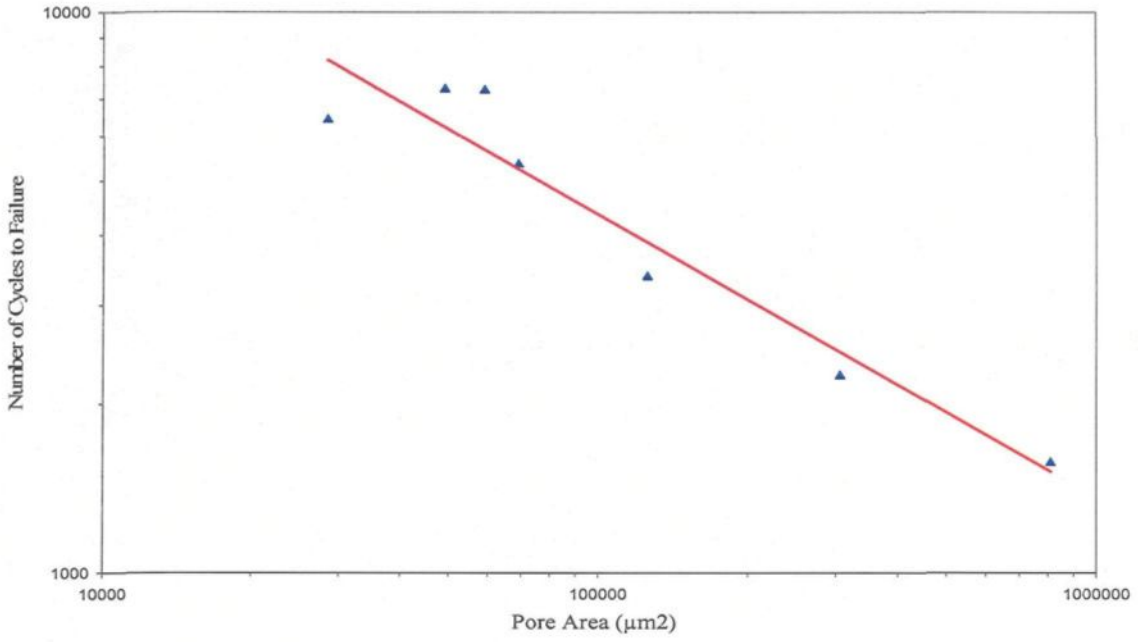


(a)

**Figure 4.13**

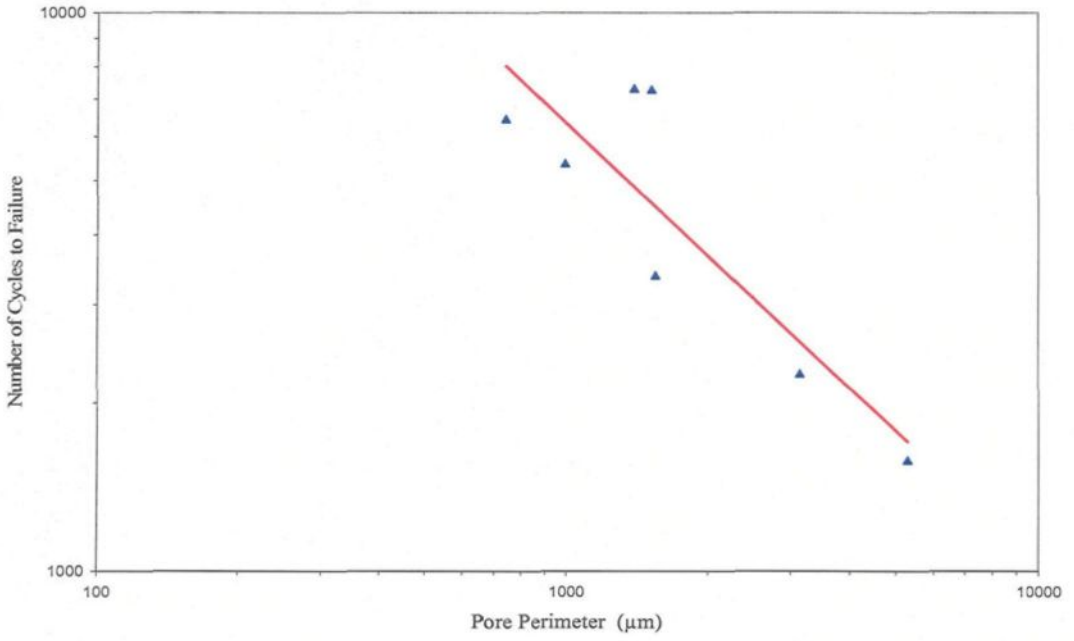


(b)

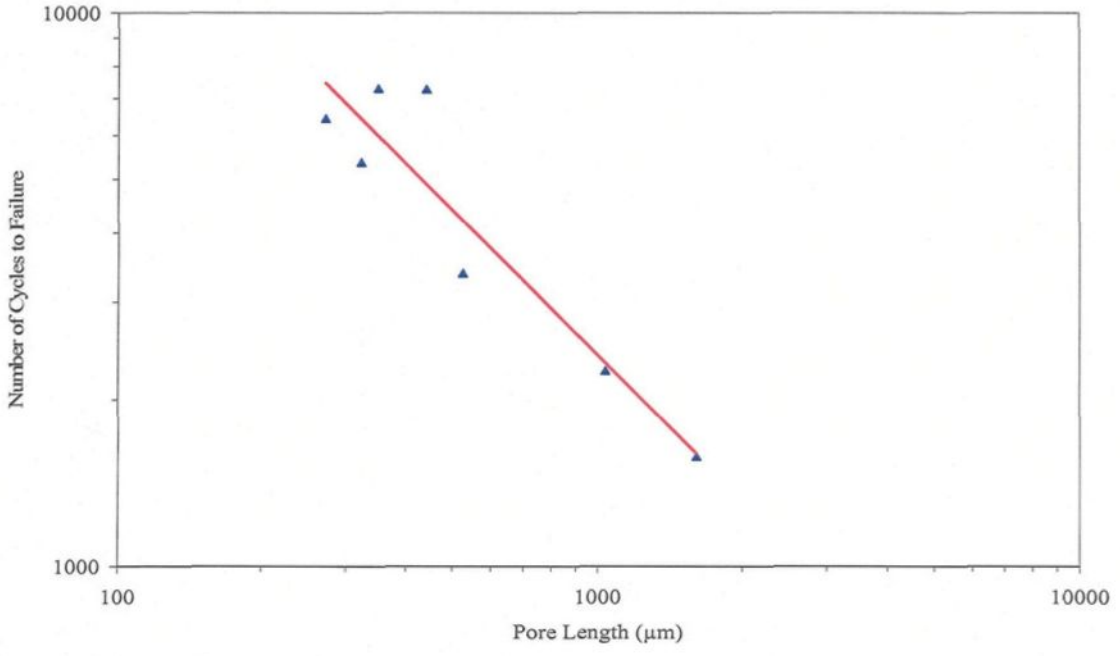


(c)

**Figure 4.13**

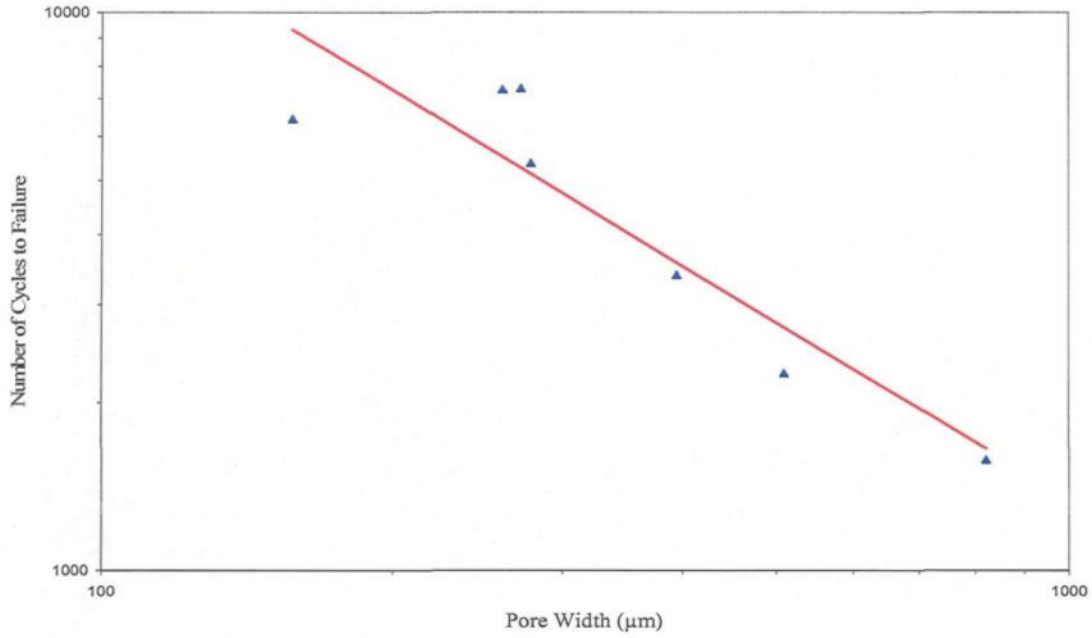


(d)

**Figure 4.13** Effect of surface pore (a) area, (b) perimeter, (c) length, and (d) width on the fatigue life of LCF-A356-T6 alloy.

### 4.3.3 Effect of slip bands on fatigue life of A356-T6 alloy

Slip bands are regions where there is intense deformation due to the shear motion between crystal planes. When a dislocation emerges at the surface, a slip step of one Burgers vector is created. During perfect reversed loading on the same slip plane, this step is cancelled; however, slips occur on many planes, and the reversal is never perfect. Accumulation of slip steps in a local region leads to severe roughening of the surface. This severe localization of plastic strain lowers the resistance to fatigue failure. [44]

In the present study, slip bands acted as the crack initiation site for only two specimens of all the A356-T6 alloy samples examined, where they provided regions of high

stress concentration, making them preferred fatigue crack initiation sites. An example of the SEM image of the fatigue fracture surface of an A356-T6 alloy sample showing the slip bands is given in Figure 4.14. Thus, in the absence of surface porosity, other microstructural constituents such as slip bands can act as preferred fatigue crack initiation sites. However, these constituents have less effect on the fatigue behavior than surface porosity.

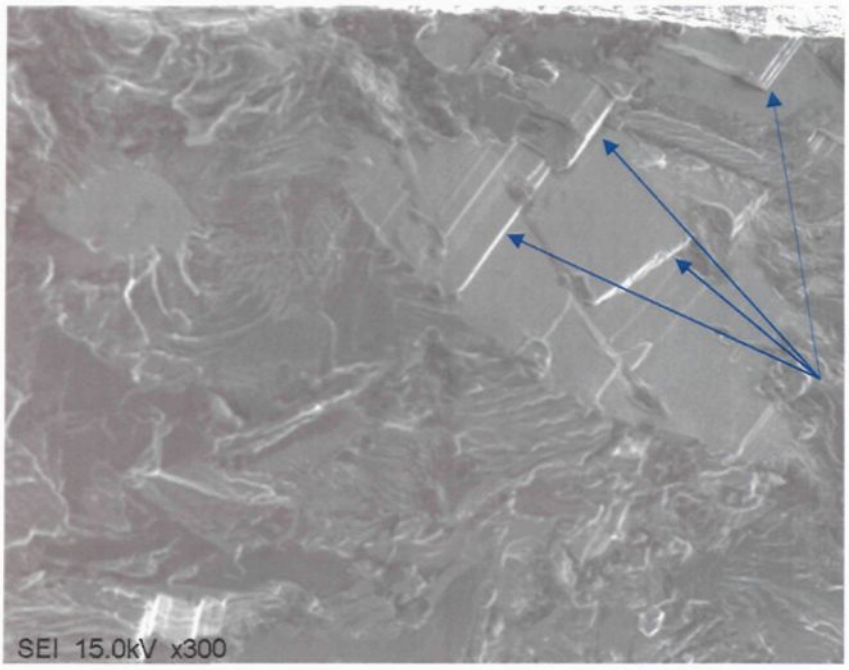


**Figure 4.14** SEM image of the fatigue fracture surface of an A356-T6 specimen, showing the slip bands (arrowed) at the crack initiation site.

### 4.3.4 Comparison of porosity in fractured and run-out samples of LP PM319-F and A356-T6 alloys

The total pore area of fractured and run-out samples (i.e., samples whose fatigue life exceeded $10^7$ cycles without fracture - termed *run-out* or non-fractured samples) of both LP PM319-F and A356-T6 alloys was measured to determine the effect of porosity on the fatigue life in the two cases. The corresponding samples were sectioned from the shoulder and polished for metallography. The total porosity on the polished surface was measured using the image analyzer over 40 fields at 50X magnification for LP PM319-F alloy and over 20 fields at 50X magnification for A356-T6 alloy. Table 4.3 and Figure 4.15 compare the results obtained. As can be seen, porosity is observed in both fractured and run-out samples.

The run-out samples are not sound since they contain porosity, as shown in Figure 4.16. In fact, as Table 4.3 and Figure 4.15 show, the run-out samples exhibit higher porosity than the fractured samples, even when their fatigue life is greater than that of the latter. This can be explained in terms of the effect of pore location (at the surface periphery or interior) on the fatigue life, where the occurrence of porosity within the interior of the sample has much less influence on fatigue crack propagation than if it were located near the fatigue sample surface periphery, as illustrated in Figure 4.9.

**Table 4.3** Porosity in fractured and run-out samples

| Alloy | Sample Type | Pore Area ($\mu m^2$) | |
|---|---|---|---|
| | | Total | S.D. |
| LP PM319-F | Fractured Sample | 1448445 | 22195 |
| | Run-out Sample | 2397488 | 18153 |
| A356-T6 | Fractured Sample | 671320 | 22322 |
| | Run-out Sample | 1215643 | 19349 |

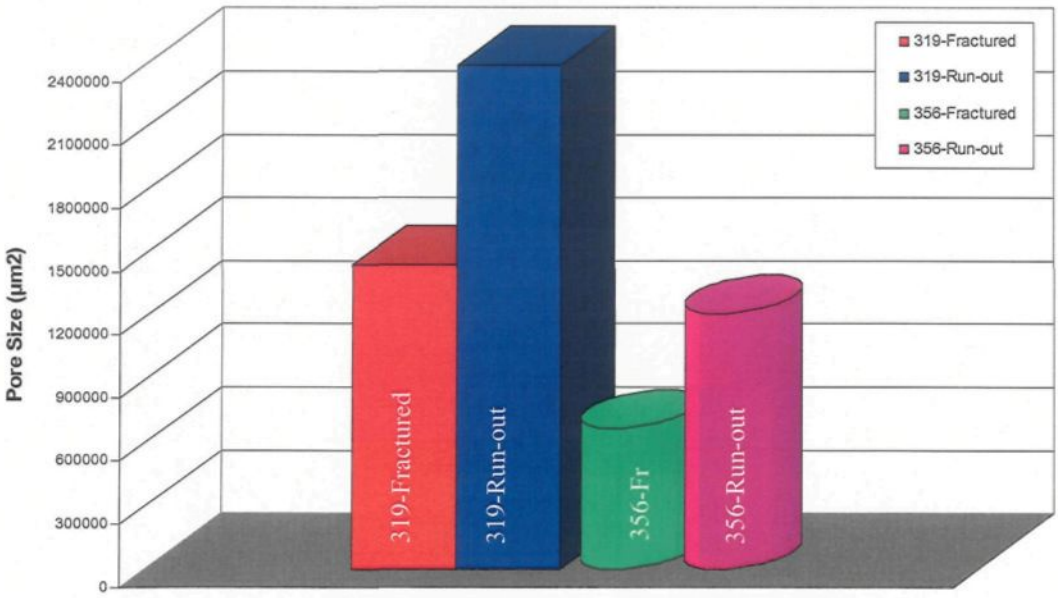


**Figure 4.15** Comparison between total pore areas in fractured and run-out samples.

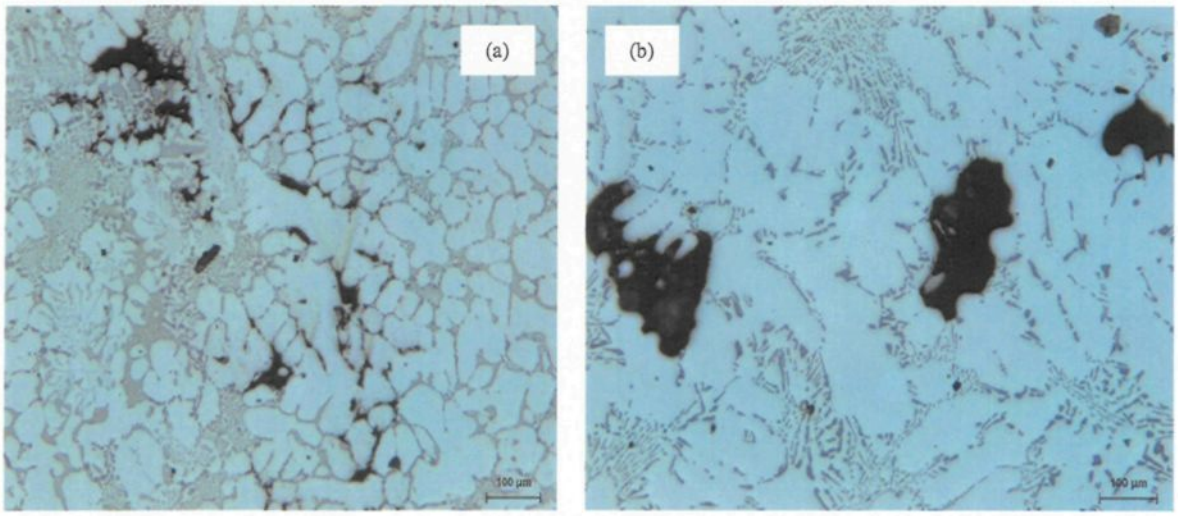


**Figure 4.16** Optical micrographs showing porosity observed in run-out samples of (a) LP PM319-F and (b) A356-T6 alloys.

### 4.3.5 Comparison of the fatigue behavior of LP PM319-F and A356-T6 alloys

Based on the results obtained, a comparison of the effect of surface pore size on the fatigue behavior of LP PM319-F and A356-T6 alloys was made, as shown in Figure 4.17. Apparently, the LP PM319-F alloy showed a better fatigue life in spite of the fact that the surface pore sizes measured were larger than those observed in the A356-T6 alloy samples.

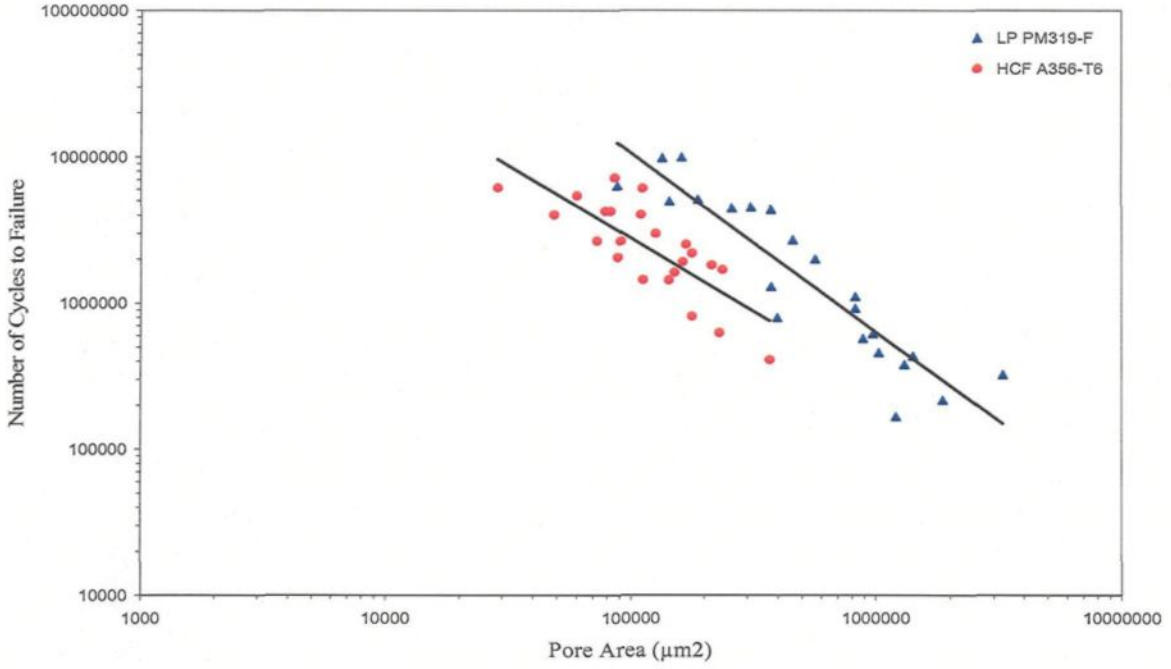


**Figure 4.17** Comparison of the effect of surface pore size on the fatigue life of LP PM319-F and A356-T6 alloys.

To understand the reason for this contradiction in behavior, the SEM technique by which the porosity measurements were carried out was re-evaluated, to determine the actual pore size responsible for the fatigue crack initiation in the two alloys. Porosity measurements were carried out using both optical microscopy and scanning electron microscopy. In the first case, longitudinal sections of the fractured samples were employed,

as shown in Figure 4.18. The porosity measurements were carried out at 10X magnification so as to cover the extent of the porosity observed (arrowed), and the average pore size was determined accordingly. It is clear from Figure 4.18 that the nature of the surface porosity in the two alloys is different: in the LP PM319-F alloy, the surface porosity seems to consist of many small individual pores or multiple pores, whereas that in A356-T6 consists of a large single pore. In the second case, the pore sizes were determined from SEM images similar to those shown in Figure 4.19, which provides examples of the multiple pores and single pore observed in samples of LP PM319-F and A356-T6 alloys, respectively. The higher magnification images in (b) and (d) clearly show the small individual pores within the delineated regions marked in (a) and (c) in the two cases.

Table 4.4 and Figure 4.20 summarizes one set of the results obtained using the two porosity measurement techniques. From Figure 4.18 and the results plotted in Figure 4.20, we can observe that the actual pore size that initiated the fatigue crack in LP PM319-F alloy is much smaller than that in A356-T6 alloy, indicating that the fatigue life for LP PM319-F alloy is expected to be greater than that of A356-T6 alloy, which is what is actually observed.

**Table 4.4** Porosity measured by the SEM and optical microscopy/image analysis techniques.

| LP PM319-F | | A356-T6 | |
|---|---|---|---|
| SEM, pore area ($\mu m^2$) | OM, average pore area ($\mu m^2$) | SEM, pore area ($\mu m^2$) | OM, pore area* ($\mu m^2$) |
| 890374 | 361 | 178465 | 63747 |
| 1420595 | 161 | 143324 | 66348 |

* pore responsible for crack initiation was easily identified, OM: optical microscopy

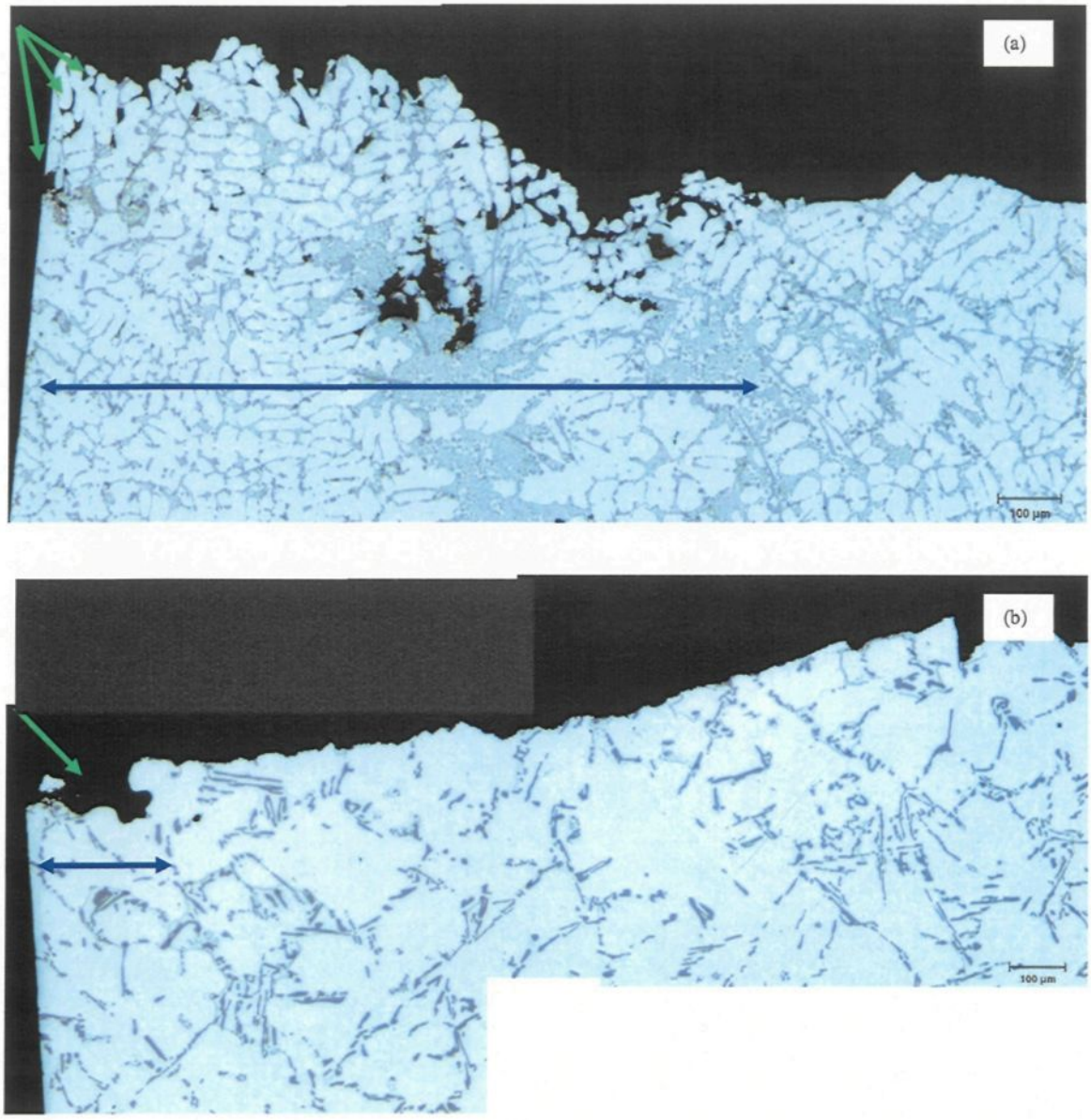


**Figure 4.18** Longitudinal sections of fractured fatigue samples, showing the surface pore size responsible for fatigue crack initiation in (a) LP PM319-F and (b) A356-T6 alloys.

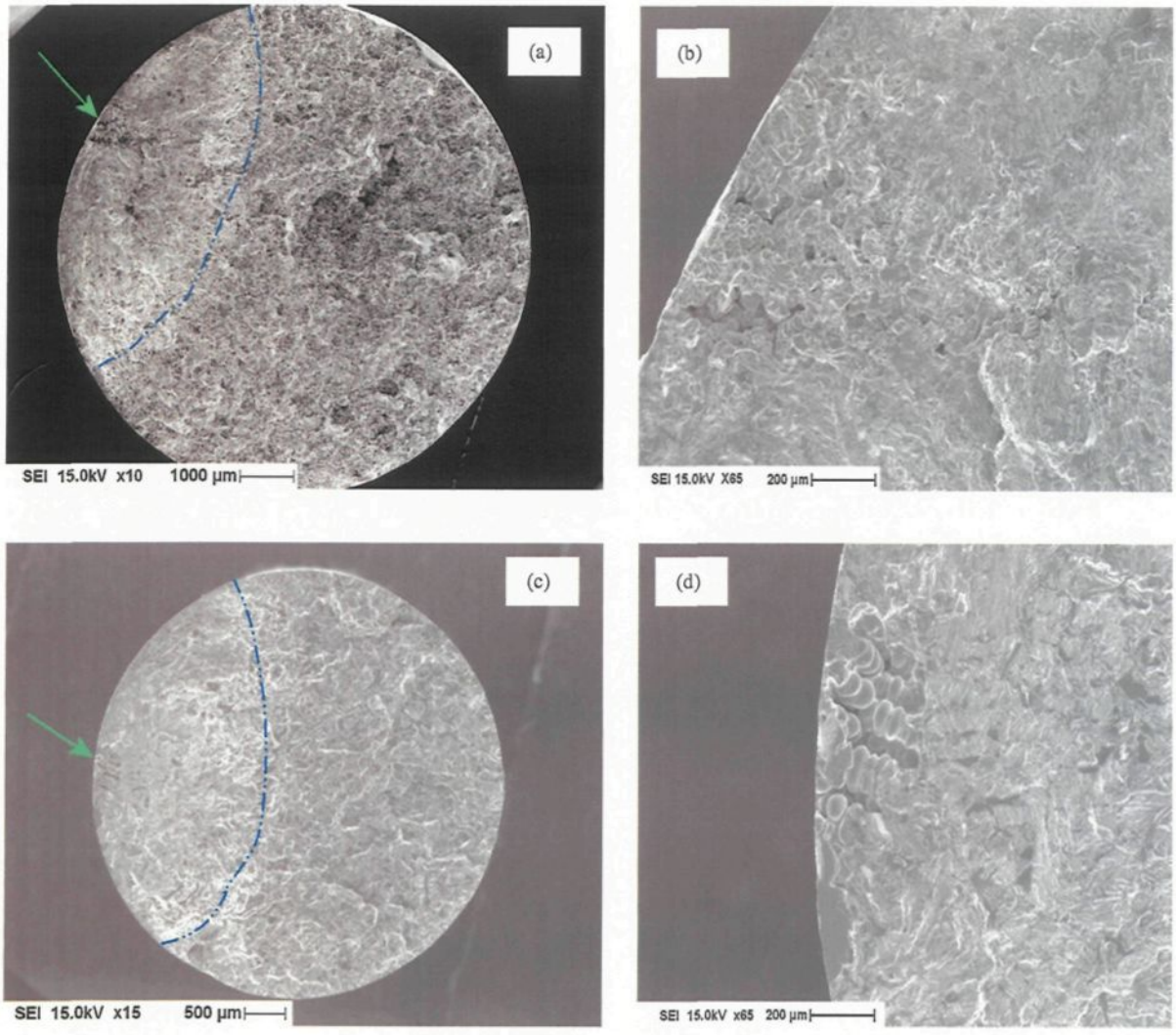


**Figure 4.19** SEM images showing the pore responsible for fatigue crack initiation in (a, b) LP PM319-F, and (c, d) A356-T6 alloys.

Figure 4.21 compares schematically, the effect of small multiple pores in the 319 alloy sample versus that of the large single pore in the A356 alloy sample. In the first case, the propagation of the crack from one small pore to the next will take a longer time, as the crack will have to cross the solid matrix between these pores (represented by the short dashed lines), increasing the resistance to crack propagation and, hence, the fatigue life. In the case of the A356 alloy sample, the high stress concentration associated with the large single pore at the periphery of the sample will increase the driving force for crack propagation and thus reduce the fatigue life of the sample.

The microstructural characteristics in the two cases are also another factor to consider. As was shown in Figure 4.1 through Figure 4.5, the SDAS, eutectic Si particle characteristics and grain size in the LP PM319-F alloy were much finer than those observed for the A356-T6 alloy. The presence of the $\alpha$-Fe, and Mg and Cu phases in the former also improved the matrix stiffness and resistance to crack propagation.

In view of the above, it is then possible to understand why the fatigue life of LP PM319-F alloy is much better than that of A356-T6 alloy, in spite of the fact that the porosity measurements using the SEM technique/images show a larger porosity in the LP PM319-F alloy. In the case of multiple pore crack initiation sites (LP PM319-F alloy), the SEM technique is not adequate enough to determine the actual pore size which initiates the fatigue crack. In the case of a single pore fatigue crack initiation site (A356-T6 alloy), the SEM technique can be applied with great accuracy.

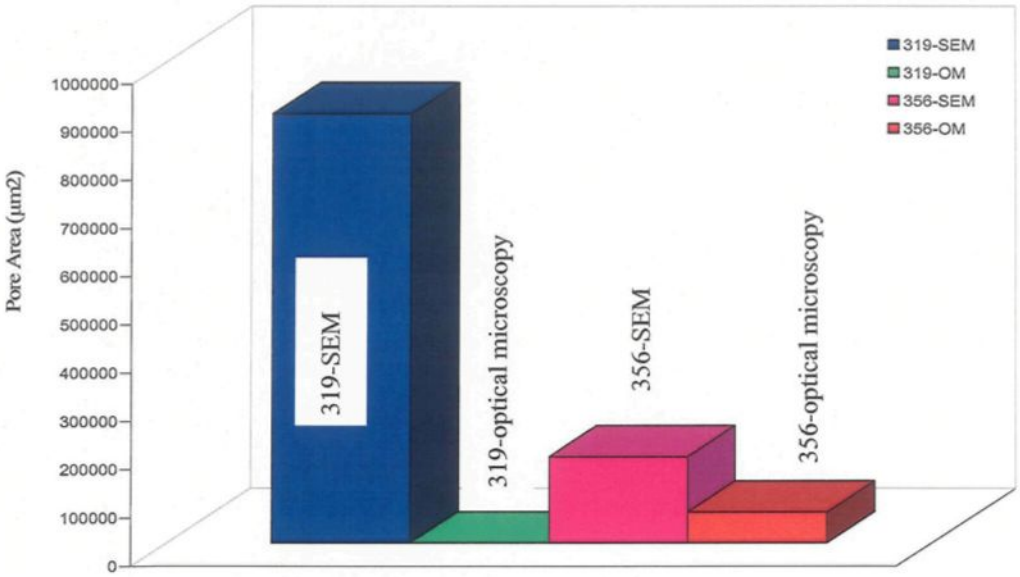


**Figure 4.20** The surface pore size responsible for fatigue crack initiation in LP PM319-F and A356-T6 alloys, measured by the SEM and optical microscopy techniques.

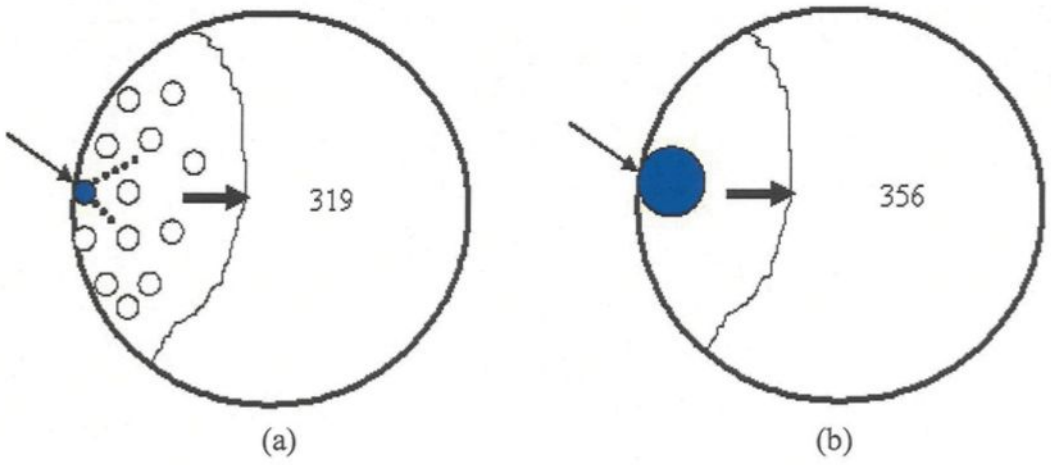


**Figure 4.21** A schematic representation showing the nature of surface porosity which initiates the fatigue crack in (a) LP PM319-F and (b) A356-T6 alloys. The thin arrows refer to the fatigue crack initiation site, while the thick arrows indicate the crack propagation direction.

## 4.4 EFFECT OF HIPPING ON THE FATIGUE LIFE OF C354-T6 CASTING ALLOY

Aluminum-silicon-copper-magnesium hypoeutectic alloys such as C354 alloy have a greater response to heat treatment as a result of the combination of Mg and Cu. These alloy types offer excellent strength and hardness with some sacrifice in ductility and corrosion resistance. The alloy castings used in the present work were typically T6 heat-treated for optimal properties. As mentioned previously, there is a wide area for the applications of these alloys, including engine cooling fans, crankcases, high speed rotating parts such as fans and impellers, structural aerospace components, air compressor pistons and fuel pumps.

Hot isostatic pressing (HIPping) of castings is recognized as a process of forming or bonding materials at high temperatures with high hydrostatic pressure acting on all surfaces simultaneously. It is considered as a means of providing improved internal soundness or integrity, increased density and improved properties. The process was developed to significantly improve the mechanical properties and fatigue strength of aluminum alloys since it helps to minimize or eliminate pores. [9, 63, 75]

### 4.4.1 Fatigue behavior of HIPped samples

The effect of HIPping on the fatigue life of 31 fatigue-tested samples of C354-T6 alloy was investigated by comparing the fatigue behavior of both HIPped (11 specimens) and non-HIPped samples (20 specimens). In the HIPped samples, it was found that the fatigue fracture occurred due to the presence of different types of crack initiation sites: a surface pore of much smaller size was observed to be responsible for fatigue crack

initiation in one sample only, four samples fractured under the effect of oxide films acting as the main crack initiation site, two samples fractured under the effect of slip bands, and the other samples fractured due to unidentified sources. In the non-HIPped samples, it was observed that all the specimens tested fractured on account of a large surface pore acting as the main crack initiation site, indicating that porosity was 100% responsible for fatigue crack initiation in this case. The reduced number of pores and the elimination of large pores in the HIPped samples is normal due to the effect of the HIPping process. In comparison, the non-HIPped samples contain large pores, as shown in Figure 4.22.

A comparison of the fatigue behavior of HIPped and non-HIPped samples is presented in Figure 4.23 which shows clearly that the fatigue life of the HIPped samples is much higher compared to that of non-HIPped samples, related directly to the elimination of porosity as a result of the HIPping process. In the absence of surface porosity, other crack initiation sites become operative, such as oxide films and slip bands. The short fatigue life of the non-HIPped samples is directly related to the presence of large surface pores, considered the most detrimental of crack initiation sites. Figure 4.24 presents examples of the crack initiation sites observed in HIPped samples.

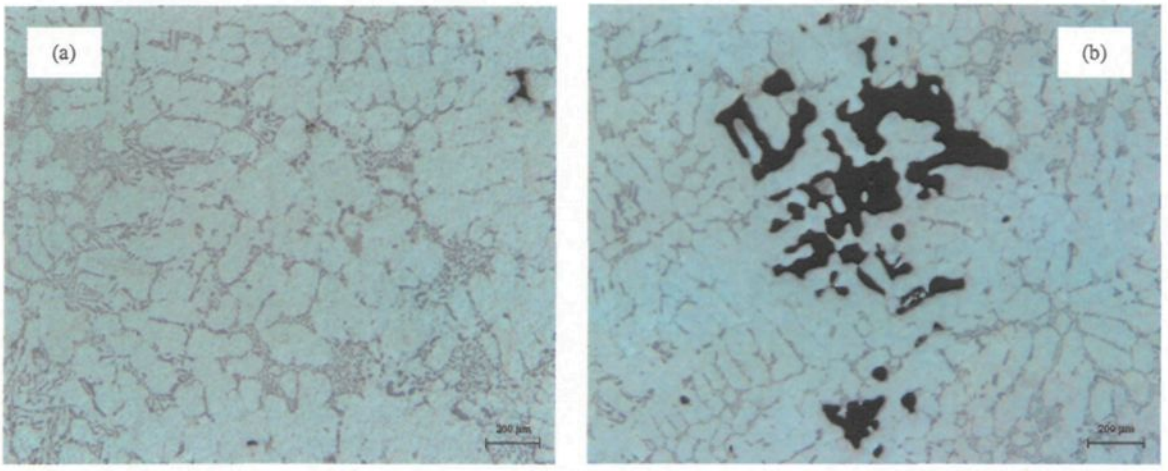


**Figure 4.22** Optical micrographs showing porosity in (a) HIPped, and (b) non-HIPped C354-T6 alloy samples.

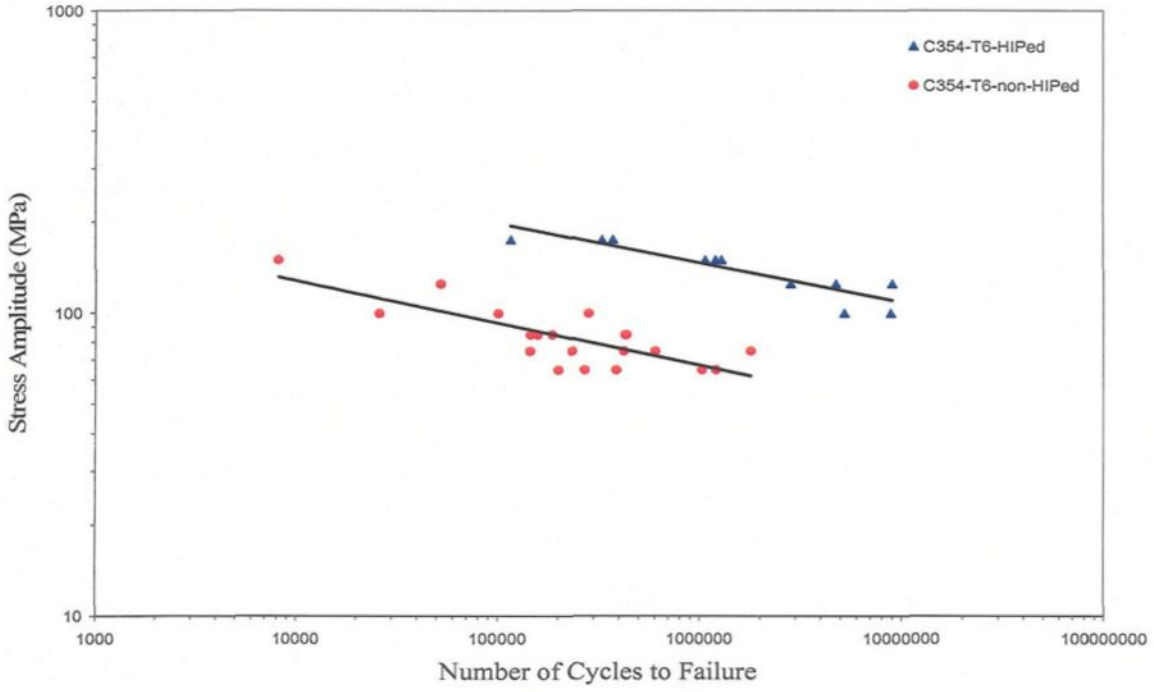


**Figure 4.23** Comparison between the fatigue life of HIPped and non-HIPped samples of C354-T6 alloy.

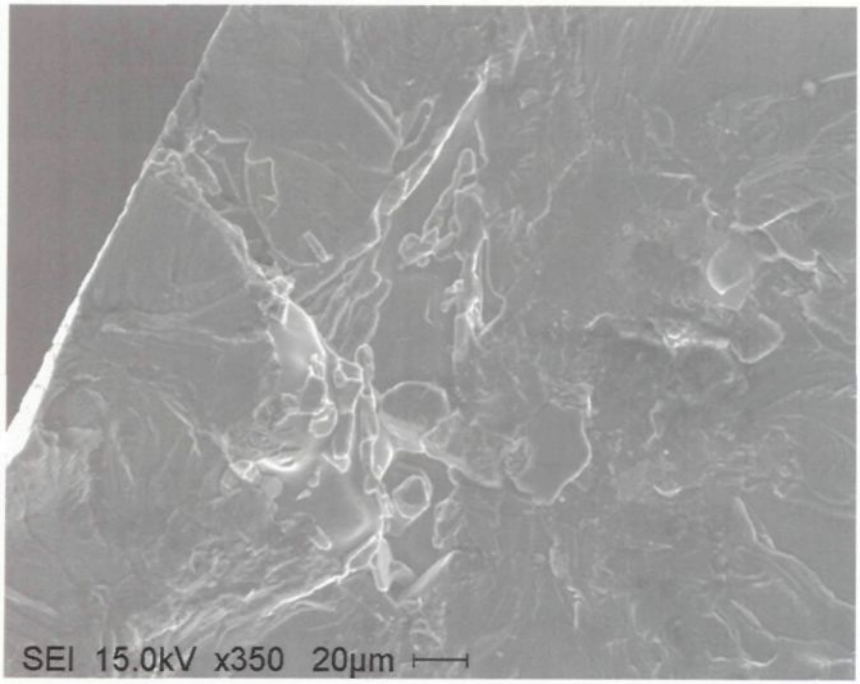


(a)

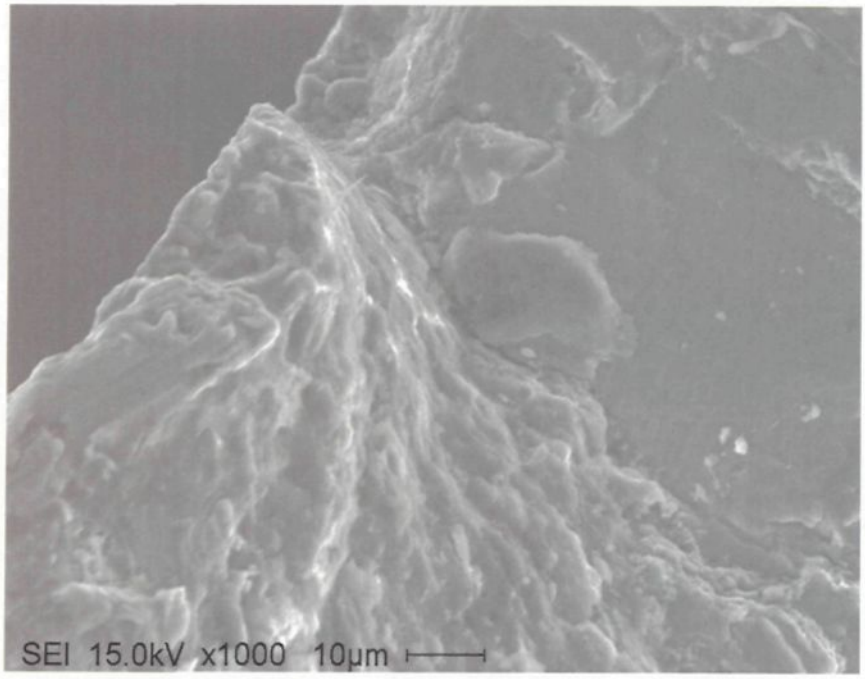


(b)

**Figure 4.24**

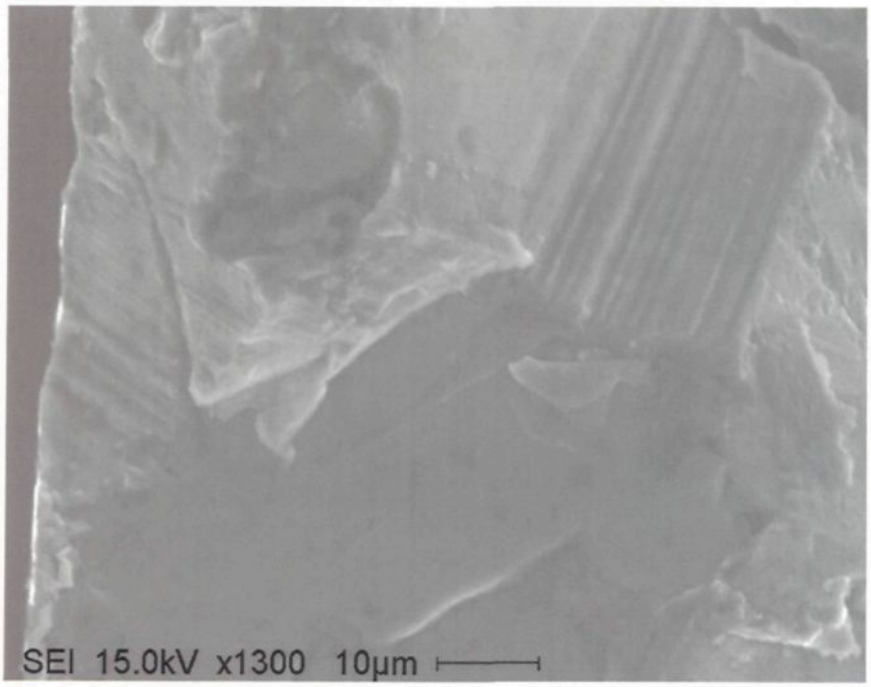


(c)

**Figure 4.24** SEM images showing the fatigue crack initiation sites observed in HIPped samples: (a) surface pore, (b) oxide films, and (c) slip bands.

### 4.4.2 Fatigue behavior of non-HIPped samples

In the non-HIPped samples, all the 20 specimens tested fractured due to the presence of large surface pores that acted as the main crack initiation site, indicating that porosity was 100% responsible for fatigue crack initiation. Figure 4.25 shows an example of the SEM images obtained from the fatigue fracture surface of a non-HIPped C354-T6 alloy sample. The arrow in Figure 4.25(a) points to the pore which initiated the fatigue crack. Quantitative measurements of the surface pores which initiated the fatigue crack were carried out using image analysis and the results of the effect of surface pore size, perimeter, length, and width on the fatigue life of non-HIPped C354-T6 alloy are shown in

Figure 4.26 and Figure 4.27. The fatigue testing was carried out at room temperature (25°C), using a stress ratio R= -1, a sinusoidal waveform, and under high cycle fatigue conditions. The stress applied ranged from 65 MPa to 100 MPa. The results obtained are plotted together in Figure 4.26 showing the effect of surface pore dimensions on the fatigue life, and separately in Figure 4.27 showing the effect of surface pore size on the fatigue life at each stress level, confirming the results shown in Figure 4.26(a): as surface pore size increases, the fatigue life decreases at each stress level. At the same time, the fatigue life also decreases with the increase in stress amplitude.

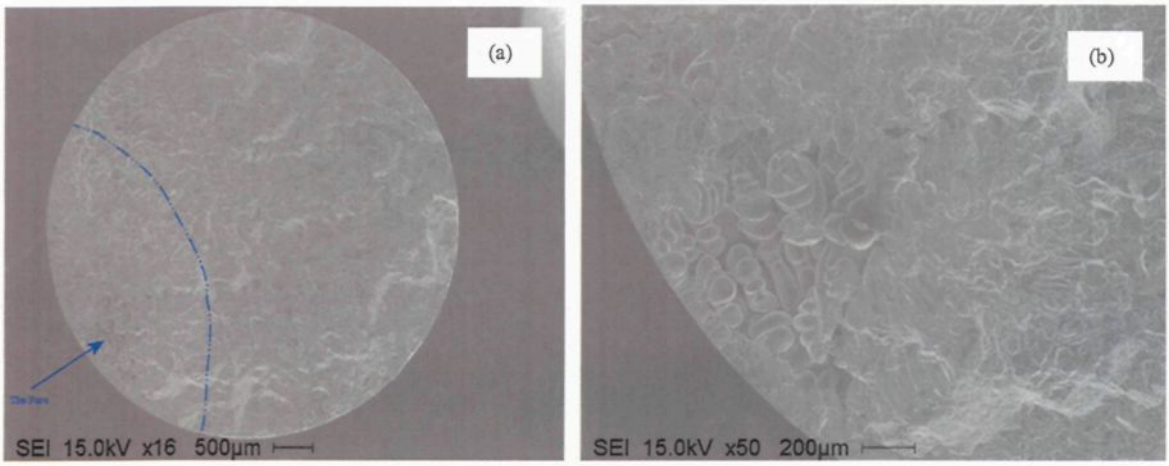


**Figure 4.25** SEM images showing the fatigue fracture surface of a non-HIPped C354-T6 alloy sample, taken at (a) low magnification, showing the bright area and the crack initiation site, (b) high magnification, showing the surface porosity associated with the crack initiation site.

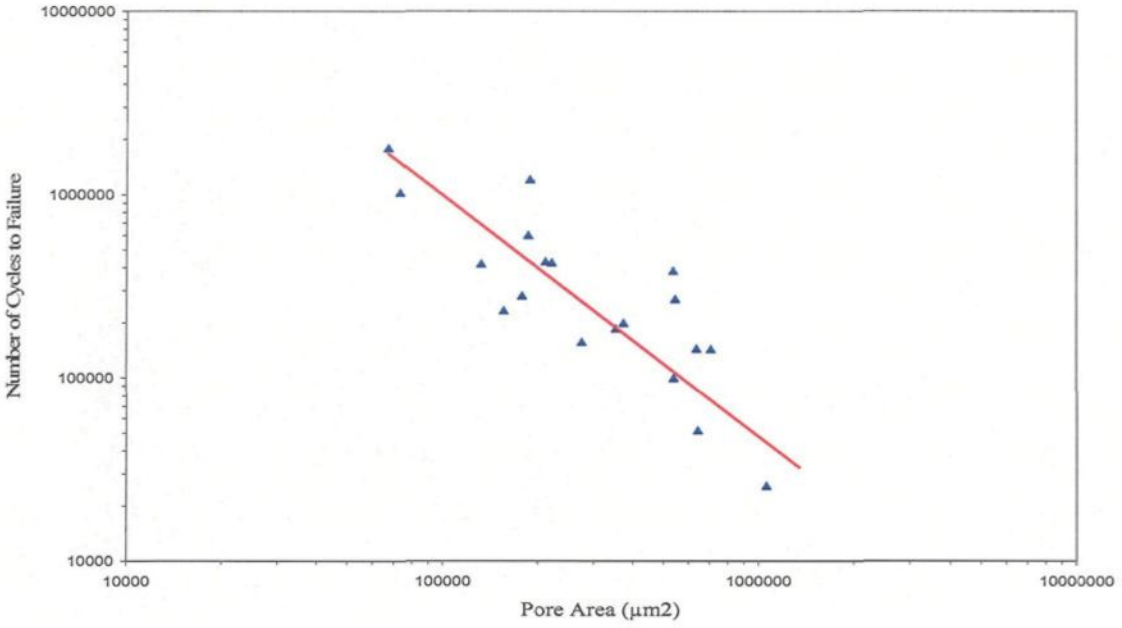


(a)

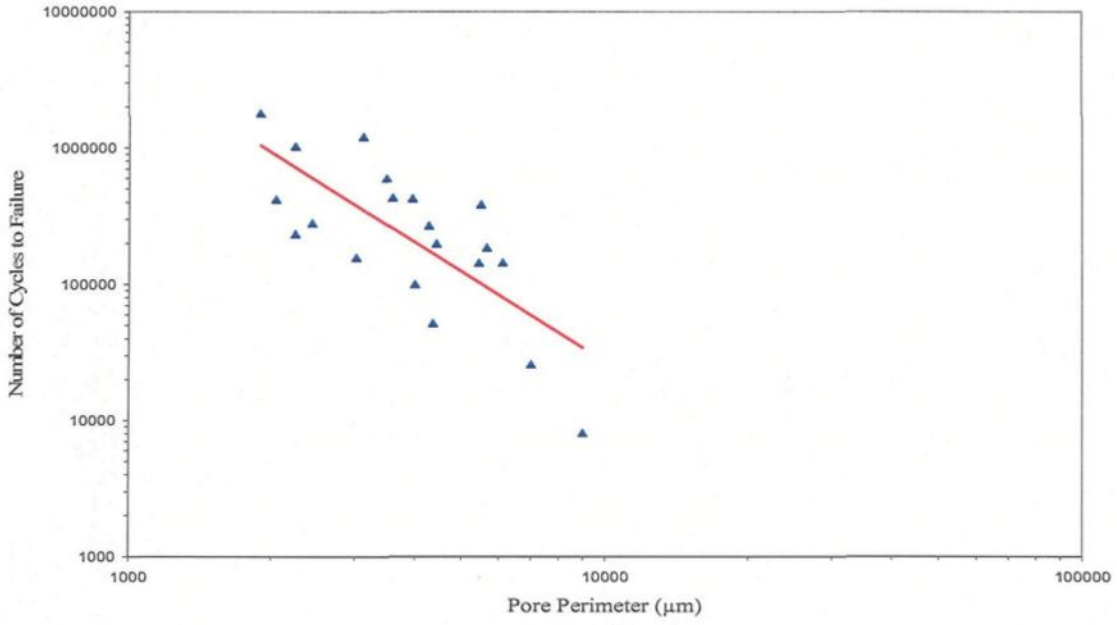


(b)

**Figure 4.26**

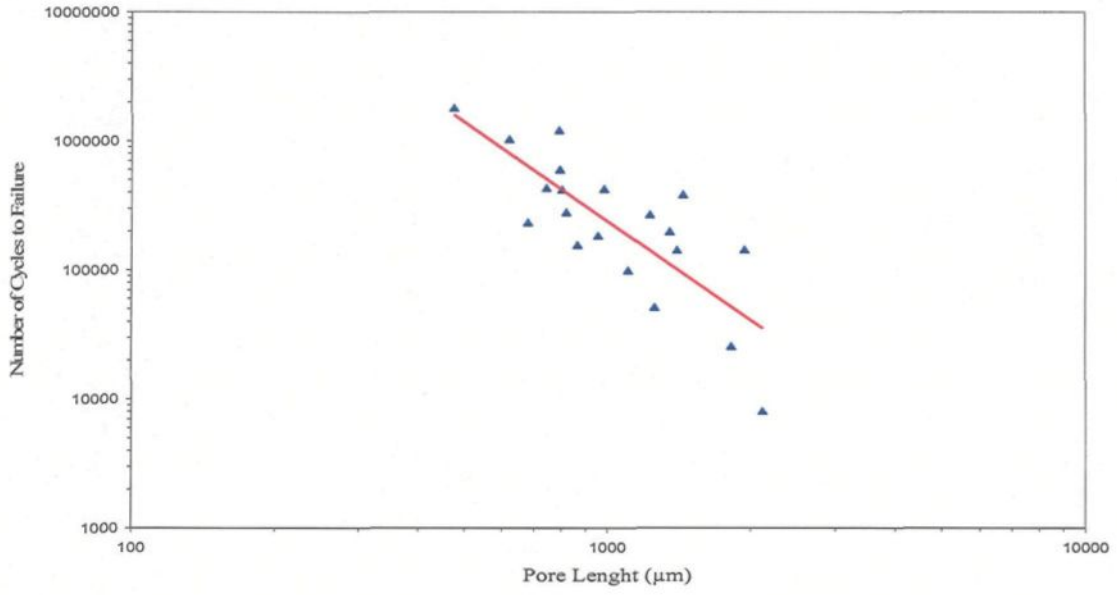


(c)

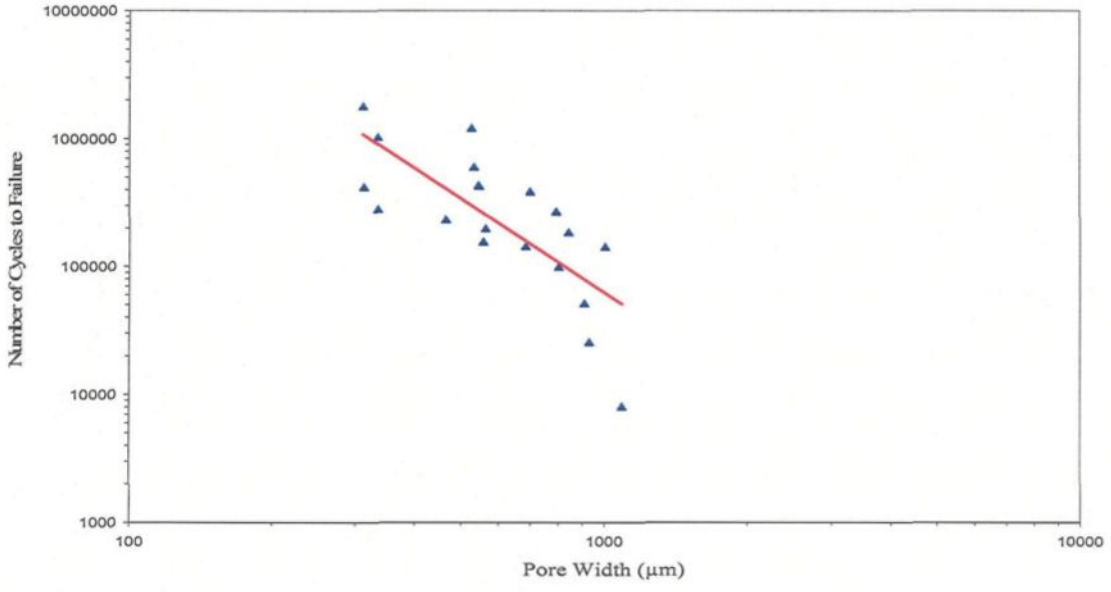


(d)

**Figure 4.26** Effect of surface pore (a) area, (b) perimeter, (c) length, and (d) width on the fatigue life of non-HIPped C354-T6 alloy.

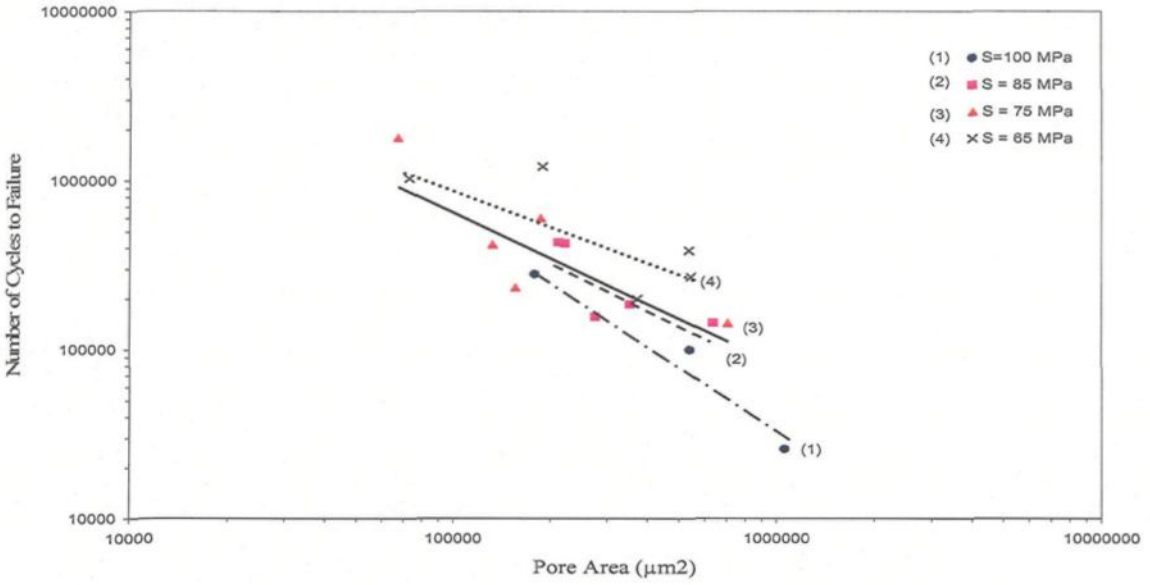


**Figure 4.27** Effect of surface pore size (area) on the fatigue life of non-HIPped C354-T6 alloy at different stress levels.

## 4.5 EFFECT OF POROSITY ON THE FATIGUE LIFE OF HYPEREUTECTIC AE425 AND PM390 CASTING ALLOYS

Two Al-Si-Cu-Mg hypereutectic alloys were selected for study in the present work, PM390 (i.e., permanent mold die-cast process 390) and AE425 alloys, as they have a wide range of application in the automotive industry. The fracture surfaces of 63 fatigue-tested samples obtained from these alloys were examined, as in the case of the hypoeutectic alloys, to correlate the porosity observed on the fracture surface with the fatigue life.

### 4.5.1 Microstructure of PM390 and AE425 alloys

The microstructure exhibited by the AE425 and PM390 alloys is characterized by the presence of a number of polygonal dark grey primary Si particles, as shown in Figure 4.28. Such hypereutectic alloys are used mainly for their wear resistance which is enhanced due to the presence of the hard primary silicon particles.

In order to improve the properties, especially the wear resistance, phosphorous was added (0.008 wt%) to both alloys, to provide refined, well-dispersed primary silicon particles in the microstructure. A small amount of clustering of the primary silicon particles is observed in the microstructure of the AE425 alloy sample shown in Figure 4.28(a), while the high cooling rate associated with the die cast PM390 alloy provides somewhat finer primary silicon particles as shown in Figure 4.28(b).

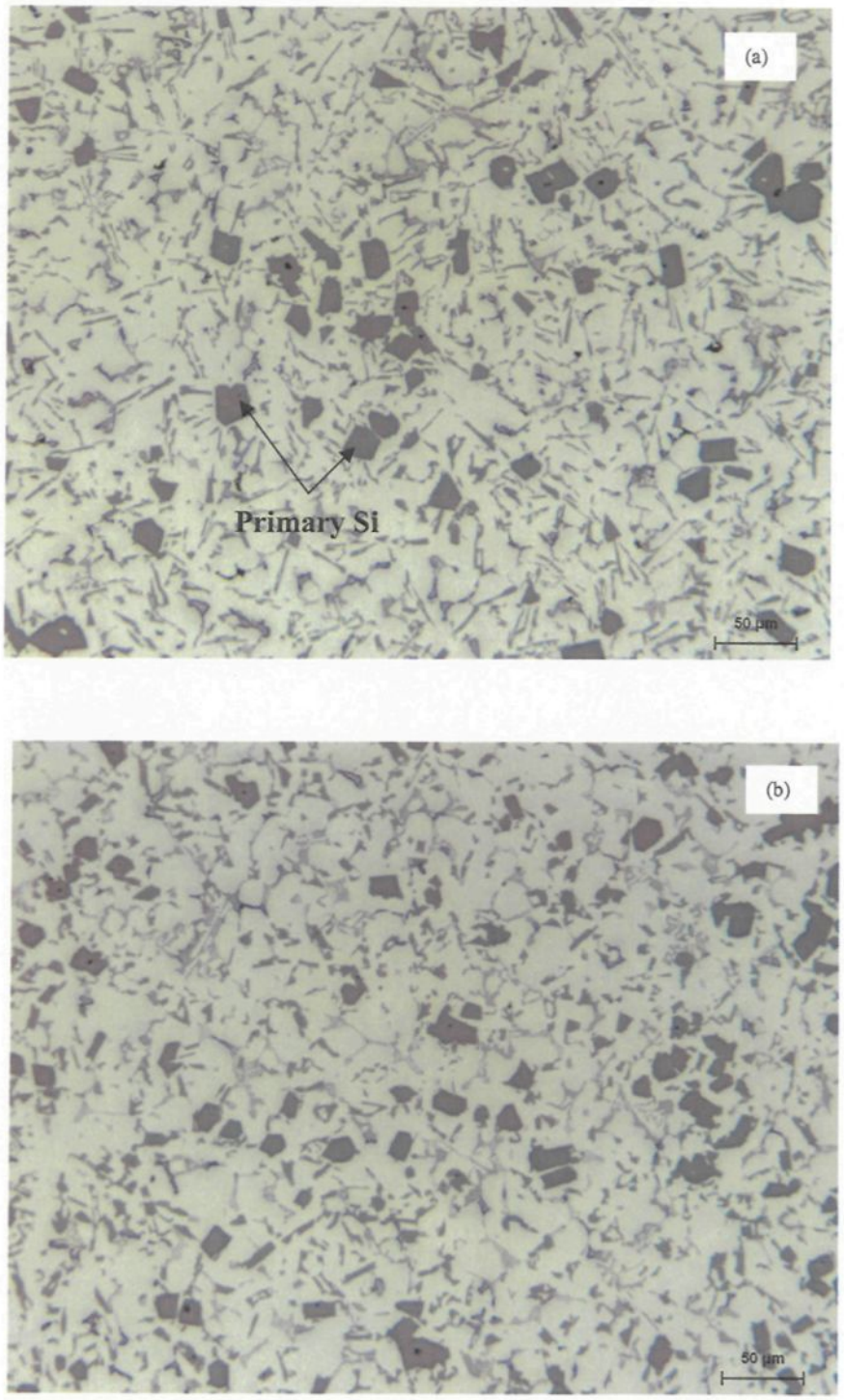


**Figure 4.28** Optical micrographs showing the microstructures of (a) AE425, and (b) PM390 alloys.

### 4.5.2 Fractography of AE425 and PM390 alloys

The fatigue fracture surfaces of the AE425 and PM390 alloy specimens were examined using scanning electron microscopy (SEM) to identify the fatigue crack initiation sites, following which quantitative measurements of these crack initiation sites were carried out using the image analyzer in order to make a correlation between the defect (porosity) that initiated the fatigue crack and the sample fatigue life.

### 4.5.3 Effect of surface porosity on fatigue life of AE425 alloy

The fatigue fracture surfaces for 34 alloy specimens (tested at two different temperatures, 150°C and 300°C) were examined to show the effect of porosity on the fatigue life of AE425 casting alloy. It was found that 31 of the 34 specimens (i.e. 91% of all specimens examined) fractured due to the effect of surface porosity acting as the main crack initiation site.

Figure 4.29 through Figure 4.32 show examples of the SEM images obtained from the fatigue fracture surfaces of AE425 alloy samples tested at two different temperatures. The nature of the surface porosity at the crack initiation site is observed to be of two types: a single surface pore from which the crack initiates, or a sponge-like area containing multiple pores in the form of a porous or spongy structure at the crack initiation site; this porous structure covers a large portion of the total bright area where the crack initiated and propagated. As before, the arrow refers to the crack initiation site (single surface pore or spongy structure) which created the fatigue crack. The reason for the spongy structure observed in these alloy samples is not understood.

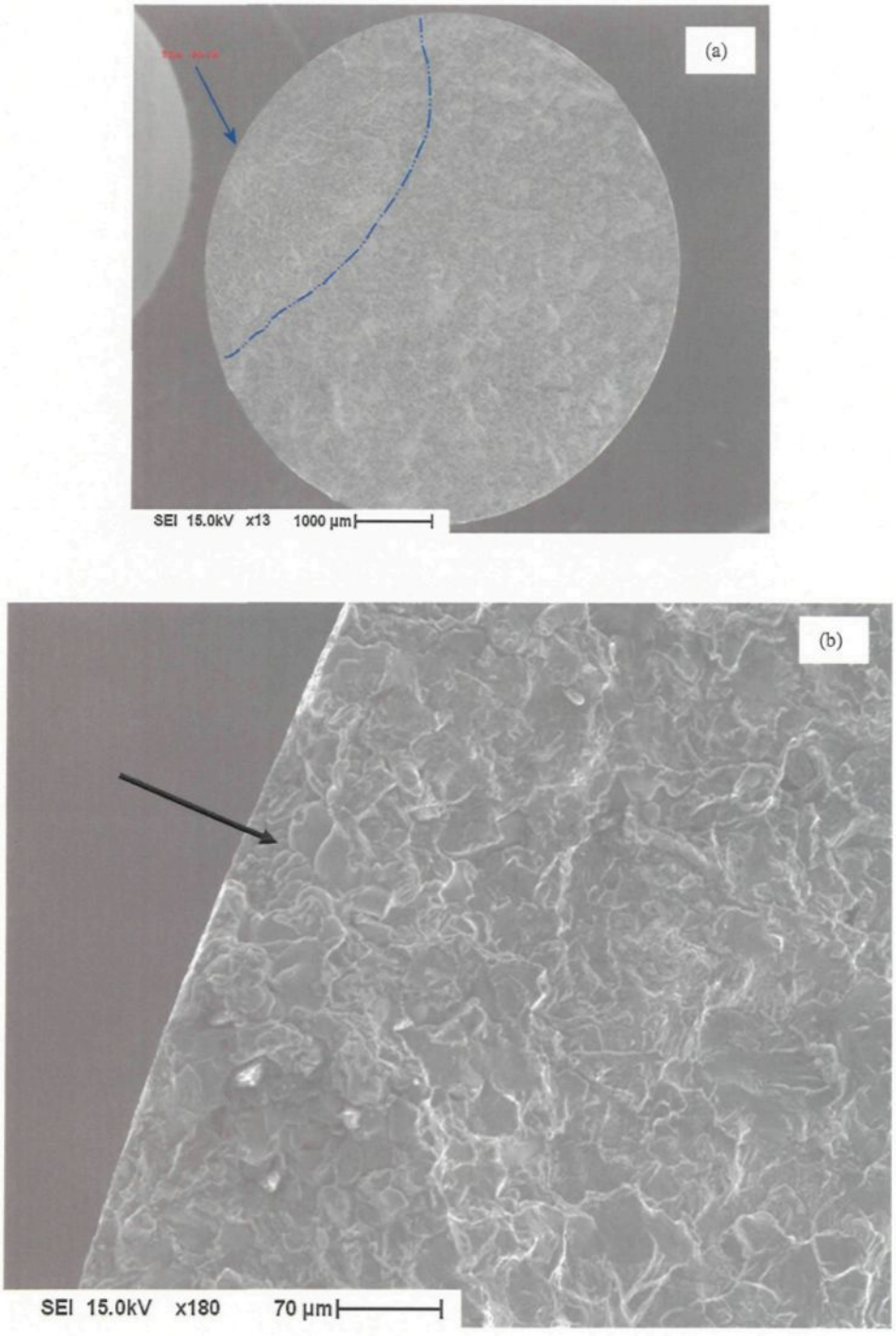


**Figure 4.29** SEM images of the fatigue fracture surface of an AE425 alloy sample taken (a) at low magnification, showing the bright area and the crack initiation site, and (b) at high magnification, showing a single pore acting as the crack initiation site (sample was tested at 150°C).

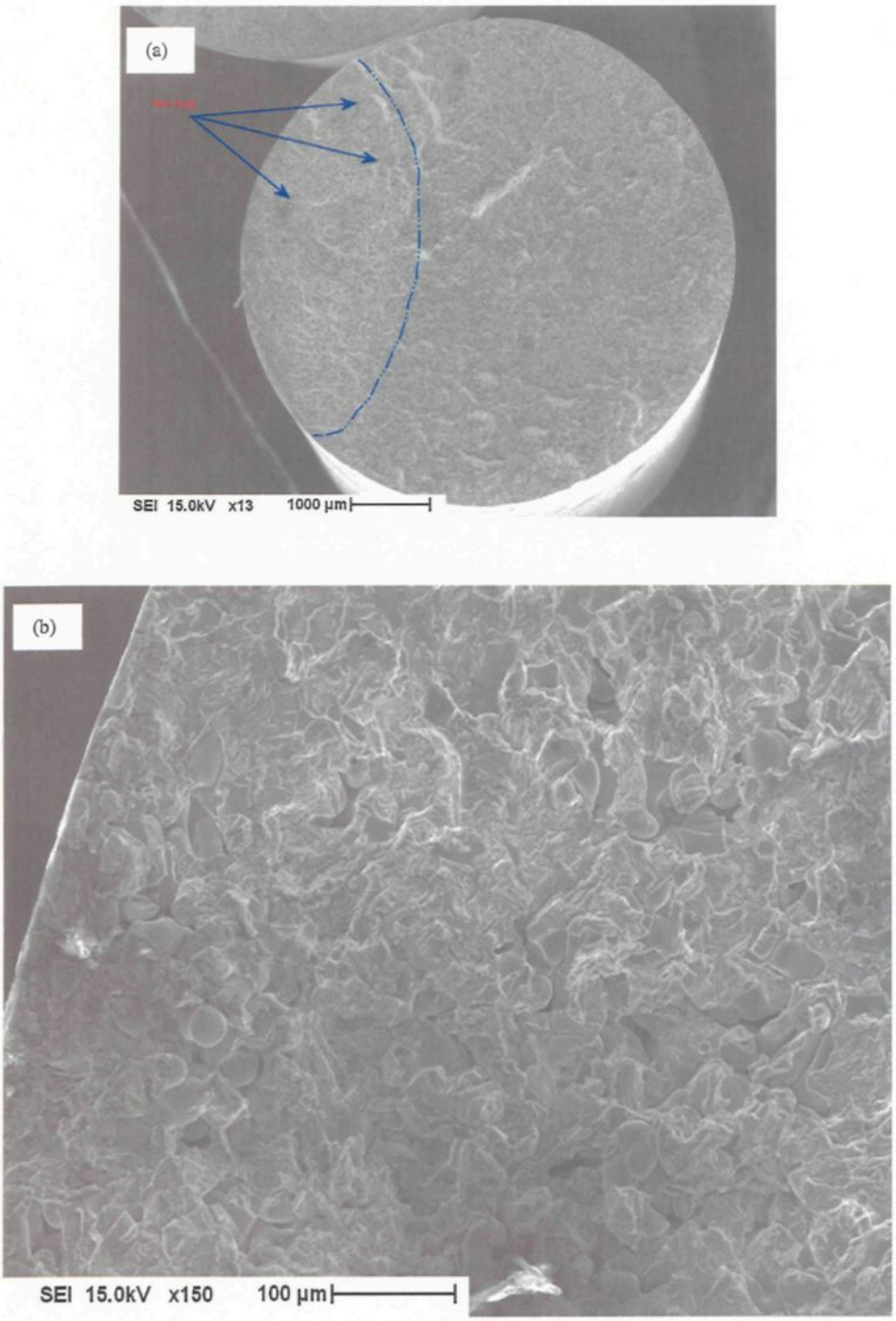


**Figure 4.30** SEM images of the fatigue fracture surface of an AE425 alloy sample taken (a) at low magnification, showing the bright area and the crack initiation site, and (b) at high magnification, showing a part of the spongy structure observed in this area (sample was tested at 150°C).

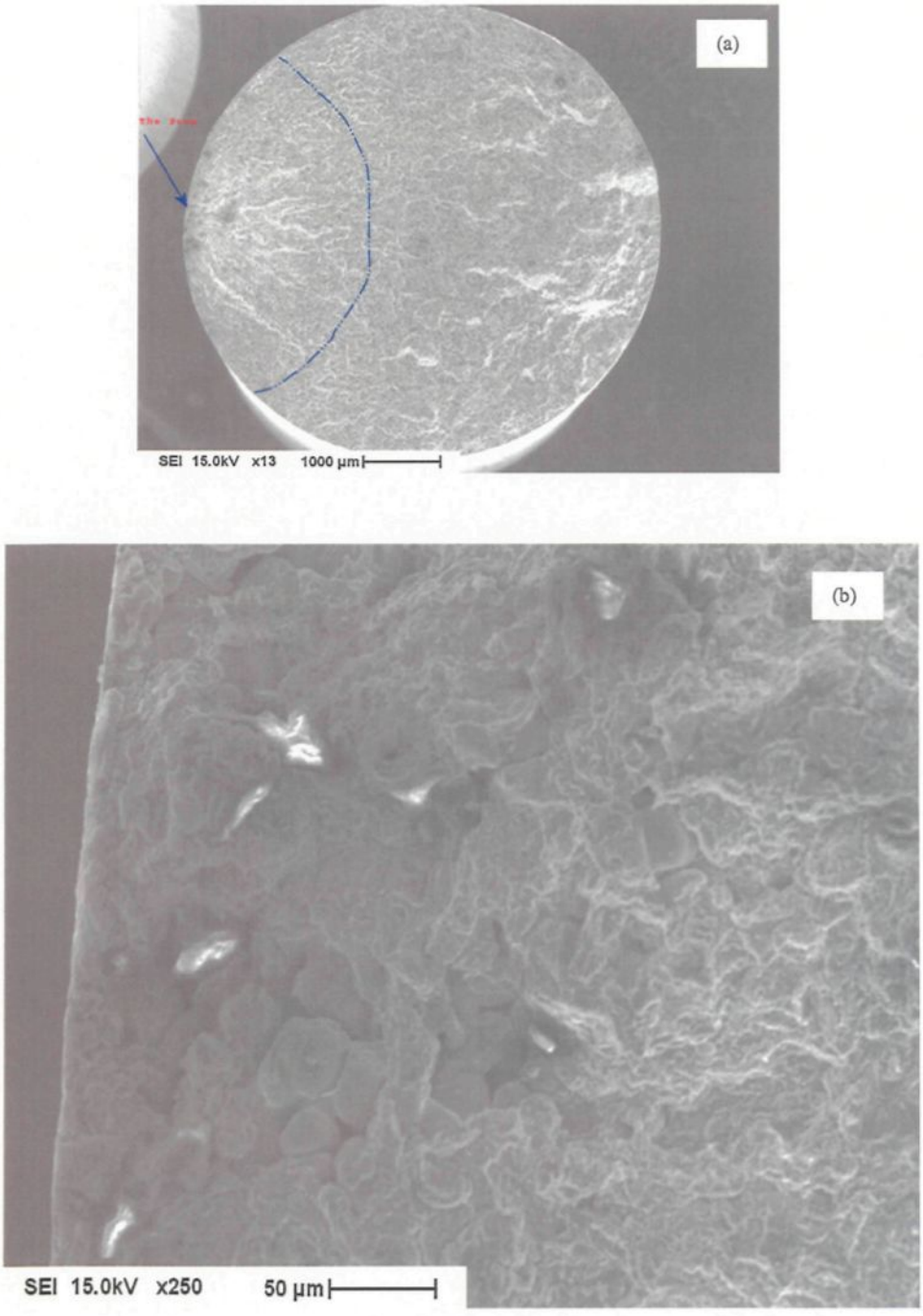


**Figure 4.31** SEM images of the fatigue fracture surface of an AE425 alloy sample taken (a) at low magnification, showing the bright area and the crack initiation site, and (b) at high magnification, showing the single pore acting as the crack initiation site (sample was tested at 300°C).

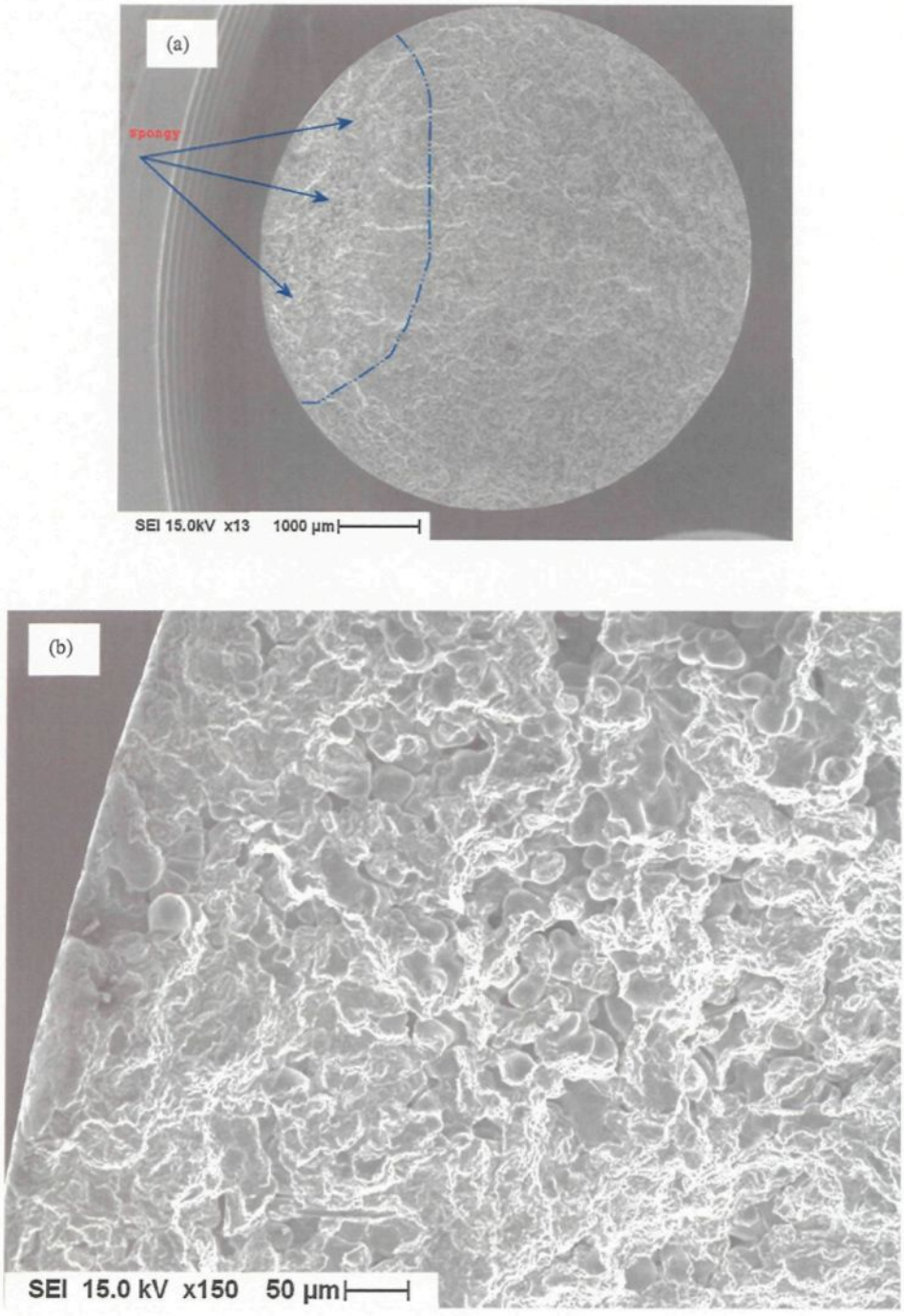


**Figure 4.32** SEM images of the fatigue fracture surface of an AE425 alloy sample taken (a) at low magnification, showing the bright area and the crack initiation site, and (b) at high magnification, showing a part of the spongy structure observed in this area (sample was tested at 300°C).

The fact that many individual pores exist is evidenced by the dendrites that can be seen clearly in these regions together with the rest of the fracture surface. Due to the difficulty in determining the exact pore size responsible for the crack initiation, measurements of the porous area using the SEM and image analysis techniques pose a lot of limitations. It is expected, therefore, that the measurements for the hypereutectic alloys will show some scatter. In view of this, the SEM technique must be re-evaluated similar to the case of 319 alloy to determine an alternate, more precise means of measuring the porosity in such samples.

However, as this is a very time consuming process, the measurements were carried out using the conventional process of quantification of the SEM images using image analysis. The results for AE425 alloy are shown in Figure 4.33 and Figure 4.34. The fatigue tests were carried out at two temperatures (150°C and 300°C), at a stress ratio R= -1, using a sinusoidal waveform, and under high cycle fatigue conditions. The stress applied ranged from 70 MPa to 100 MPa for the samples tested at 150°C, and from 36 MPa to 45 MPa for those tested at 300°C.

The scatter in the results obtained in such cases makes some difficulties to analyse these results according to the type of crack initiation observed and the test temperatures. The effect of surface porosity (either type) on the fatigue life is obvious: as the surface pore size increases, there is a marked decrease in the fatigue life, for the same reasons as those mentioned previously in section 4.3.1.

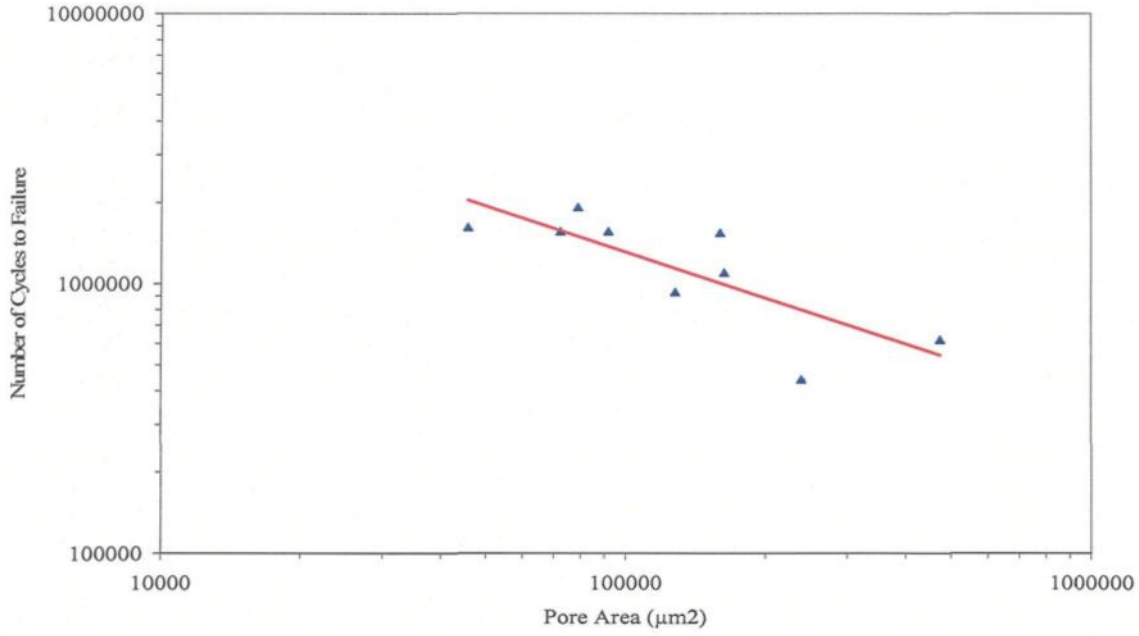


(a)

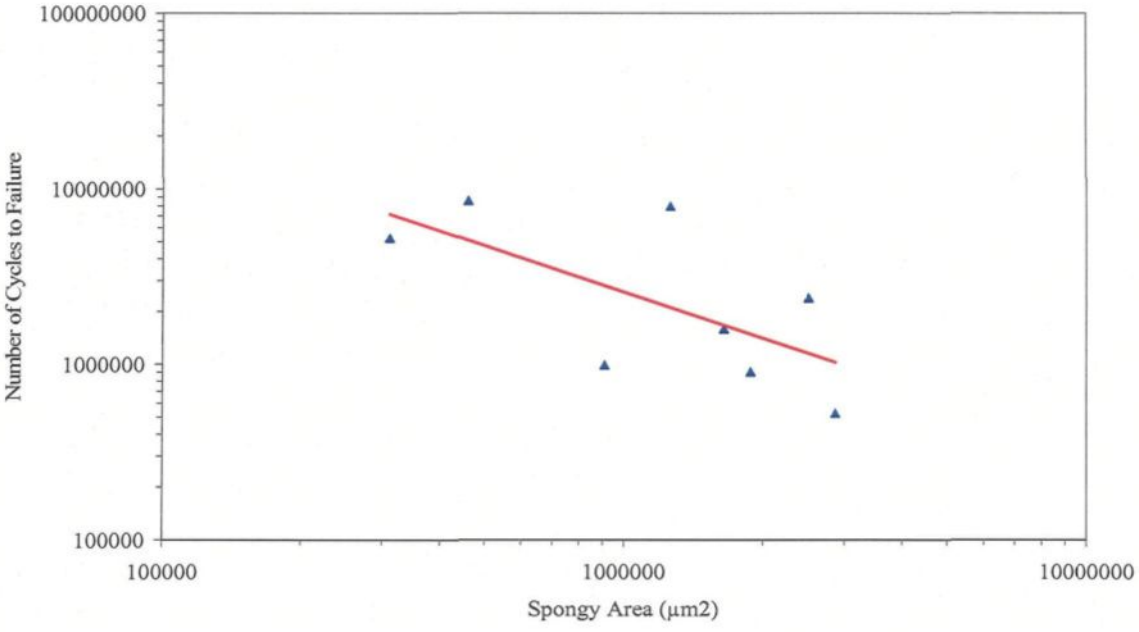


(b)

**Figure 4.33** Effect of (a) surface pore size and (b) surface spongy area on the fatigue life of AE425 alloy samples tested at 150°C.

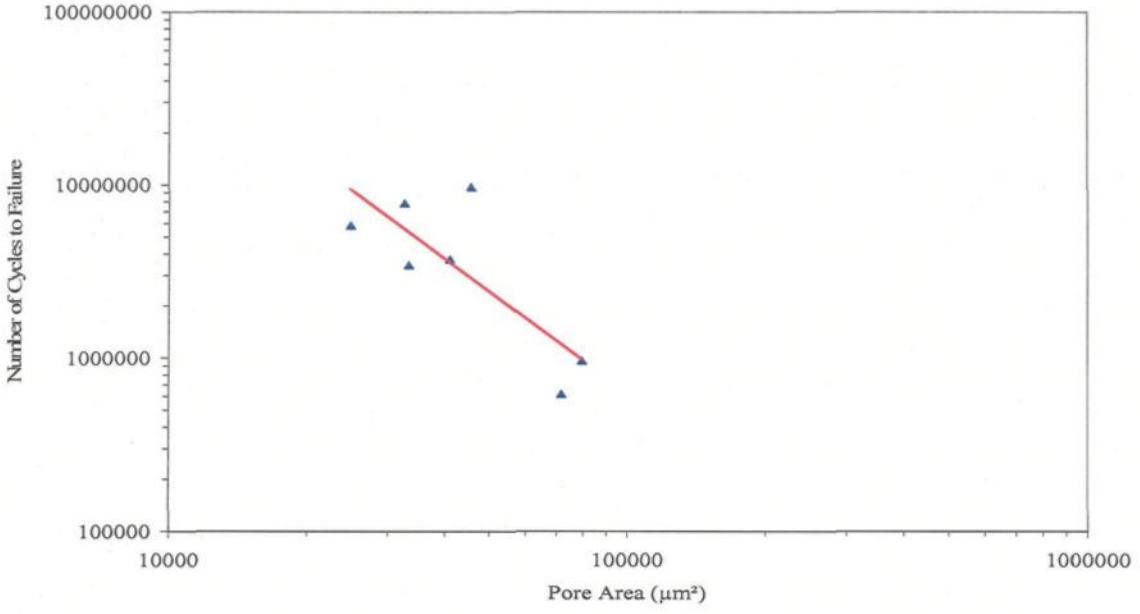


(c)

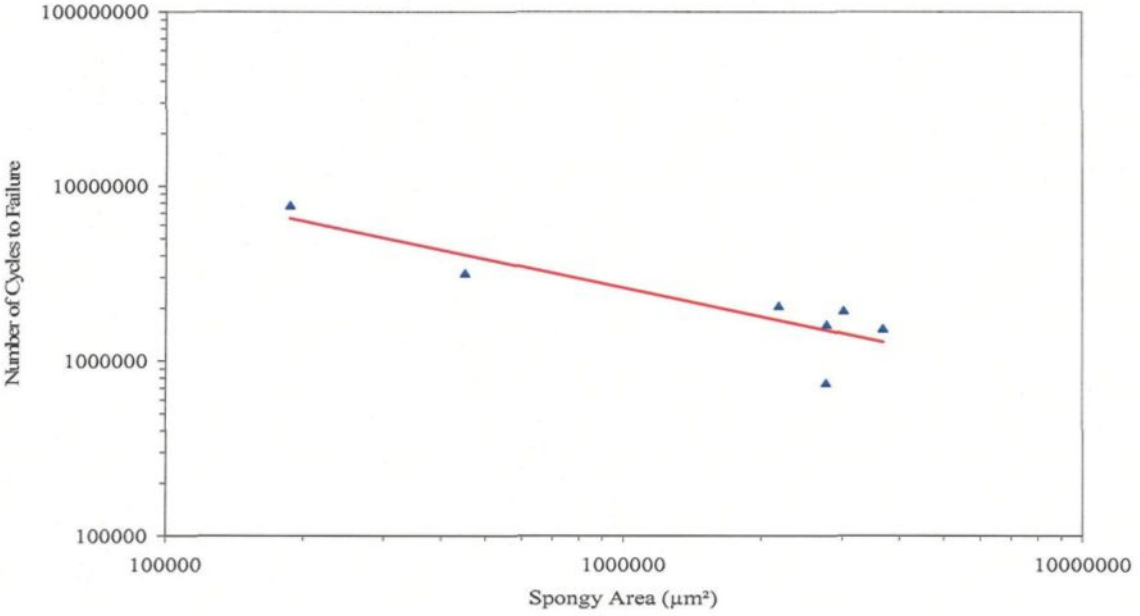


(d)

**Figure 4.34** Effect of (a) surface pore size and (b) surface spongy area on the fatigue life of AE425 alloy samples tested at 300°C.

### 4.5.4 Effect of surface porosity on fatigue life of PM390 alloy

The fatigue fracture surfaces of 29 specimens were examined to show the effect of porosity on the fatigue life of PM390 alloy. As in the case of the AE425 alloy, the tests were carried out at two temperatures, 150°C and 300°C. It was found that 25 of the 29 specimens (i.e. 86% of all the specimens examined) fractured due to the effect of porosity acting as the main crack initiation site.

Figure 4.35 and Figure 4.36 show examples of SEM images obtained from the fatigue fracture surface of two PM390 alloy samples tested at the two temperatures. The arrows point to the pore which initiated the fatigue crack.

Quantitative measurements of the surface porosity observed on the fatigue fracture surfaces of these PM390 alloy specimens were carried out using same procedures as those used for the AE425 alloy. The results for PM390 alloy are shown in Figure 4.37 through Figure 4.40. The fatigue tests were carried out at two temperatures (150°C and 300°C), at a stress ratio R= -1, using a sinusoidal waveform, and under high cycle fatigue conditions. The stress applied ranged from 69 MPa to 94 MPa for the samples tested at 150°C, and from 35 MPa to 41 MPa for those tested at 300°C.

The results obtained have been plotted together in Figure 4.37 and Figure 4.39, and separately in Figure 4.38 and Figure 4.40 for the different stress levels applied, showing that the fatigue life decreases with the increase in both the surface pore size and the stress amplitude.

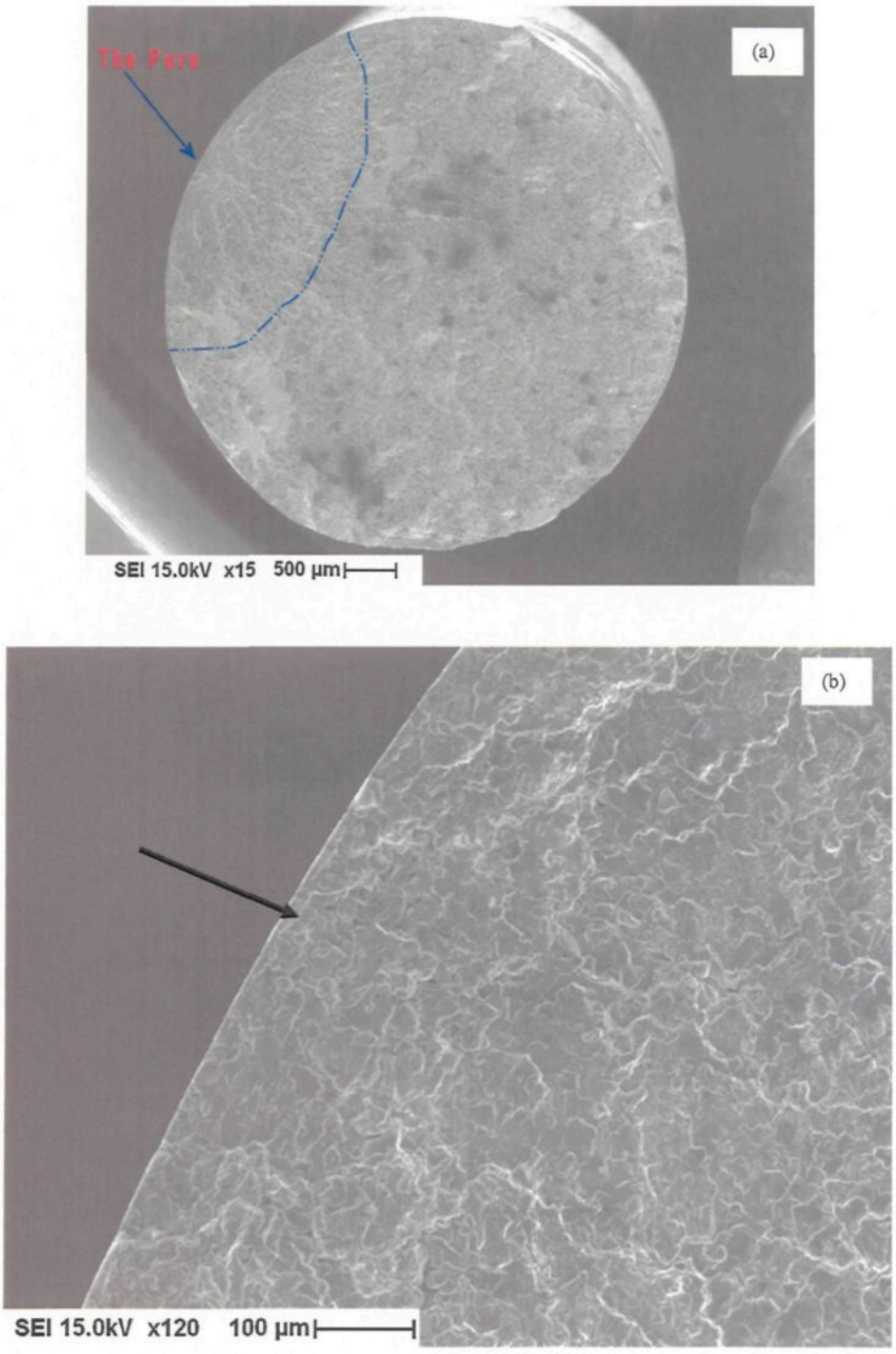


**Figure 4.35** SEM images of the fatigue fracture surface of a PM390 alloy sample taken (a) at low magnification, showing the bright area and the crack initiation site, and (b) at high magnification, showing the single pore acting as the crack initiation site (sample was tested at 150°C).

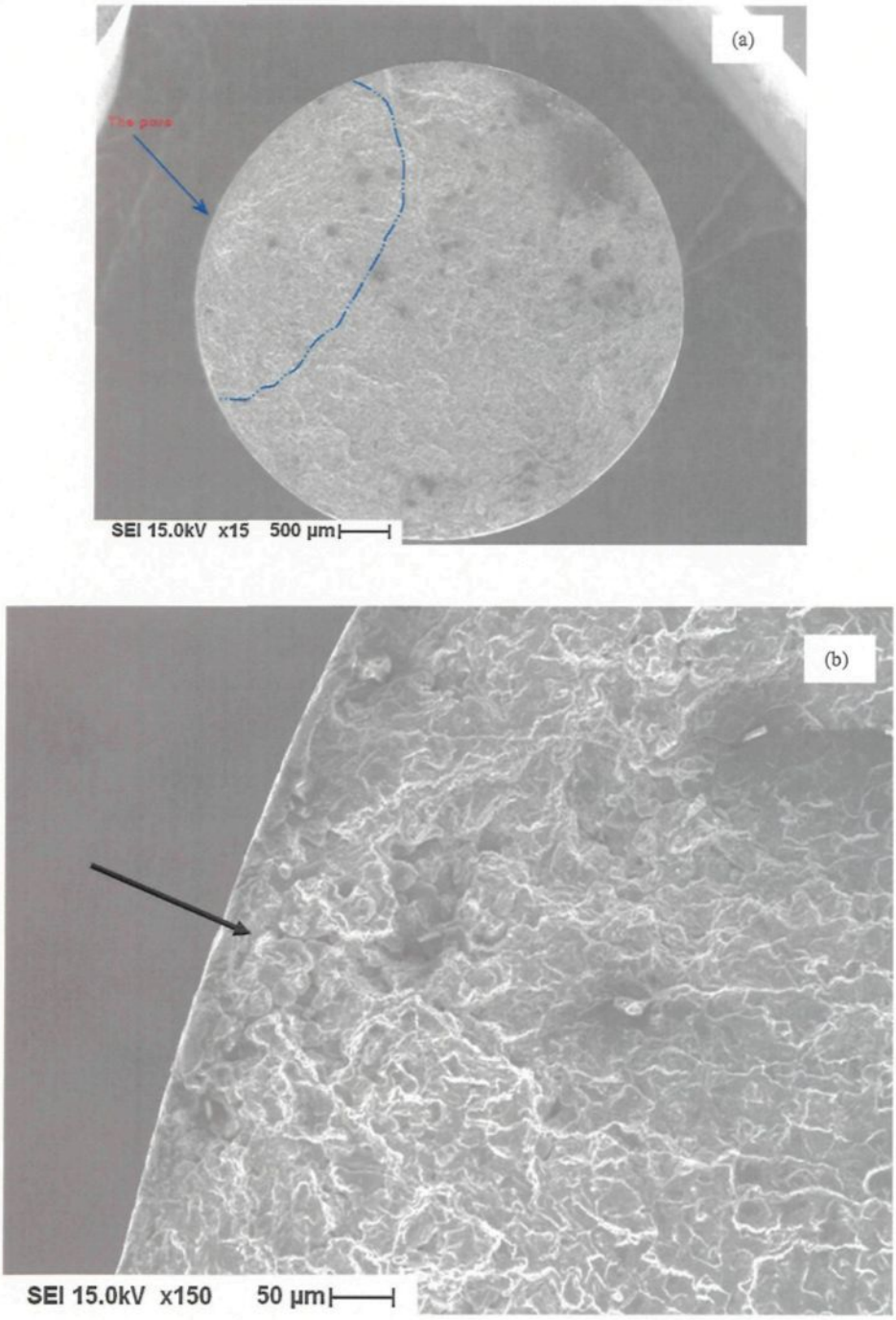


**Figure 4.36** SEM images of the fatigue fracture surface of a PM390 alloy sample taken (a) at low magnification, showing the bright area and the crack initiation site, and (b) at high magnification, showing the single pore acting as the crack initiation site (sample was tested at 300°C).

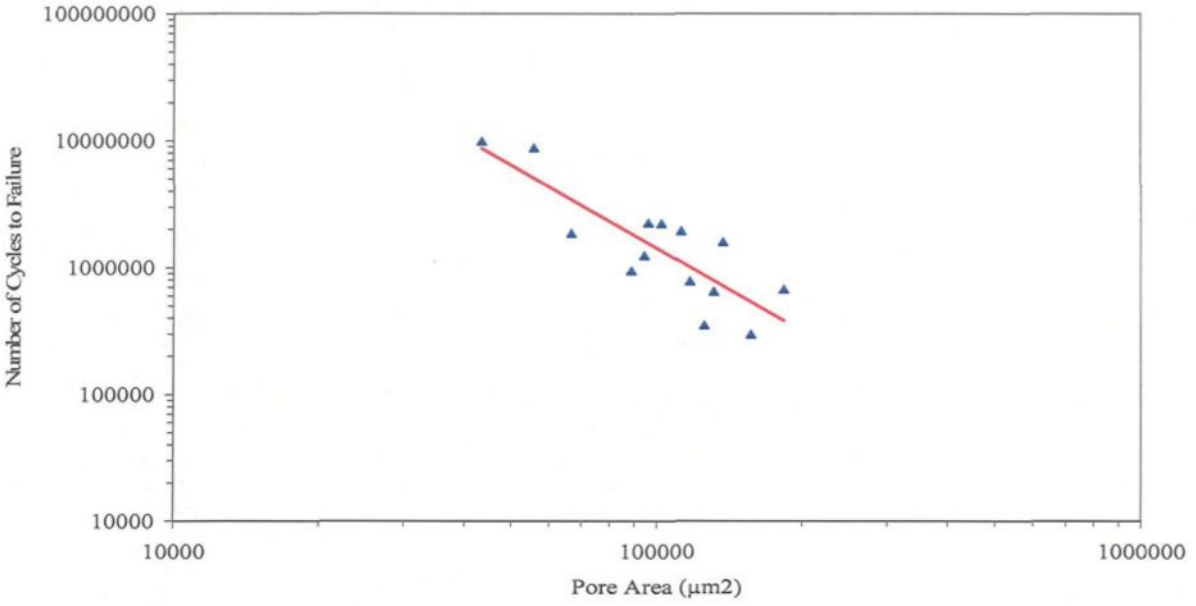


**Figure 4.37** Effect of pore size on the fatigue life of PM390 alloy samples tested at 150°C.

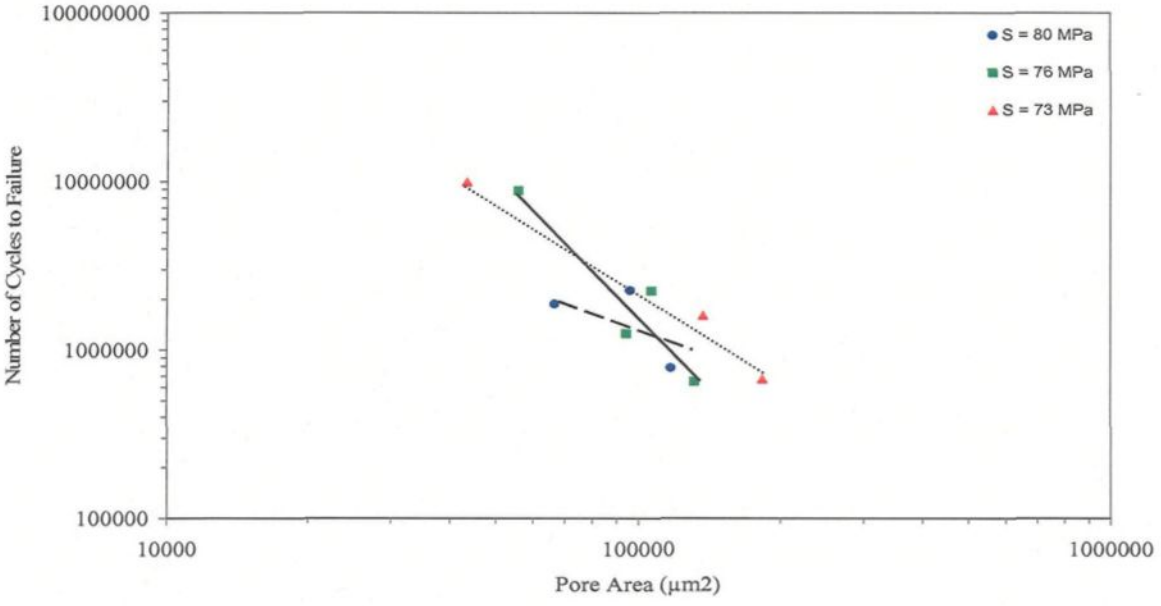


**Figure 4.38** Effect of pore size on the fatigue life of PM390 alloy samples tested at 150°C at different stress levels.

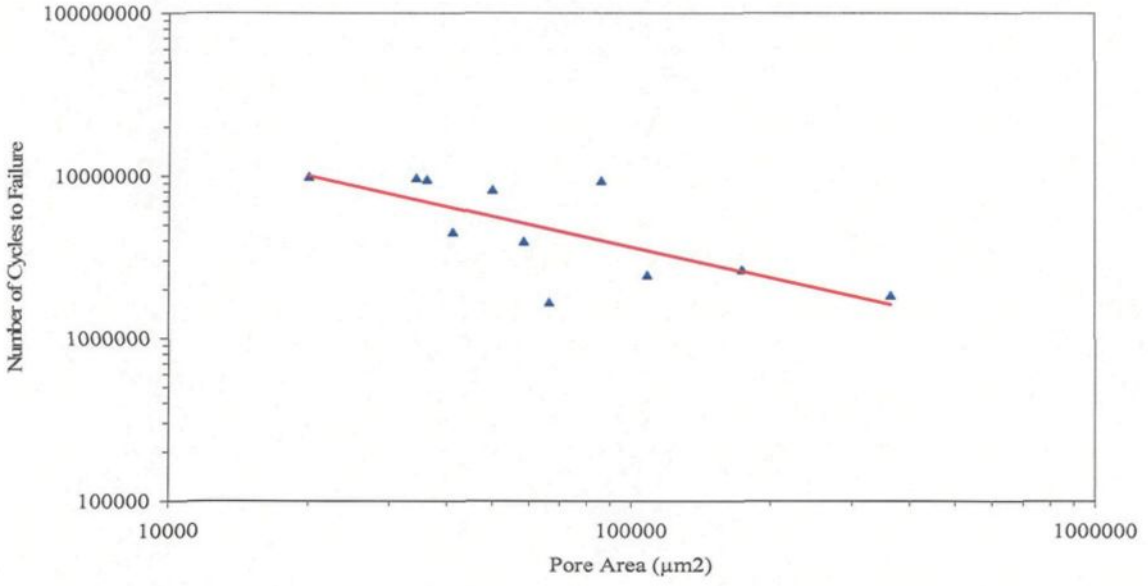


**Figure 4.39** Effect of surface pore size on the fatigue life of PM390 alloy samples tested at 300°C.

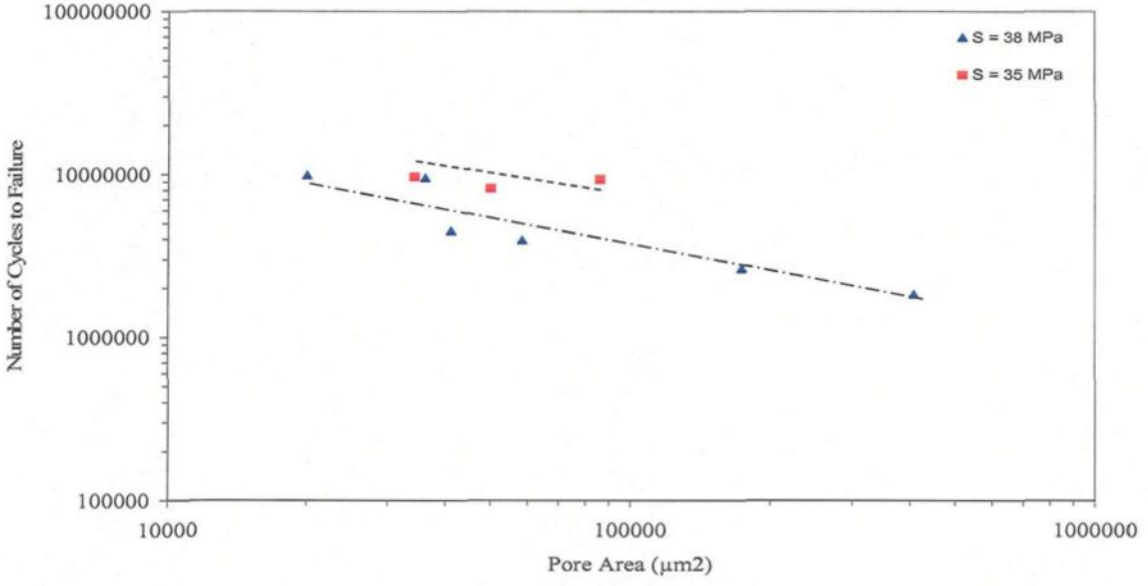


**Figure 4.40** Effect of surface pore size on the fatigue life of PM390 alloy samples tested at 300°C at different stress levels.

### 4.5.5 Effect of Si particles on the fatigue behavior of hypereutectic alloys

Primary silicon particles in hypereutectic Al-Si casting alloys influence their fatigue behavior. These particles are hard and brittle in nature, and act as favored sites for crack propagation. The crack is attracted towards them, increasing the crack growth rate. The damage and decohesion of primary silicon particles during cyclic loading results in facilitating the fatigue crack propagation and, as a consequence, lowers the fatigue life. Figure 4.41(a) and (b) shows examples of optical micrographs of the fatigue fracture surface typically obtained from the AE425 and PM390 samples, while Figure 4.41(c) shows an example of an optical micrograph taken from the matrix far from the fracture surface. The decohesion and damage of silicon particles at the fracture surface (circled regions) can be clearly seen, indicating that these particles contribute to the fatigue cracking, increasing the fatigue crack growth rate and shortening the fatigue life. In comparison, the primary silicon particles observed within the matrix (Figure 4.41(c)), and far from the fracture surface, are not affected.

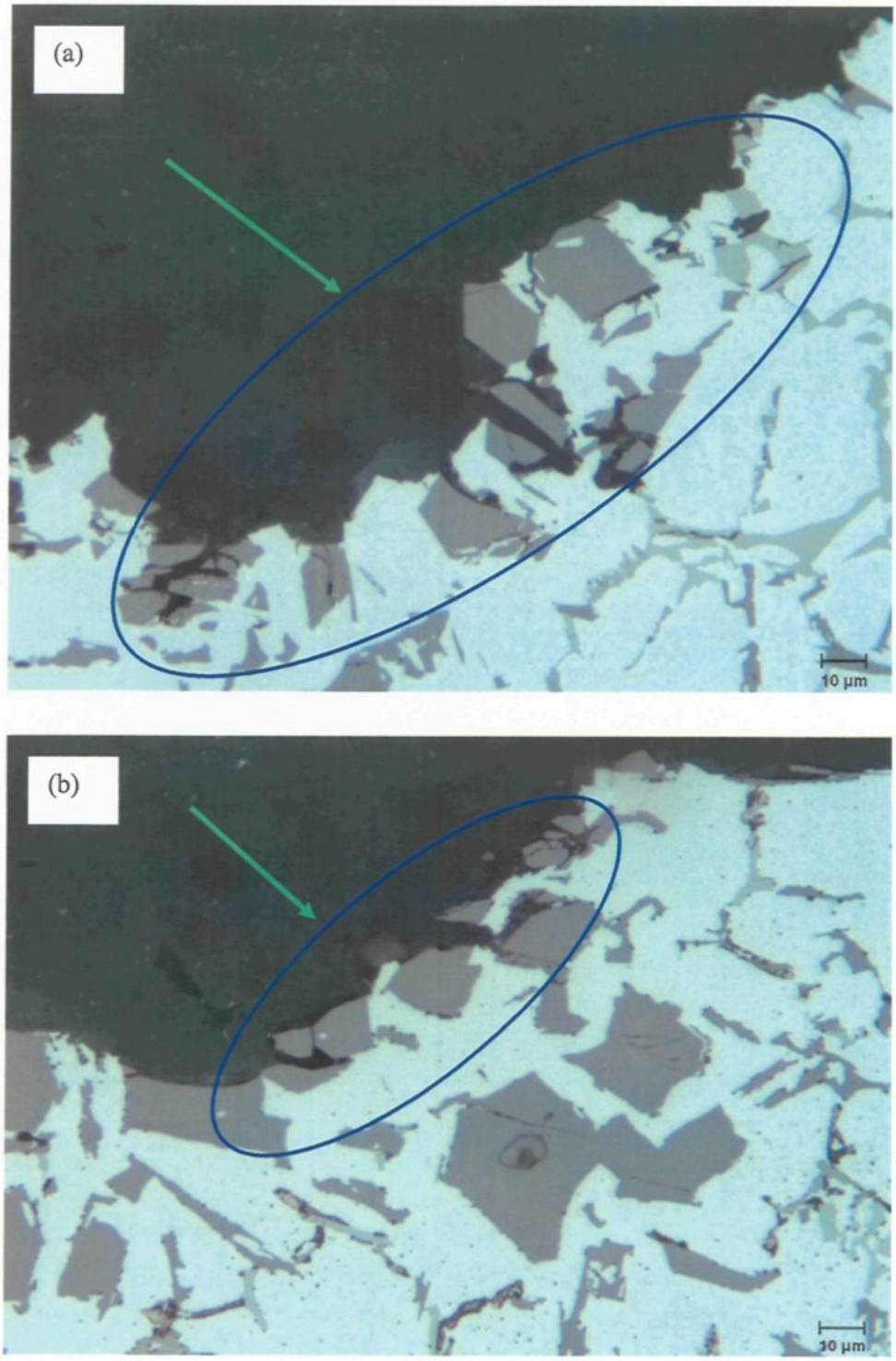


**Figure 4.41**

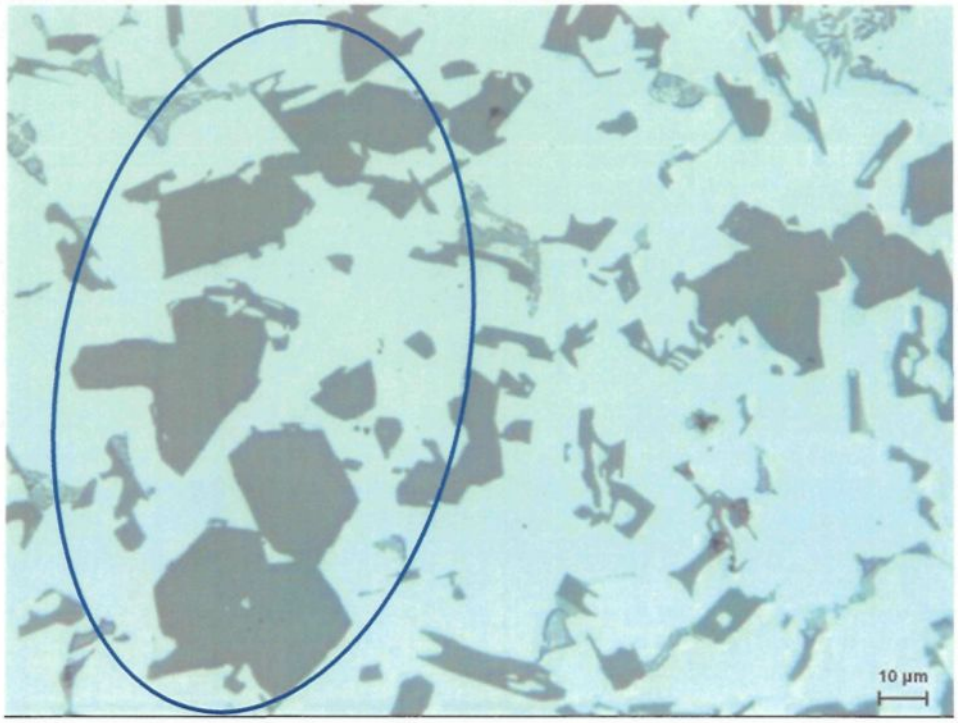


(c)

**Figure 4.41** Optical micrographs showing damage and decohesion of primary Si particles (a, b) on the fracture surface compared to the undamaged particles within the matrix (c), typically observed in AE425 and PM390 hypereutectic alloy samples.

# CHAPTER 5

# CONCLUSIONS

# CHAPTER 5

# CONCLUSIONS

The effect of surface porosity on the fatigue life of LP PM319-F, A356-T6, C354-T6, AE425 and PM390 Al-Si casting alloys was investigated in the present work. From an analysis of the results obtained, the following can be concluded.

1. Surface porosity is the most important casting defect affecting the fatigue life, as it is found to be the most favored site for fatigue crack initiation: from among the 157 specimens tested, 129 specimens (82%) fatigue fractured due to this effect.
2. The sample fatigue life decreases as the surface pore size increases (and vice versa) where, due to the increase in the stress concentration associated with the increase in the surface pore size, the driving force for fatigue crack initiation and propagation is also increased.
3. In the absence of surface porosity, other casting defects such as oxide films near to the surface can be responsible for fatigue crack initiation. In the present study, 3% of all tested samples fractured on account of oxide films acting as the main crack initiation site.
4. Apart from casting defects (porosity and oxide films), some microstructural features can also act as crack initiation sites. In the present case, slip bands were mainly

responsible, where 3% of all tested samples fractured on account of slip bands acting as the main crack initiation site.

5. Fatigue crack initiation always starts at the free surface of the sample, regardless the type of defect involved (porosity, oxide films or slip bands). The maximum stress is found at this point and the stress gradient from the free surface toward the centre of the sample (sample interior) favors fatigue crack propagation. It is impossible for the fatigue crack to propagate in the opposite direction i.e., from a low stress region (sample interior) to a high stress region (sample free surface).
6. While run-out samples are not sound since they contain porosity, however, the occurrence of this porosity within the interior of the samples has much less influence on crack initiation than if the porosity were located on the sample surface, which is why they do not fracture even after a large number of cycles ($>10^7$).
7. The SEM technique can be applied with great accuracy for measurements of single pores responsible for fatigue crack initiation. When the crack initiation area contains multiple pores (the case of LP PM319-F alloy) or a spongy porous structure (the case of AE425 alloy), these measurements are not enough to determine the exact fatigue crack initiation site, and the technique must be re-evaluated to provide greater accuracy of the results.
8. When the crack initiation area contains multiple pores, the actual fatigue crack initiation site can be determined employing optical microscopy and a longitudinal section of the fractured specimen. However, this is a time consuming process.

9. The HIPping process has a positive effect on the fatigue strength of Al-Si casting alloys as it eliminates the large surface porosity and results in increasing the sample fatigue life. In the absence of surface porosity, other crack initiation sites such as oxide films and slip bands which have less effect on fatigue strength compared with surface porosity become operative.
10. The primary silicon particles in hypereutectic alloys contribute to the fatigue behavior in that the decohesion and damage of these particles under cyclic loading weakens the structure and accelerates the fatigue fracture.
11. Microstructural constituents/features such as the eutectic Si particle characteristics, the secondary dendrite arm spacing, intermetallics, and grain size can influence the fatigue life if they are responsible for the fatigue crack propagation.

# RECOMMENDATIONS FOR FUTURE WORK

Based on the results obtained in the present study on the effect of casting defects in relation to the fatigue life of Al-Si type casting alloys, the following may be recommended for future work.

1. The crack initiation area in hypereutectic Al-Si alloys should be investigated in detail to determine the nature of the spongy porous structure normally associated with the crack initiation site in these alloys. Such an analysis would help in determining a suitable technique for quantitative analysis of crack initiation sites consisting of multiple pores or other features such as slip bands, etc.
2. Apart from the different casting techniques employed for producing the castings/samples used in the present study, the effect of other factors such as the melt treatments applied (degassing, grain refining and modification), the intermetallics and other second phase constituents present in the structure, as well as the heat treatment regime employed on porosity formation would provide further insight into the fatigue properties.

# REFERENCES

# REFERENCES


1. *ASM Handbook Vol. 2 Properties and Selection: Nonferrous Alloys and Special-Purpose Materials,* ASM International, The Materials Information Society, U.S.A., 1990.

2. O. Madelaine-Dupuich and J. Stolarz, "Fatigue of Eutectic Al-Si Alloys", *Materials Science Forum*, 1996, Vol. 217-222, pp. 1343-1348.

3. J.E. Gruzleski and B.M. Closset, *The Treatment of Liquid Aluminum-Silicon Alloys*, American Foundarymen's Society, Inc., Des Plaines, IL, U.S.A., 1990.

4. Z. Ma, "Effect of Fe-Intermetallics and Porosity on Tensile and Impact Properties of Al-Si-Cu and Al-Si-Mg Cast Alloys," Ph.D Thesis, Université du Québec à Chicoutimi (UQAC), Qc, Canada, August, 2002.

5. J.R. Davis, *Aluminum and Aluminum Alloys*, ASM Specialty Handbook, ASM International, Materials Park, OH, U.S.A., 1993.

6. G.L. Armstrong, "Alloy Selection for Automotive Aluminum Castings," *SAE Technical Paper*, No. 780249, Society of Automotive Engineers, 1987.

7. F. Palazzo, "The Future in the Automotive Industry", *Allumino,* Vol. 46, No. 9, 1977, pp. 323-334.

8. W.S. Miller, "Recent Development in Aluminum Alloys for the Automotive Industry", *Materials Science and Engineering A*, Vol. A280, 2000, pp. 37-49.

9. J.G. Kaufman, E.L. Rooy, *Aluminum Alloy Castings Properties, Processing, and Applications*, ASM International, Materials Park, Ohio, U.S.A. 2004.

10. L. Bäckerud, G. Chai, and J. Tamminen, *Solidification Characteristics of Aluminum Alloys, Vol. 2 Foundry Alloys*, AFS/Skanalumimium, Des Plaines, IL, U.S.A, 1990.

11. J.E. Hatch, *Aluminum: Properties and Physical Metallurgy*, American Society for Metals, Metals Park, OH, U.S.A. 1984.

12. J.M. Boileau and J.E. Allison, "The Effect of Porosity Size on the Fatigue Properties in a Cast 319 Aluminum Alloy", *SAE Transactions,* Vol. 110, 2001, pp. 648-659.

13. J.M. Kim, H.W. Kwon, D.G. Kim and C.R. Loper, Jr., "Porosity Formation in Relation to the Feeding Behavior of Al-Si Alloys". *AFS Transactions*, Vol 105, 1997, pp. 825-831.

14. G.K. Sigworth, C. Wang, H. Huang and T. Berry, "Porosity Formation in Modified and Unmodified Al-Si Alloy Castings", *AFS Transactions,* Vol. 102, 1994, pp. 245-260.

15. K. Kubo and R.D. Pehlke, "Porosity Formation in Solidifying Castings", *AFS Transactions,* Vol. 94, 1986, pp. 753-756.

16. N. Roy, A.M. Samuel and F.H. Samuel, "Porosity Formation in Al-9Wt Pct Si-3 Wt Pct Cu Alloy System: Metallographic Observations", *Metallurgical and Materials Transactions A*, Vol. 27A, 1996, pp. 415-429.

17. Y.J. Huang and S.Z. Lu, "A Measurement of the Porosity in Aluminum Cast Alloys Using Fractal Analysis", *Proc. 2nd Int. Aluminum Casting Technology Symposium,* 2002, Columbus, OH, ASM International, 2002, 4p.

18. N. Roy, L. Zhang, P.R. Louchez and F.H. Samuel, "Porosity Formation in Al-9 wt % Si-3 wt% Cu-X Alloy System: Measurements of Porosity," *Journal of Materials Science*, Vol. 31(5), 1996, pp. 1243-1254.

19. A.M. Samuel and F.H. Samuel, "Porosity Factor in Quality Aluminum Castings", *AFS Transactions*, Vol. 100, 1992, pp. 657-666.

20. H. Shahani, "Effect of Hydrogen on the Shrinkage Porosity of Aluminum Copper and Aluminum Silicon Alloys", *Scandinavian Journal of Metallurgy*, Vol. 14, 1985, pp. 306-312.

21. J. Campbell, *The Solidification of Metals*, Iron and Steel Institute, Publication 110, London, 1976, 18 pp.

22. M. Djurdjevic, R. Hasenbush and J. Sokolowski, "Assessment of The Hydrogen Level in 319 Aluminum Alloy Melts Using the Thermal Analysis Technique", *Light Metals 2002*, The Minerals, Metals & Materials Society, Warrendale, PA, 2002, pp. 889-896.

23. A Nouruzi-Khorasani, "Gas Porosity in Aluminum Silicon Alloys," *Metal Castings and Surface Finishing,* Vol. 42, Nos. 9-10, 1996, pp. 34-39.

24. Elwin L. Rooy, "Mechanisms of Porosity Formation in Aluminum," *Modern Casting*, 1992, pp. 34-36.

25. Q.T. Fang and P.N. Anyalebechi, "Effects of Solidification Conditions on Hydrogen Porosity Formation in Aluminum Alloy Castings," *Light Metals 1988,* The Minerals, Metals & Materials Society, Warrendale, PA, 1988, pp. 477-486.

26. P.D. Lee and S. Sridhar, "Effect of Strontium Modifiers on Porosity in Cast Al-Si Alloys," The Minerals, Metals & Materials Society, Seattle, 2002, pp. 555-565.

27. Q.T Fang and D.A. Granger, "Porosity Formation in Modified and Unmodified A356 Alloy Castings," *AFS Transactions*, Vol. 97, 1989, pp. 989-1000.

28. P.D. Lee and S. Sridhar, "Direct Observation of the Effect of Strontium on Porosity Formation During the Solidification of Aluminum-Silicon Alloys," *International Journal of Cast Metals Research*, Vol. 13, No. 4, 2000, pp. 185-198.

29. D. Argo and J.E. Gruzleski, "Porosity in Modified Aluminum Alloy Castings," *AFS Transactions*, Vol. 96, 1988, pp. 65-74.

30. D. Emadi, J.E. Gruzleski and J.M. Toguri, "The Effect of Na and Sr Modification on Surface Tension and Volumetric Shrinkage of A356 Alloy and Their Influence on Porosity Formation," *Metallurgical Transactions B*, Vol. 24B, 1993, pp. 1055-1063.

31. X. Bian, Z. Zhang and X. Liu, "Effect of Strontium Modification on Hydrogen Content and Porosity Shape of Al-Si Alloys," *Materials Science Forum*, Vol. 331-337, 2000, pp. 361-366.

32. L. Liu, A.M. Samuel, F.H. Samuel, H. Doty and S. Valtierra, "Influence of Oxides on Porosity Formation in Sr-Treated Al-Si Casting Alloys," *Journal of Materials Science*, Vol. 38, 2003, pp. 1255-1267.

33. S. El Hadad, "Effect of Trace Elements on the Microstructure and Porosity Formation in 319 Type Al-Si-Cu Alloys," M. Eng. Thesis, UQAC, Chicoutimi, QC, Canada, 2003.

34. M. Dash and M. Makhlouf, "Effect of Alloying Elements on the Feeding Characteristics of Aluminum-Silicon Casting Alloys," *Journal of Light Metals,* Vol. 1, 2001, pp. 251-265.

35. J.A. Taylor, G. B. Schaffer and D.H. StJohn, "The Role of Iron in the Formation of Porosity in Al-Si-Cu-Based Casting Alloys: Part I. Initial Experimental Observations," *Metallurgical and Materials Transactions A*, 1999, Vol. 30A, pp. 1643-1650.

36. A.K. Gupta, B.K. Saxena, S.N. Tiwari and S.L. Malhotra, "Review: Pore Formation in Cast Metals and Alloys," *Journal of Materials Science*, Vol. 27, 1992, pp. 853-862.

37. H. Iwahori, K. Yonekura, Y. Yamamoto and M. Nakamura, "Occurring Behavior of Porosity and Feeding Capabilities of Sodium and Strontium-Modified Al-Si Alloys," *AFS Transactions*, Vol. 98, 1990, pp. 167-173.

38. C. Tian, J. Law, J. Van de Touw, M. Murray, J-Y. Yao, D. Graham and D. StJohn, "Effect of Melt Cleanliness on the Formation of Porosity Defects in Automotive High Pressure Die Castings," *Journal of Materials Processing Technology*, Vol. 122, 2002, pp. 82-93.

39. G. Laslaz and P. Laty, "Gas Porosity and Metal Cleanliness in Aluminum Casting Alloys," *AFS Transactions*, Vol. 99, 1991, pp. 83-90.

40. D.R. Irani and V. Kondic, "Casting and Mold Design Effects on Shrinkage Porosity of Light Alloys," *AFS Transactions*, Vol. 77, 1969, pp. 208-211.

41. J.T. Berry, R.P. Taylor and R.A. Overfelt, "Porosity Patterns in A356 Bar and Plate Castings and Their Relation to Riser Design," *AFS Transactions*, Vol. 105, 1997, pp. 465-471.

42. G.K. Sigworth and C.H. Caceres, "Porosity Formation in Aluminum Alloy Castings Under Quasi-Directional Solidification," *International Journal of Cast Metals Research*, Vol. 9, 1997, pp. 331-336.

43. George E. Dieter, *Mechanical Metallurgy*, Second Edition, Metallurgy and Metallurgical Engineering Series, McGraw-Hill, New York, 1976.

44. S.R. Lampman, *Fatigue and Fracture*, ASM International, The Materials Information Society, Materials Park, OH, U.S.A, 1996.

45. R.I. Stephens, A Fatemi, R.R. Stephens and H.O. Fuchs, *Metal Fatigue in Engineering*, Second Edition, John Wiley & Sons, Inc., New York, 2001.

46. A. Wickberg, G. Gustafsson and L.-E. Larsson, "Microstructure Effects on the Fatigue Properties of a Cast Al7SiMg Alloy," *SAE Transactions*, Vol. 93, 1984, pp. 728-735.

47. W.T. Donlon, C. Paige, C.J. Morris and J.E. Allison, "The Effect of Casting Defects and Microstructure on Mechanical Properties of Die Cast AM50 Magnesium and 356 Aluminum," *Aluminum and Magnesium for Automotive Applications,* J.D. Bryan (Ed.), The Minerals, Metals & Materials Society, Warrendale, PA, 1996, pp. 17-27.

48. P.C. Inguanti, "Cast aluminum fatigue property/microstructure relationships," *Proc. of the 17th National SAMPE Technical Conference,* SAMPE, Covina, CA, U.S.A., 1985, pp. 61-72.

49. S.E. Stanzl-Tschegg, H.R. Mayer, A. Beste and S. Kroll, "Fatigue and Fatigue Crack Propagation in AlSi7Mg Cast Alloys Under in-Service Loading Conditions," *International Journal of Fatigue*, Vol. 17, No. 2, 1995, pp. 149-155.

50. C.M. Sonsino and J. Ziese, "Fatigue Strength and Applications of Cast Aluminum Alloys with Different Degrees of Porosity", *International Journal of Fatigue*, Vol. 15, No. 2, 1993, pp. 75-84.

51. M.J. Couper, A.E. Neeson and J.R. Griffiths, "Casting Defects and the Fatigue Behavior of an Aluminum Casting Alloy," *Fatigue & Fracture of Engineering Materials & Structures*, Vol. 13, No. 3, 1990, pp.213-227.

52. H. Suzuki and T. Kunio, "Influence of Porous Defect on Scatter of Fatigue Strength of Aluminum Casting Alloy, AC4B (JIS)," *Proc. Int. Conf. on Role of Fracture Mechanics in Modern Technology*, 2-6 June 1986, Fukuoka, Japan, 1987, pp. 225-232.

53. J.C. Ting and F.V. Lawrence, Jr., "Modeling the Long Life Fatigue Behavior of a Cast Aluminum Alloy," *Fatigue & Fracture of Engineering Materials & Structures*, Vol.16, No. 6, 1993, pp. 631-647.

54. R.B. Gundlach, B.Ross, A. Hetke, S. Valtierra and J.F. Mojica, "Thermal Fatigue Resistance of Hypoeutectic Aluminum-Silicon Casting Alloys", *AFS Transactions* Vol.102, 1994, pp. 205-223.

55. H. Mayer, M. Papakyriacou, B. Zettl and S.E. Stanzl-Tschegg, "Influence of Porosity on the Fatigue Limit of Die Cast Magnesium and Aluminum Alloys", *International Journal of Fatigue,* Vol. 25, 2003, pp. 245-256.

56. J-Y. Buffière, S. Savelli, P.H. Jouneau, E. Maire and R. Fougères, "Experimental Study of Porosity and Its Relation to Fatigue Mechanisms of Model Al-Si7-Mg0.3 Cast Al Alloys," *Materials Science and Engineering A,* Vol. 319, 2001, pp.115-126.

57. M. Avalle, G. Belingardi, M.P. Cavatorta and R. Doglione, "Casting Defects and Fatigue Strength of a Die Cast Aluminum Alloy: A Comparison between Standard Specimens and Production Components," *International Journal of Fatigue,* Vol. 24, 2002, pp.1-9.

58. Q.G. Wang, D. Apelian and D.A. Lados, "Fatigue Behavior of A356-T6 Aluminum Cast Alloys. Part I. Effect of Casting Defects," *Journal of Light Metals,* Vol. 1, 2001, pp. 73-84.

59. Q.G. Wang, P.N. Crepeau, J.R. Griffiths and C.J. Davidson, "The Effect of Oxide Films and Porosity on Fatigue of Cast Aluminum Alloys," *Shape Casting: The John Campbell Symposium*, M. Tiryakioglu and P.N. Crepeau (Ed.), *The Minerals, Metals, & Materials Society*, Warrendale, PA, 2005, pp. 205-214.

60. Q.G. Wang, P.N. Crepeau, D. Gloria and S. Valtierra, "Improvement of Fatigue Strenght in Aluminum Castings," *Proc. of the 2nd Int. Aluminum Casting Technology Symposium,* Columbus, OH, ASM International, 2002, pp. 209-218.

61. J.M. Boileau and J.E. Allison, "The Effect of Solidification Time and Heat Treatment on the Fatigue Properties of a Cast 319 Aluminum Alloy," *Metallurgical and Materials Transactions A*, Vol. 34A, 2003, pp. 1807-1820.

62. J.M. Boileau, J.W. Zindel and J.E. Allison, "The Effect of Solidification Time on the Mechanical Properties in a Cast A356-T6 Aluminum Alloy," SAE Paper #970019, SAE, Warrendale, PA, 1997.

63. M.H. Lee, J.J. Kim, K.H. Kim, N.J. Kim, S. Lee and E.W. Lee, "Effects of HIPping on High-Cycle Fatigue Properties of Investment Cast A356 Aluminum Alloys," *Materials Science and Engineering A*, Vol. 340, 2003, pp. 123-129.

64. J.A. Odegard and K. Pedersen, "Fatigue Properties of an A356 (AlSi7Mg) Aluminum Alloy for Automotive Applications - Fatigue Life Prediction," *Proc. of Conf. of Metal Matrix Composites*, Detroit, MI, U.S.A., 28 Feb. – 3 Mar., 1994, pp. 25-35.

65. G.O. Rading, J. Li and J.T. Berry, "Fatigue Crack Growth in Cast Al-Cu Alloy A206 With Different Levels of Porosity," *AFS Transactions*, Vol. 102, 1994, pp. 57-61.

66. J.F. Major, "Porosity Control and Fatigue Behavior in A356-T61 Aluminum Alloy," *AFS Transactions*, Vol. 105, 1997, pp. 901-906.

67. S. Savelli, J-Y Buffière, E. Maire and R. Fougères, "Characterization by Synchrotron X-Ray Microtomography of Internal Microstructural Features and Their Detrimental Effects With Respect to the Fatigue Properties in an Aluminum Cast Alloy," *Proc. of ICAA-6: 6th Int. Conf. on Aluminum Alloys,* Toyohashi, Japan, 5-10 July, 1998, pp. 571-576.

68. B. Skallerud, T. Iveland and G. Härkegard, "Fatigue Life Assessment of Aluminum Alloys with Casting Defects," *Engineering Fracture Mechanics*, Vol. 44, No. 6, 1993, pp. 875-874.

69. B. Zhang, D.R. Poirier and W. Chen, "Microstructural Effects on High-Cycle Fatigue-Crack Initiation in A356.2 Casting Alloy," *Metallurgical and Materials Transactions A*, Vol. 30A, 1999, pp. 2659-2666.

70. M.E. Seniw, M.E. Fine, E.Y. Chen, M. Meshii and J. Gray, "Relationship of Defect Size and Location to Fatigue Failure in Al Alloy A356 Cast Specimens," *Proc. of the 1997 TMS Fall Symposium, Sep. 14-18,* Indianapolis, IN, U.S.A., ASM International, 1997, pp. 371-379.

71. *Annual Book of ASTM Standards, Section 3: Metal Test Methods and Analytical Procedures*, Vol. 3.1, 1995, E466-82, pp. 470-471.

72. P. Kapranos, D.H. Kirkwood, H.V. Atkinson, J.T. Rheinlander, J.J. Bentzen, P.T. Toft, C.P. Debel, G. Laslaz, L. Maenner, S. Blais, J.M. Rodriguez-Ibabe, L. Lasa, P. Giordano, G. Chiarmetta and A. Giese, "Thixoforming of an Automotive Part in A390 Hypereutectic Al-Si Alloy," *Journal of Materials Science Processing Technology*, Vol. 135, 2003, pp. 271-277.

73. L. Lasa and J.M. Rodriguez-Ibabe, "Toughness and Fatigue Behavior of Eutectic and Hypereutectic Al-Si-Cu-Mg Alloys Produced through Lost Foam and Squeeze Casting," *Materials Science and Technology*, Vol. 20, 2004, pp.1599-1608.

74. Q.G. Wang, D. Apelian and D.A. Lados, "Fatigue Behavior of A356/357 Aluminum Cast Alloys. Part II- Effect of Microstructural Constituents," *Journal of Light Metals*, Vol. 1, 2001, pp. 85-97.

75. C. Meyers and J.S. Chou, "Experimental Investigations of Deformation in HIPped A356 Aluminum Castings," *AFS Transactions*, Vol. 99, 1991, pp. 175-786.

# APPENDIX A

# FATIGUE DATA

**Table A.1** Fatigue data summary of LP PM319-F aluminum alloy, tested at 25°C, stress ratio: R= -1, waveform: sinusoidal, high cycle fatigue (HCF) (# fatigue-tested samples: 23).

| Specimen Code | Test log No. | Specimen ID | Location | Diameter (mm) | ± Load (N) | ± Stress (MPa) | Cycles to Failure |
|---|---|---|---|---|---|---|---|
| L1 | 818541 | 1242 | Bulkhead | 8.91032 | 4986 | 80 | 6339412 |
| L2 | 818549 | 1257 | Bulkhead | 8.88238 | 4711 | 76 | 4971141 |
| L3 | 818484 | 1103 | Bulkhead | 8.93064 | 5200 | 83 | 433195 |
| L4 | 818519 | 1203 | Bulkhead | 8.91032 | 4986 | 80 | 1294079 |
| L5 | 818493 | 1116 | Bulkhead | 8.92302 | 4942 | 79 | 9858710 |
| L6 | 818539 | 1237 | Bulkhead | 8.90778 | 4986 | 80 | 9988892 |
| L8 | 818499 | 1125 | Bulkhead | 8.91540 | 4933 | 79 | 2710537 |
| L9 | 818551 | 1261 | Bulkhead | 8.79840 | 4955 | 80 | 5119092 |
| L10 | 818537 | 1233 | Bulkhead | 8.91032 | 4488 | 72 | 5000739 |
| L12 | 818532 | 1222 | Bulkhead | 8.88492 | 4217 | 68 | 4373482 |
| L13 | 818496 | 1120 | Bulkhead | 8.91540 | 4933 | 79 | 217053 |
| L14 | 818533 | 1224 | Bulkhead | 8.87730 | 4706 | 76 | 1995876 |
| L15 | 818488 | 1109 | Bulkhead | 8.92810 | 4946 | 79 | 379614 |
| L17 | 818508 | 1145 | Bulkhead | 8.91794 | 4933 | 79 | 457637 |
| L18 | 818536 | 1229 | Bulkhead | 8.88238 | 4711 | 76 | 918072 |
| L19 | 818485 | 1104 | Bulkhead | 8.92556 | 4941 | 79 | 324254 |
| L20 | 818526 | 1213 | Bulkhead | 8.91032 | 4488 | 72 | 4547537 |
| L21 | 818486 | 1105 | Bulkhead | 8.91540 | 5182 | 83 | 573352 |
| L22 | 818538 | 1236 | Bulkhead | 8.91540 | 4746 | 76 | 1104851 |
| L23 | 818500 | 1127 | Bulkhead | 8.92302 | 5191 | 83 | 616287 |
| L24 | 818507 | 1143 | Bulkhead | 8.93064 | 5200 | 83 | 167265 |
| L25 | 818475 | 1140 | Bulkhead | 8.90270 | 5169 | 83 | 793754 |
| L26 | 818531 | 1220 | Bulkhead | 8.89000 | 4719 | 76 | 4465850 |

**Table A.2** Fatigue data summary of A356-T6 aluminum alloy, tested at 25°C, stress ratio: R= -1, waveform: sinusoidal, high cycle fatigue (HCF) (# fatigue-tested samples: 26).

| Specimen Code | Test log No. | Specimen ID | Location | Diameter (mm) | ± Load (N) | ± Stress (MPa) | Cycles to Failure |
|---|---|---|---|---|---|---|---|
| HA2 | 809584 | 837 | L5 Bolt Boss | 5.08762 | 1241 | 61 | 410230 |
| HA3 | 809533 | 708 | L5 Bolt Boss | 5.10032 | 1174 | 57 | 6158643 |
| HA4 | 809601 | 672 | L4 Bulkhead | 5.07492 | 1303 | 64 | 969942 |
| HA5 | 809598 | 668 | L4 Bulkhead | 5.09524 | 1246 | 61 | 4037010 |
| HA6 | 809591 | 653 | L4 Bulkhead | 5.09778 | 1317 | 64 | 1918653 |
| HA7 | 809538 | 729 | L5 Bolt Boss | 5.07746 | 1094 | 54 | 1697819 |
| HA8 | 809569 | 634 | L4 Bulkhead | 5.08762 | 1383 | 68 | 1438144 |
| HA9 | 809594 | 658 | L4 Bulkhead | 5.09016 | 1312 | 64 | 1825455 |
| HA10 | 809567 | 628 | L4 Bulkhead | 5.09016 | 1219 | 60 | 5434782 |
| HA11 | 809561 | 616 | L4 Bulkhead | 5.10286 | 1392 | 68 | 1445587 |
| HA13 | 809560 | 615 | L4 Bulkhead | 5.10032 | 1388 | 68 | 2058124 |
| HA14 | 809547 | 766 | L5 Bolt Boss | 5.08508 | 1099 | 54 | 7197321 |
| HA15 | 809553 | 795 | L4 Bolt Boss | 5.08762 | 1383 | 68 | 5587221 |
| HA16 | 809545 | 754 | L5 Bolt Boss | 5.07746 | 1165 | 57 | 4029112 |
| HA18 | 809585 | 838 | L5 Bolt Boss | 5.06984 | 1161 | 57 | 627215 |
| HA19 | 809558 | 611 | L4 Bulkhead | 5.09270 | 1383 | 68 | 4260419 |
| HA21 | 809546 | 761 | L5 Bolt Boss | 5.08508 | 1237 | 61 | 1621077 |
| HA22 | 809592 | 656 | L4 Bulkhead | 5.09524 | 1246 | 61 | 6098732 |
| HA23 | 809543 | 745 | L5 Bolt Boss | 5.09524 | 1103 | 54 | 3251510 |
| HA24 | 809537 | 722 | L5 Bolt Boss | 5.07492 | 1094 | 54 | 2660302 |
| HA25 | 809559 | 614 | L4 Bulkhead | 5.09016 | 1241 | 61 | 2199769 |
| HA27 | 809595 | 662 | L4 Exhaust Rail | 5.08508 | 1308 | 64 | 3001301 |
| HA28 | 809564 | 622 | L4 Bulkhead | 5.09270 | 1312 | 64 | 2527976 |
| HA29 | 809532 | 705 | L5 Bolt Boss | 5.10286 | 1321 | 64 | 813316 |
| HA30 | 809582 | 828 | L4 Bolt Boss | 5.10032 | 1103 | 54 | 2668523 |
| HA31 | 809597 | 666 | L4 Bulkhead | 5.09270 | 1312 | 64 | 4258450 |

**Table A.3** Fatigue data summary of A356-T6 aluminum alloy, tested at 25°C, stress ratio: R= -1, waveform: sinusoidal, low cycle fatigue (LCF) (# fatigue-tested samples: 14).

| Specimen Code | Test log No. | Specimen ID | Location | Diameter (mm) | ± Load (N) | ± Stress (MPa) | Cycles to Failure |
|---|---|---|---|---|---|---|---|
| LA1 | 809611 | 741 | L4 Exhaust Rail | 5.10286 | 3314 | 162 | 4352 |
| LA2 | 809631 | 816 | L4 Exhaust Rail | 5.11048 | 3323 | 162 | 2259 |
| LA3 | 809606 | 719 | L4 Exhaust Rail | 5.08762 | 3292 | 162 | 4887 |
| LA4 | 809624 | 791 | L4 Exhaust Rail | 5.11048 | 3221 | 157 | 7317 |
| LA5 | 809614 | 755 | L4 Exhaust Rail | 5.12572 | 3447 | 167 | 7283 |
| LA6 | 809625 | 792 | L4 Exhaust Rail | 5.11810 | 3229 | 157 | 9653 |
| LA7 | 809610 | 740 | L4 Exhaust Rail | 5.09778 | 3407 | 167 | 1371 |
| LA8 | 809630 | 815 | L4 Exhaust Rail | 5.09270 | 3301 | 162 | 9733 |
| LA9 | 809613 | 751 | L4 Exhaust Rail | 5.10286 | 3314 | 162 | 9830 |
| LA10 | 809618 | 769 | L4 Exhaust Rail | 5.10286 | 3621 | 177 | 6456 |
| LA12 | 809627 | 799 | L4 Exhaust Rail | 5.11048 | 3527 | 172 | 3390 |
| LA13 | 809628 | 800 | L4 Exhaust Rail | 5.08000 | 3686 | 182 | 1581 |
| LA14 | 809605 | 711 | L4 Exhaust Rail | 5.10032 | 3616 | 177 | 97 |
| LA16 | 809632 | 824 | L4 Bulkhead | 5.09524 | 3505 | 172 | 5378 |

**Table A.4** Fatigue data summary of C354-T6 (non-HIPped) aluminum alloy, tested at 25°C, stress ratio: R= -1, waveform: sinusoidal, high cycle fatigue (HCF) (# fatigue-tested samples: 20).

| Specimen Code | Specimen ID | Diameter (mm) | ± Load (N) | ± Stress (MPa) | Cycles to Failure |
|---|---|---|---|---|---|
| NH1 | 354-20-6F | 5.12 | 1750 | 85 | 144365 |
| NH2 | 354-2-6F | 5.12 | 1338 | 65 | 384935 |
| NH4 | 354-13-4F | 5.12 | 1338 | 65 | 1211357 |
| NH5 | 354-16-2A | 5.11 | 1333 | 65 | 1029498 |
| NH6 | 354-18-2A | 5.12 | 1544 | 75 | 1801532 |
| NH7 | 354-19-4F | 5.13 | 1757 | 85 | 432675 |
| NH8 | 354-10-6C | 5.12 | 1750 | 85 | 185776 |
| NH9 | 354-2-6C | 5.11 | 2564 | 125 | 51739 |
| NH10 | 354-7-4C | 5.11 | 1538 | 75 | 419954 |
| NH11 | 354-4-6C | 5.12 | 1544 | 75 | 233754 |
| NH12 | 354-18-4F | 5.13 | 1757 | 85 | 156875 |
| NH13 | 354-16-6C | 5.11 | 3076 | 150 | 8122 |
| NH14 | 354-6-2C | 5.10 | 1532 | 75 | 143604 |
| NH15 | 354-4-2F | 5.11 | 2051 | 100 | 25815 |
| NH18 | 354-10-4C | 5.13 | 2067 | 100 | 281001 |
| NH20 | 354-19-2C | 5.11 | 1333 | 65 | 199337 |
| NH22 | 354-2-2A | 5.13 | 1757 | 85 | 426433 |
| NH23 | 354-19-6C | 5.11 | 1538 | 75 | 601051 |
| NH24 | 354-13-2C | 5.11 | 2051 | 100 | 99861 |
| NH25 | 354-7-6F | 5.12 | 1338 | 65 | 269420 |

**Table A. 5** Fatigue data summary of C354-T6 (HIPped) aluminum alloy, tested at 25°C, stress ratio: R= -1, waveform: sinusoidal, high cycle fatigue (HCF) (# fatigue-tested samples: 11).

| Sample Code | Sample ID | Diameter (mm) | Load (N) | Stress (MPa) | Cycles to Failure |
|---|---|---|---|---|---|
| HP1 | 354-19-1C | 5.13 | 3617 | 175 | 115282 |
| HP2 | 354-4-5C | 5.13 | 3100 | 150 | 1208107 |
| HP3 | 354-16-3A | 5.11 | 3079 | 150 | 1073791 |
| HP4 | 354-6-1C | 5.11 | 2051 | 100 | 8870295 |
| HP5 | 354-2-3F | 5.12 | 2574 | 125 | 2827385 |
| HP6 | 354-20-3A | 5.11 | 2564 | 125 | 4748988 |
| HP7 | 354-6-5A | 5.13 | 3100 | 150 | 1294594 |
| HP8 | 354-13-3C | 5.11 | 2564 | 125 | 9021791 |
| HP9 | 354-16-3F | 5.13 | 3617 | 175 | 328071 |
| HP11 | 354-2-3A | 5.13 | 3617 | 175 | 371325 |
| HP12 | 354-19-3C | 5.12 | 2059 | 100 | 5231141 |

**Table A.6** Fatigue data summary of AE425 aluminum alloy, tested at 150°C (302°F), stress ratio: R= -1, waveform: sinusoidal, high cycle fatigue (HCF) (# fatigue-tested samples: 18).

| Specimen Code | Test log No. | Specimen ID | Location | Diameter (mm) | ± Load (N) | ± Stress (MPa) | Cycles to Failure |
|---|---|---|---|---|---|---|---|
| ae1 | 795014 | 111 | Dome | 6.35762 | 2335 | 74 | 5236892 |
| ae2 | 795012 | 105 | Dome | 6.35508 | 2331 | 74 | 993563 |
| ae3 | 795017 | 119 | Dome | 6.35508 | 2602 | 82 | 1616578 |
| ae4 | 794994 | 27 | Dome | 6.37286 | 2567 | 81 | 442006 |
| ae5 | 795013 | 108 | Dome | 6.35254 | 2331 | 74 | 619245 |
| ae6 | 795003 | 56 | Dome | 6.36778 | 2340 | 74 | 1594362 |
| ae7 | 795004 | 57 | Dome | 6.36016 | 2447 | 77 | 527696 |
| ae8 | 795006 | 60 | Dome | 6.35000 | 2406 | 76 | 1919035 |
| ae9 | 837277 | 39 | Dome | 6.35508 | 2331 | 74 | 2394630 |
| ae10 | 795015 | 114 | Dome | 6.35762 | 2335 | 74 | 7966125 |
| ae11 | 795002 | 55 | Dome | 6.35000 | 2215 | 70 | 1540921 |
| ae12 | 795016 | 117 | Dome | 6.35508 | 2331 | 74 | 1098768 |
| ae13 | 837278 | 71 | Dome | 6.35254 | 2220 | 70 | 1558724 |
| ae14 | 794995 | 30 | Dome | 6.35762 | 3176 | 100 | 243068 |
| ae15 | 794996 | 32 | Dome | 6.36016 | 2669 | 84 | 908713 |
| ae16 | 794988 | 10 | Dome | 6.34492 | 2433 | 77 | 1560476 |
| ae17 | 794998 | 41 | Dome | 6.34746 | 2438 | 77 | 930086 |
| ae18 | 794987 | 7 | Dome | 6.36016 | 2224 | 70 | 8576256 |

**Table A.7** Fatigue data summary of AE425 aluminum alloy, tested at 300°C (572°F), stress ratio: R= -1, waveform: sinusoidal, high cycle fatigue (HCF) (# fatigue-tested samples: 16).

| Specimen Code | Test log No. | Specimen ID | Location | Diameter (mm) | ± Load (N) | ± Stress (MPa) | Cycles to Failure |
|---|---|---|---|---|---|---|---|
| AE1 | 795084 | 107 | Dome | 6.32714 | 1259 | 40 | 754881 |
| AE3 | 795073 | 72 | Dome | 6.36524 | 1432 | 45 | 622889 |
| AE4 | 795082 | 99 | Dome | 6.36524 | 1241 | 39 | 3470703 |
| AE5 | 795060 | 25 | Dome | 6.33730 | 1134 | 36 | 1956935 |
| AE6 | 795065 | 42 | Dome | 6.35508 | 1143 | 36 | 1542358 |
| AE7 | 795069 | 53 | Dome | 6.37286 | 1148 | 36 | 5856554 |
| AE8 | 795063 | 35 | Dome | 6.35000 | 1139 | 36 | 2086139 |
| AE9 | 795083 | 106 | Dome | 6.35000 | 1330 | 42 | 969637 |
| AE10 | 795055 | 3 | Dome | 6.36016 | 1143 | 36 | 9784305 |
| EA11 | 795075 | 77 | Dome | 6.37540 | 1148 | 36 | 7821612 |
| AE12 | 795088 | 118 | Dome | 6.37032 | 1241 | 39 | 3746476 |
| AE13 | 795070 | 54 | Dome | 6.33476 | 1228 | 39 | 4303409 |
| AE14 | 795064 | 37 | Dome | 6.34746 | 1139 | 36 | 1628781 |
| AE15 | 795086 | 112 | Dome | 6.34492 | 1139 | 36 | 3197862 |
| AE16 | 795089 | 123 | Dome | 6.32206 | 1223 | 39 | 3135978 |
| AE17 | 795087 | 113 | Dome | 6.34238 | 1228 | 39 | 7882044 |

**Table A.8** Fatigue data summary of PM390 aluminum alloy, tested at 150°C (302°F), stress ratio: R= -1, waveform: sinusoidal, high cycle fatigue (HCF) (# fatigue-tested samples: 14).

| Specimen Code | Test log No. | Specimen ID | Location | Diameter (mm) | ± Load (N) | ± Stress (MPa) | Cycles to Failure |
|---|---|---|---|---|---|---|---|
| pm2 | 795032 | 235 | Dome | 5.13080 | 1695 | 82 | 945261 |
| pm3 | 795022 | 206 | Dome | 5.12572 | 1641 | 80 | 1878157 |
| pm4 | 795023 | 208 | Dome | 5.12318 | 1548 | 80 | 784870 |
| pm5 | 795021 | 205 | Dome | 5.13080 | 1819 | 88 | 352663 |
| pm6 | 795050 | 314 | Dome | 5.12826 | 1499 | 73 | 1604666 |
| pm7 | 795054 | 323 | Dome | 5.12318 | 1939 | 94 | 298687 |
| pm8 | 735039 | 265 | Dome | 5.13080 | 1570 | 76 | 1253872 |
| pm9 | 795026 | 217 | Dome | 5.11556 | 1566 | 76 | 2238223 |
| pm11 | 795049 | 310 | Dome | 5.12572 | 1570 | 76 | 650423 |
| pm12 | 795020 | 201 | Dome | 5.12826 | 1641 | 80 | 2261543 |
| pm13 | 795044 | 290 | Dome | 5.12064 | 1495 | 73 | 674769 |
| pm14 | 795025 | 211 | Dome | 5.12318 | 1423 | 69 | 1955648 |
| pm15 | 795035 | 242 | Dome | 5.11556 | 1561 | 76 | 8855065 |
| pm20 | 795043 | 289 | Dome | 5.13080 | 1499 | 73 | 9976007 |

**Table A.9** Fatigue data summary of PM390 aluminum alloy, tested at 300°C (572°F), stress ratio: R= -1, waveform: sinusoidal, high cycle fatigue (HCF) (# fatigue-tested samples: 15).

| Specimen Code | Test log No | Specimen ID | Location | Diameter (mm) | ± Load (N) | ± Stress (MPa) | Cycles to Failure |
|---|---|---|---|---|---|---|---|
| PM1 | 795112 | 284 | Dome | 5.10540 | 778 | 38 | 9569129 |
| PM2 | 795097 | 230 | Dome | 5.12064 | 783 | 38 | 5048161 |
| PM3 | 795105 | 257 | Dome | 5.12318 | 720 | 35 | 9725712 |
| PM4 | 795120 | 308 | Dome | 5.09016 | 774 | 38 | 3957913 |
| PM5 | 795113 | 285 | Dome | 5.12064 | 783 | 38 | 9892293 |
| PM6 | 795099 | 241 | Dome | 5.09778 | 778 | 38 | 4514636 |
| PM7 | 795117 | 294 | Dome | 5.11302 | 840 | 41 | 2451621 |
| PM8 | 795090 | 203 | Dome | 5.11556 | 720 | 35 | 8229600 |
| PM9 | 795096 | 229 | Dome | 5.12318 | 783 | 38 | 1841109 |
| PM11 | 795104 | 253 | Dome | 5.10286 | 778 | 38 | 1674078 |
| PM12 | 795108 | 273 | Dome | 5.09778 | 716 | 35 | 9331552 |
| PM13 | 795094 | 222 | Dome | 5.10794 | 778 | 38 | 4380928 |
| PM14 | 795119 | 300 | Dome | 5.10286 | 818 | 40 | 1396396 |
| PM15 | 795091 | 213 | Dome | 5.11556 | 783 | 38 | 2647294 |
| PM16 | 795102 | 251 | Dome | 5.11810 | 783 | 38 | 9519347 |